Stony Brook University

Changes in Atmospheric Circulation between Solar Maximum and Minimum Conditions in Winter and Summer

A Dissertation Presented

by

Jae Nyung Lee

to

The Graduate School

in Partial Fulfillment of the

Requirements

for the Degree of

Doctor of Philosophy

in

Marine and Atmospheric Science

Stony Brook University

May 2008

Stony Brook University

The Graduate School

Jae Nyung Lee

We, the dissertation committee for the above candidate for the Degree of Doctor of Philosophy, hereby recommend acceptance of this dissertation

Sultan Hameed – Dissertation Advisor

Professor, School of Marine and Atmospheric Science

Minghua Zhang - Chairperson of Defense

Professor, ITPA director, School of Marine and Atmospheric Science

Marvin Geller

Professor, School of Marine and Atmospheric Science

Robert Wilson

Professor, School of Marine and Atmospheric Science

Drew T. Shindell

Researcher, NASA Goddard Institute for Space Studies

This dissertation is accepted by the Graduate School

Lawrence Martin

Dean of the Graduate School

Abstract of the Dissertation

Changes in Atmospheric Circulation between

Solar Maximum and Minimum Conditions in Winter and Summer

by

Jae Nyung Lee

Doctor of Philosophy

in

Marine and Atmospheric Science

Stony Brook University

2008

Statistically significant climate responses to the solar variability are found in Northern Annular Mode (NAM) and in the tropical circulation. This study is based on the statistical analysis of numerical simulations with ModelE version of the chemistry coupled Goddard Institute for Space Studies (GISS) general circulation model (GCM) and National Centers for Environmental Prediction/National Center for Atmospheric Research (NCEP/NCAR) reanalysis.

The low frequency large scale variability of the winter and summer circulation is described by the NAM, the leading Empirical Orthogonal Function (EOF) of geopotential heights. The newly defined seasonal annular modes and its dynamical significance in the stratosphere and troposphere in the GISS ModelE is shown and

compared with those in the NCEP/NCAR reanalysis. In the stratosphere, the summer NAM obtained from NCEP/NCAR reanalysis as well as from the ModelE simulations has the same sign throughout the northern hemisphere, but shows greater variability at low latitudes. The patterns in both analyses are consistent with the interpretation that low NAM conditions represent an enhancement of the seasonal difference between the summer and the annual averages of geopotential height, temperature and velocity distributions, while the reverse holds for high NAM conditions. Composite analysis of high and low NAM cases in both the model and observation suggests that the summer stratosphere is more "summer-like" when the solar activity is near a maximum. This means that the zonal easterly wind flow is stronger and the temperature is higher than normal. Thus increased irradiance favors a low summer NAM. A quantitative comparison of the anti-correlation between the NAM and the solar forcing is presented in the model and in the observation, both of which show lower/higher NAM index in solar maximum/minimum conditions.

The summer NAM in the troposphere obtained from NCEP/NCAR reanalysis has a dipolar zonal structure with maximum variability over the Asian monsoon region. The corresponding EOF in ModelE has a qualitatively similar structure but with less variability in the Asian monsoon region which is displaced eastward of its observed position. In both the NCEP/NCAR reanalysis and the GISS GCM, the negative anomalies associated with the NAM in the Euro-Atlantic and Aleutian island regions are enhanced in the solar minimum conditions, though the results are not statistically significant.

The difference of the downward propagation of NAM between solar maximum and solar minimum is shown with the NCEP/NCAR reanalysis. For the winter NAM, a much greater fraction of stratospheric circulation perturbations penetrate to the surface in solar maximum conditions than in minimum conditions. This difference is more striking when the zonal wind direction in the tropics is from the west: when equatorial 50 hPa winds are from the west, no stratospheric signals reach the surface under solar minimum conditions, while over 50 percent reach the surface under solar maximum conditions.

This work also studies the response of the tropical circulation to the solar forcing in combination with different atmospheric compositions and with different ocean modules. Four model experiments have been designed to investigate the role of solar forcing in the tropical circulation: one with the present day (PD) greenhouse gases and aerosol conditions, one with the preindustrial (PI) conditions, one with the doubled minimum solar forcing, and finally one with the hybrid-isopycnic ocean model (HYCOM). The response patterns in the tropical humidity and in the vertical motion due to solar forcing are season dependent and spatially heterogeneous. The tropical humidity response from the model experiments are compared with the corresponding differences obtained from the NCEP/NCAR reanalysis with all years and with non-ENSO years. Both the model and the reanalysis consistently show that the specific humidity is significantly greater in the convective region in solar maximum compared to solar minimum for January and July. The column integrated humidity in all the model experiments with different composition, different solar forcing, and different ocean module, increased with solar forcing in the tropical band over the Atlantic sector

in both seasons. The model's humidity response pattern is generally consistent with the paleoclimate records indicating increased precipitation near the equator that decreases at subtropical to middle latitudes with increased solar output.

The differences in the zonally averaged vertical velocities indicate that the ascending branch of the Hadley cell is enhanced and shifted northward, and that the descending branch is weakened and shifted northward in the solar MAX simulation in January. The downward branch of the Hadley cell is strengthened in MAX in July.

A possible link of climate response in midlatitudes to solar forcing is also presented by showing changes in zonal mean wind, changes in temperature gradient, and changes in E-P flux.

Table of Contents

List of Figures

List of Tables

Acknowledgement

It is difficult to overstate my gratitude to my Ph.D. supervisor, Dr. Sultan Hameed. With his enthusiasm, his patience, and his great efforts to explain things clearly and simply, he helped to make sun-climate research fun for me. Throughout my Ph.D years, he provided encouragement, sound advice, good teaching, and lots of good ideas.

I would like to thank to my dissertation committee members. Meeting with Dr. Drew T. Shindell provided me a new horizon of modeling and a great opportunity to work with the GISS GCM. He provided clear suggestions, writings, and huge amount of model outputs and codes as well. I would like to express my sincere thanks to Dr. Minghua Zhang. His clear knowledge made many topics of atmospheric science exciting for me throughout years. He provided many discussions and radiation codes. I would like to express my warm thanks to Dr. Robert Wilson. He taught me how to apply statistics to atmospheric science in a practical manner. He provided good teaching and a series of matlab codes. I wish to thank Dr. Marvin Geller. He provided me motivations and deep understanding of solar research. I am truly grateful for his invitation to the CAWSES meeting and for introducing me to many of his colleagues.

I would like to thank the many people who have taught me atmospheric science: Dr. Robert Cess, who showed me the vision of atmospheric science for the first time, Dr. Brian Colle, and Dr. Edmund Chang.

I also greatly appreciate the professors at Yonsei University who laid the foundation for my scientific way of thinking through solid education in physics.

I am indebted to my many student colleagues for providing a stimulating and fun environment in which to learn and grow. I am especially grateful to my office mates; Jie Gong and Matt Jones, and friends; Yanluan Lin, Joe Olson, Hua Song, Howard Teich Keyi Chen, Wuyin Lin, Moguo Sun, and Yanjuan Guo at SoMAS.

I would like to thank Greg Faluvegi at GISS for organizing the model outputs and Kristy Field at Columbia University for running the model.

I am grateful to the secretaries and librarians in the MoMAS for assisting me in many different ways. Carol Dovi, Nancy Glover, and Gina Gartin deserve special mention.

Most importantly, I wish to thank my beloved parents, Beyonjun Kim and Sunny Chung. They bore me, taught me, and loved me.

Last, I would like to thank my wonderful family, Shinae Lee, Sungsu Lee, and Suhoung Lee, who inspire me all the time. I dedicate my thesis to them.

1. Introduction

1.1 general introduction

Identifying the natural variability of solar irradiance and estimating its impacts on climate is an essential issue in discussions of climate change because any variability in the Sun-Climate system may ultimately cause the climate to change. Despite the important theoretical and observational evidence on the Sun-climate mechanism, many aspects of this link still remain uncertain. The IPCC report [2007] repeatedly states that the level of scientific understanding of the solar radiative forcing is very low. The projection of the future climate change due to greenhouse gases will become more reliable if the influences of the solar forcing are explicitly accounted for.

Since 1978, as analyses of satellite observation of solar activity provided measurements of solar variability in addition to the total solar irradiance (TSI), solar variability has been the focus of more serious investigations as a potential forcing factor of climate change. The variations of solar irradiance are not uniformly distributed through the solar spectrum, but are concentrated in the ultra violet (UV) spectral region. The variations in the UV radiation over the 11-year solar cycle are up to a few percent while the TSI varies by only less than 0.1%, which corresponds to a global solar irradiance change of 1.1W/m² at the top of the atmosphere [*Lean*, 2000]. This suggests that the effect of UV radiation on stratospheric chemistry and dynamics provides a possible link between the solar variability and Earth's climate. From numerous early observational and theoretical works,, the in-phase relationship between solar activity

and ozone was already known for the past two decades [*Zerefos and Crutzen*, 1975; *Crutzen et al*., 1975; *Callis and Neally*, 1978; *Penner and Chang* 1978; *Brasseur and Simon*, 1981; *Brasseur et al*., 1987; *Angell*, 1988, 1989, 1991; *Haigh*, 1994]. *Geller* [1980; 1988] suggested that a radiative-dynamic feedback might give a larger response to solar UV variations than expected because radiative changes can be amplified by altering planetary-wave propagation, which further changes the polar vortex and the meridional temperature gradient. The GCM modeling work of *Haigh* [1999] and *Shindell et al.* [1999a] introduced the role of ozone in amplifying the direct solar UV influences on the zonal mean state of the middle atmosphere.

Christoforou and Hameed [1997] documented that the intensity and position of the centers of action (COA) in the North Pacific Ocean, the Aleutian Low and Hawaiian High, depends on the phase of solar activity. The presence of 11-year solar cycle was also identified in tropospheric and stratospheric temperatures and geopotential heights [*Labitzke*, 1982; *Labitzke*, 2001], stratosphere/troposphere coupling via Northern Annular Mode (NAM) [*Shindell et al*., 2001; *Baldwin and Dunkerton*, 2005], and stratospheric circulation [*Kodera and Kuroda*, 2002]. There are recent successful modeling works, where the chemical, thermal, and dynamic structure changes were observed in the stratosphere when the solar UV is varied [*Matthes et al.,* 2003; 2006; *Shindell et al*., 2006a; 2006b; *Haigh*, 2006]. Variations in solar irradiance are particularly large in the UV, and these wavelengths are absorbed in the stratosphere, where they also increase the ozone concentration via oxygen photolysis, amplifying stratospheric heating [*Haigh*, 1994; 1999; *Shindell et al*., 1999a]. Those changes in the stratosphere are found to influence the troposphere [*Meehl et al*., 2003; *Meehl and Hu*, 2006; *Matthes,* 2003].

Compared to the past, the present research environment can provide more observational and numerical evidences to identify the sun-climate connections. NCEP/NCAR reanalysis provides 60 years of complete atmospheric data based on in situ and satellite measurement up to 10 hPa. The European Center for Medium-Range Weather Forecasts (ECMWF) Re-Analysis (ERA-40) data also covers 45 years since mid-1957 to mid-2002 and extends further to 0.1 hPa level. These data can be used to examine the vertical structure of a solar signal over more than five 11-year solar cycles.

The present work has used both the reanalysis and the Goddard Institute for the Space Science (GISS) ModelE to study the impact of 11-year solar variability on the large scale and tropical circulation, and found that the characteristic features of the Northern Annular Mode are sensitive indicators of solar forcing, and that the tropical circulation plays an important mechanical role. While the correlation between solar forcing and NAM in the winter seasons have been previously investigated by many studies [*Shindell et al.,* 1999b; 2001, *Baldwin and Dunkerton*, 2005], the mechanism for sun-climate connection is not fully understood, and the amplitude and origin of the stratospheric ozone response is still controversial.

Most of the studies in wave features and NAM phenomena are limited to winter seasons. The present work has extended the study of NAM to summer seasons, and found significant solar signals by newly defining the NAM in the summer stratosphere. To better understand the role of solar activity variations in the modulation of NAM, the recent GISS ModelE simulation experiments which impose spectrally varying irradiance changes are compared with the observational solar signals obtained from NCEP/NCAR reanalysis [*Lee and Hameed*, 2007; *Lee et al.,* 2007]. The stratospheric NAM is

significantly correlated with the solar activity during summer. The analysis of NAM in both the model and observations suggests that the summer stratosphere is more "summer-like" when the solar activity is near a maximum. This means that the zonal easterly wind flow is stronger and the temperature higher than normal. Thus increased irradiance favors a low summer NAM. A quantitative comparison of the anti-correlation between the NAM and the solar forcing is presented in the model and in observations, both of which show lower/higher NAM index in solar maximum/minimum conditions. The temperature fluctuations in simulated solar minimum conditions are greater than in solar maximum throughout the summer stratosphere.

Thompson and Wallace [1998; 2000] argued the dynamical coupling between the stratosphere and troposphere as vertically coherent variations in the annular modes of extratropical variability, which are characterized by zonally symmetric fluctuations in atmospheric pressure between the polar regions and the middle latitudes. *Baldwin and Dunkerton* [2001] demonstrated the vertical coupling of the tropospheric NAM with the stratospheric NAM. They showed that the associated changes in tropospheric circulation persist as long as the corresponding changes in stratosphere, up to ~60days. Therefore, changes in NAM at tropospheric levels tend to persist as long as the corresponding same-sign changes exist in NAM at stratospheric levels. The downward propagation rate of the winter NAM is investigated in different solar and QBO conditions and the propagation rate was found to be higher when the solar UV is stronger [*Hameed and Lee*, 2005].

Many works have proposed tropical climate changes associated with the solar cycle, with warmer and moister troposphere during the solar maximum which is similar to that expected when greenhouse gases increase. *Meehl et al*. [2003] suggested a

feedback mechanism for solar forcing: enhanced irradiance produces greater evaporation intensifying the regional monsoon, the Hadley and the Walker circulations in the tropics, leading to cloud reductions and hence more solar input over the subtropical ocean regions. *van Loon et al*. [2004], *Kodera* [2005], *van Loon et al*. [2007] showed significant differences in the seasonal vertical velocity (ω) over the tropics between solar maximum and minimum. Some of the observational studies suggest that the thermal solar signal is preferentially strong in subtropical Pacific areas and affects the moisture transport and precipitation in these regions [*van Loon et al*., 2004, *van Loon et al*., 2007].

However, there is substantial uncertainty in the identification of climate response to solar cycle variations because the response is difficult to separate from internal climate variations and the response to anthropogenic forcing. Therefore, to investigate the role of solar forcing on the variability of humidity and the intensity of tropical circulation, a GCM experiment with double minimum solar forcing is carried out. Changes in Hadley circulation and in humidity induced by solar forcing are found to be statistically significant. The specific humidity is greater in the convective region in solar maximum compared to minimum for both winter and summer seasons. The responses of zonally averaged vertical velocities with present day greenhouse gas and aerosol conditions indicate that the ascending branch of the Hadley cell is enhanced near the equator and the ITCZ is shifted northward in response to solar forcing during winter. The changes in the vertical motion are not significantly increased by doubling the solar forcing.

The thesis is divided into seven chapters. The second chapter presents the general characteristics and downward propagation of NAM. The third chapter discusses analysis

of NAM to determine the effect of solar variability on its downward propagation rate , which was published in the *Geophysical Research Letters* in 2005. The fourth chapter discusses the physical significance of the summer NAM and its relation to solar cycle published in the *J. of Geophysical Research* in 2007. The fifth chapter then describes the statistically significant solar signal in the summer NAM from the GCM experiments published in the *Journal of Atmospheric and Solar-Terrestrial Physics* in 2008. The sixth chapter then goes on to explain how new model experiments were set up with the GCM to better understand solar signals in tropical circulation. Solar signals in the tropical circulation are described in terms of the specific humidity and the vertical velocities. Finally, chapter seven provides more evidences of solar signal in mid-latitudes in terms of temperature gradient, Eliassen-Palm flux, and zonal mean wind.

1.2 Solar variability

1.2.1 Sun

The sun is mostly made up of hydrogen (75% of the mass) and helium (25% of the mass). But, it is neither a solid nor a gas but plasma made up of electrons, protons, and atomic nuclei which is gaseous near the solar surface but gets denser towards the core. The sun can be decomposed into three layers (http://sohowww.nascom.nasa.gov/, here after). The solar interior composed of the core which prevails to temperature between 13.5 and 15.6 million K. Above this core, energy is carried outwards by radiation through the radiative zone (the intermediate zone). However, the radiation does not reach directly outwards from this layer, because the plasma density is very high and

the radiation gets bounced around countless numbers of times. It takes about 170 thousand years for radiation to escape from the core to the top of the radiative zone. Outer layer of these two spherical shells, where the temperature drops below 0.2 million K, is the convective zone. The plasma in this layer is too cool and opaque to allow radiation to pass. Instead, huge convection form and large bubbles of hot plasma move up towards the surface. The convective zone can be divided into the photosphere and the thin outer layer, chromosphere. The temperature of the photosphere is only about 5,800K. The strong characteristic of solar atmosphere over photosphere is the granular cells. Granule is irregular, bright, polygonal structures with diameter of approximately 1000Km and one life span of 10 minutes. Sometimes, super-granulation happens with huge granule cells with diameter of 30,000 Km and one life span of one day, which are common over the solar surface. The cause of the granulation is the instabilities of deeper layers against thermal convection.

The energy transfer by the radiation is not large enough to maintain the thermal equilibrium due to the huge temperature difference between the layers. In some regions where the temperature in the inside rises very strongly, the column expands, and the parcel ascends adiabatically (by assuming the plasma as an ideal gas). The ascending plasma parcel (~1 km/s) recover a part of their work done on expansion from the recombination energy, which develops during the combination from proton and electron to an H-atom. The ascent movements in the granules are stopped by the stable layering in the upper photosphere. The mechanical energy from compression of the ascending parcel is transported in the form of acoustic wave into the outer layers.

About 1,500 km higher over photosphere, there are many narrow, bright flame tongues, faculae, which are characterized by 5,000Km of height and 500 Km of width. Faculae are bright areas that are usually most easily seen near the limb, or edge, of the solar disk. The Sunspots result when solar magnetic field lines erupt at the solar surface due to the interaction of electromagnetic forces in the solar plasma with solar turbulence. While the sunspots tend to make the Sun look darker, the faculae make it look brighter. Both faculae and sunspots are magnetic phenomena that appear more frequently during time of high solar activity. The changes of the solar faculae are mainly responsible for solar ultraviolet (UV) flux output variation. At the visible wavelengths which dominate total solar irradiance (TSI), faculae emission near solar maximum exceeds the dimming effect caused by sunspots, resulting in a net TSI increase [*Solanki and Fligge*, 2000].

1.2.2. Records of solar variability

Since late 1978, the different Satellite-based radiometers in space, HF on NIMBUS 7, ACRIM (Active Cavity Radiometer Irradiance Monitor) I on SMM, ACRIM II on UARS, VIRGO on SOHO, ACRIM III on ACRIMSat have been monitoring the TSI [*Fröhlich,* 2006]. The various data sets are offset, but they are in basic agreement with long term variations of TSI with amplitudes on the order of 0.1%.

Solar Radiation and Climate Experiment (SORCE) is a small free-flying satellite carrying TIM (Total Irradiance Monitor), SIM (Spectral Irradiance Monitor), SOLSTICE (Solar Stellar Irradiance Comparison Experiments) A&B, and XPS (XUV Photometer System) to measure the solar radiation at the top of the atmosphere. The SIM and TIM mission have been measuring the SSI and TSI since August 2003 up to the present solar minimum time frame. The SIM measures the spectral irradiance in the 200-2400 nm

region covering more than 97% of the total solar irradiance (TSI) with a resolving power ranging from 280 in the near UV to a minimum of 37 at 1260 nm [*Harder et al.*, 2008]. With this full spectral coverage, the spectral irradiance time series can be integrated into sub-ranges; extreme ultraviolet (XUV), ultraviolet (UV), visible, infrared (IR), and near infrared. The record of SSI measured from space with the required precision to detect the distribution of the solar energy input to the earth. The dominant temporal solar variances are due to flares (minutes-hours), active region evolution and solar rotation (days to weeks), and solar cycle magnetic evolution (months to years). The SSI variations are dependent on the solar atmosphere where the emissions are originated [*Woods et al.*, 2008]. The photospheric emissions, which dominate in the near infrared, visible, and near ultraviolet ranges, vary by about 0.1% over the 11-year solar cycle and are characterized by dark sunspots and bright faculae. The emissions from the solar chromosphere and transition region are easily identified in the extreme ultraviolet and far ultraviolet ranges, and their solar cycle variations of 20% to 300% are associated with the evolution of bright plages. Coronal emissions, which dominate in the X-ray and the lower part of the extreme ultraviolet range, vary by factors of 5 to 1000 over the solar cycle.

Besides TSI, other records of solar variability go back further than the measurement of TSI using electrical substitution radiometer (ESRs) from the space. Three different indexes are used in this study to determine the solar maximum and minimum conditions.

a. sunspot numbers

b. 10.7cm radio flux

c. 290-295nm UV flux

a. Sunspot numbers

Since first observed by using the telescope from the time of *Galileo* in 1610 (http://solar-center.stanford.edu/sunspots/galileo.html), small blemishes or spots on the surface of the Sun are observed. Many independent observers have compiled the records of the number and character of these sunspots. In 1843, S. *Heinrich Schwabe* recognized a distinctive 11-year sunspot cycle. The sunspot numbers are counted day-by day by adding 10 times the number of sunspot groups to the total number of individual spots after *J. Wolf* (1816-1893). The measurement of sunspots depends not only on observer but observation site because spots are not symmetrically distributed across solar longitude. The daily international number is computed as a weighted average of measurements from a network of observatories (http://www.ngdc.noaa.gov/stp/SOLAR/SSN/ssn.html). In the 17th century, almost no sunspots were observed for a period of almost 50 years. During this period, referred to as the *Maunder Minimum*, winters in Europe were much longer and colder than normal [*Eddy*, 1976]. Since then, the trend suggests a gradual increase in solar output (*Modern Maximum*).

b. 10.7 cm radio flux

The 10.7 cm (2800 MHz in frequency) solar flux is a measurement of the integrated emission at 10.7cm wavelength. It is almost completely thermal in origin, and directly related to the total amount of plasma trapped in the magnetic fields overlying active

regions. This index is highly and positively correlated with the sunspot numbers. (http://www.drao-ofr.hia-iha.nrc-cnrc.gc.ca/icarus/www/sol_home.shtml).

c. 290-295 nm UV flux

The reconstruction of UV flux has been performed by combining historical estimates of solar spectral irradiance variability and contemporary measurements and models [*Lean*, 2000]. Models of spectral irradiance changes, which rely on information about the wavelength dependence of the sunspot and facular contrasts, have been developed, motivated by the need for simulations of climate and atmospheric responses to properly account for a multitude of wavelength-dependent processes. Current spectral irradiance variability models rely on information about the wavelength dependence of sunspot contrasts made by ground-based or SORCE TIM/SIM observations and facular contrasts estimated by solar atmosphere models.

The facular brightening is constructed based on ratios of core-to-wing emissions in the Mg II and Ca II Fraunhofer absorption lines after 1976. The advantage of a core-to-wing ratio, which defines the Mg II index, rather than the absolute solar irradiance of the line center is that the former is less sensitive to spectral resolution of the instrument (http://www.iup.uni-bremen.de/gome/gomemgii.html). The UV variations from 1950 to 1976 are estimated from linear combinations of daily Ca plage indices and 100-day mean 10.7 cm radio fluxes from 1950 to 1976. The spectral irradiance at wavelength λ is determined from multiple regressions of changes in faculae brightening and sunspot darkening.

2. The Northern Annular Mode (NAM)

2.1 Definition

Thompson and Wallace [1998] defined the northern annular mode (NAM) as the leading empirical orthogonal function (EOF) of the northern hemisphere (NH) wintertime monthly mean sea level pressure and showed that the surface signature of the NAM is dominated by a zonally symmetric, meridional seesaw in atmospheric mass between the polar region and mid latitudes. To distinguish the leading EOF of the NH SLP field from the North Atlantic Oscillation (NAO), they referred to it as the NAM or the Arctic Oscillation (AO). *Thompson and Wallace* [2000] showed that the NAM has a barotropic structure in geopotential height fields marked by a zonally symmetric pattern that amplifies by a factor of ~5 from the surface to the lower stratosphere for the NH winter season (October – April). The NAM exhibits its largest variance in the North Atlantic sector. Baldwin and Dunkerton [1999, 2001] demonstrated the vertical coupling of the tropospheric NAM with the stratospheric NAM. The changes in NAM at tropospheric levels tend to persist as long as the corresponding same-sign changes exist in NAM at stratospheric levels.

2.2 Seasonality of geopotential height

Fig. 2.1 shows monthly averages of the mean Northern Hemisphere geopotential height fields at 1000-hPa, 500-hPa, and 10-hPa from January to December. There is an

annual march in the geopotential height at all levels, with higher values near the surface during the cold-season (October – April). Figure 2.2 shows the annual march of the standard deviation in the Northern Hemisphere geopotential heights. We can see that the variance is large in the cold season and it is low during the warm season (May – September).

The variance of $\langle Z_{10} \rangle$ is largest in winter when the westerly polar vortex is strongest. If fluctuations in $\langle Z_{10} \rangle$ are a manifestation of planetary wave-mean flow interaction, its observed seasonality is consistent with the predictions of *Charney and Drazin* [1961]. For this reason, the winter in the NH is called the active season [*Thompson and Wallace*, 2000]. It is only during the active season that the leading mode in the 10-hPa fields has the characteristic zonally symmetric pattern which is similar to the pattern in the lower-troposphere. *Baldwin and Dunkerton* [2001] showed the usefulness of the NAM formalism in detecting propagation of signals from the stratosphere to the troposphere but the mechanisms by which stratospheric variability influences the tropospheric circulation remain unclear. *Thompson et al*. [2005] suggested that processes by which variations in the amplitude and location of stratospheric wave drag are communicated to tropospheric levels can be divided into the "direct" and "indirect" effects. They defined the "direct effect" as the balanced response of the zonal-mean tropospheric circulation to anomalous mechanical and thermal forcing at stratospheric levels, and the "indirect" effects as those where changes in the stratospheric zonal flow impact the propagation of wave activity. Indirect effects include amplification due to internal tropospheric dynamics [*Song and Robinson*, 2004], the impact of anomalous shear at the tropopause level on vertically propagating planetary waves

[*Shindell et al*., 1999b; *Hu and Tung*, 2001], and feedbacks between the shear at the tropopause level and the momentum flux by baroclinic eddies [*Kushner and Polvani*, 2004]. However, the questions remain as to why does not downward propagation always happen and why the time scale for downward propagation varies.

2.3 Structure of the annular modes during the active season and inactive Season

The active season is defined as time of year when troposphere/stratosphere coupling is vigorous, and corresponds to the winter when the zonal flow in the lower stratosphere is disturbed by waves dispersing upwards from the troposphere. The *Charney -Drazin* theory predicts that these interactions should occur when the zonal flow in the lower stratosphere is westerly, but less than a threshold value. Therefore, the structure of the NAM is different with the season. During the active seasons, the NAM is characterized by equivalent barotropic, meridional dipoles in the extratropical circulation. During inactive seasons, the stratospheric NAM has a different pattern and it is different from the pattern of the tropospheric NAM. In the stratosphere, the summer pattern is characterized by variability of the same sign throughout the northern hemisphere, with the highest amplitudes in the tropics and gradually decreasing towards the pole. The tropospheric NAM has a dipole structure in summer like the winter mode but its greatest variability is over the Asian monsoon region. The details on the structure of summer NAM and its physical significance are described in the chapter 4.

2.4 Downward propagation of NAM

To understand the physical significance of the downward propagation of Northern Annular Mode during the active season, it is useful to examine characteristics of the interannual and month-to-month variability of the Northern Hemisphere winter circulation by examining anomalous wind patterns and comparing them with NAM indexes for the corresponding winters.

In figure 2.3, the anomalous zonal-mean winds are shown for two negative NAM winters (1977 and 1985) and two positive NAM winters (1989 and 1990). Each winter is presented from top to bottom, as December, January and February. It was noted by *Kodera* [1995] that the evolution of zonal wind anomalies has similar patterns even though month-to-month variation of stratospheric and tropospheric circulation is quite different for each winter. The first and second columns, for the 1977 winter and 1985 winter show that negative wind anomalies (weak westerlies) first appear in December in the midlatitudes of the low stratosphere and they shift poleward and intrude into the troposphere by January.

A similar but opposite polarity of the evolution of anomalies is observed during 1989 and 1990 winters as shown in third and forth columns where downward propagation of positive wind anomalies (stronger westerlies) is seen. The NAM index, defined as the time coefficients of the first EOF of geopotential height field explains about 20% of variability throughout the troposphere and up to 45% at 10 hPa level [*Hameed and Lee, 2005*]. The two different polarities of wind anomalies discussed above are well exhibited by the evolution of the NAM index as shown in Figure 2.4. The years shown in Figure

2.4 are the same as in the zonal wind anomaly analysis in Figure 2.3. The values of NAM index tend to be positive while the polar vortex is strong (and cold) and it is negative while it is weak and warm. The color scheme in the figures for the NAM index is chosen to be red in negative (warm) regime and blue in positive (cold) regime. The time-height development of the NAM in each winter shows that the signals emerging from the stratosphere reach the surface in three of the winters. The first and second columns, 1977 winter and 1985 winter show that negative NAM signal (weak westerlies) first appears in December in the lower stratosphere and the signal propagates into the troposphere in January. During the 1989 and 1990 winters as seen in the third and forth columns, the positive signal first appears in December and propagates downward throughout January and February.

Considering the whole 57 years of NCEP period, it is obvious that a number of positive and negative stratospheric events reached the surface. We identified an anomalous event when the amplitude of the NAM index at 10 hPa was greater than 1 or 1.5 times the standard deviation of the entire 57 years of winter months. The result from each winter, the rate of the downward propagation and its relation to the solar cycle and the QBO is presented in chapter 3.

3. Sun-climate mechanism in winter

In this chapter, the differences in the frequencies of the downward propagation of the NAM surface during solar maximum and minimum periods are shown. A much greater fraction of stratospheric perturbations penetrate to the surface during solar maximum conditions than during minimum conditions. This difference is more striking when the zonal wind direction in the tropics is from the west: no stratospheric signals reach the surface when equatorial 50 hPa winds are from the west under solar minimum conditions, and over 50 percent reach the surface under solar maximum conditions.

3.1 Introduction

It has been known for more than a hundred years that changes in the solar cycle apparently produce corresponding changes in weather and climate on the earth [*Lamb*, 1972; *Burroughs*, 1992]. The link between the solar cycle and climate has been a puzzle because the solar energy output changes by only about 0.1 percent during a typical 11 year solar cycle [*Lean and Rind*, 2001], a change that is too small to produce a significant changes at the surface based on the energy budget. A possible clue is that the changes in the output of solar ultraviolet (UV) radiation are significantly greater, up to a few percent during a typical 11-year solar cycle [*Lean,* 2000]. Furthermore, the percent change in the UV radiation is greater at shorter wavelengths. Since the solar UV radiation is the main agent for producing ozone in the stratosphere, the significant changes in ozone with the

solar cycle is expected. Such changes have been verified in observations [*Hood*, 1997] and also in modeling studies [*Shindell et al*., 1999; 2001; *Lee and Smith*, 2003]. Systematic changes in the distribution of ozone result in changes in the temperature and pressure distributions in the stratosphere. It is now recognized that the different thermal and dynamical signatures in the stratosphere between solar maximum and minimum conditions [*Labitzke*, 2001; *Hood*, 2004] and these are modulated by the quasi-biennial oscillation (QBO) of the zonal equatorial winds [*Labitzke*, 2003]. Several studies have demonstrated that solar cycle induced perturbations are large in the upper stratosphere and gradually descend to the lower stratosphere [*Kodera and Kuroda*, 2002; *Gray et al*., 2001; 2004]. *Baldwin and Dunkerton* [1999; 2001] used the northern annular modes to demonstrate that some perturbations in the stratosphere can reach the surface. The northern annular mode (NAM) is the first empirical orthogonal function of geopotential height at each level and thus represents a principal mode of stratospheric circulation. These authors showed that positive and negative anomalies in the stratospheric NAM are generated, and on occasions propagate to the surface maintaining the same sign. In the stratosphere annular mode values are a measure of the strength of the polar vortex, while the near surface annular mode is called the Arctic Oscillation (AO).

We have used the method of *Baldwin and Dunkerton* to investigate downward propagation in solar maximum and minimum conditions. Results show a clear difference: Many more stratospheric perturbations reach the surface in solar maximum conditions than in minimum conditions. Furthermore, no stratospheric signals reach the surface in minimum conditions when the tropical wind in the lower stratosphere is from the west.

3.2 Data : NCEP/NCAR reanalysis

For the present analysis, National Centers for Environmental Prediction/National Center for Atmospheric Research (NCEP/NCAR) reanalysis [*Kalnay et al.*, 1996] monthly mean geopotential height field for 1948-2004 is used to define the annular mode independently at each of the 17 pressure altitudes from 1000hPa to 10hPa. Climatological mean has been removed at each grid point at a given altitude to calculate the monthly geopotential height anomalies. Data are weighted by the square root of cosine of latitude to generate the equal area weight at each grid point.

3.2.1 Evolution of the NCEP/NCAR reanalysis

There were two major changes in the atmospheric observation systems in the last half century [*Kistler and Kalnay*, 1999]. The first one took place during the period 1948 - 1957, when the NH upper air network was gradually improved, and culminated in the International Geophysical Year (IGY) of 1957-58. The second major addition took place with the First Global GARP (Global Atmospheric Research Project) Experiment (FGGE), run in 1978/1979, observing systems relying on remote sensing and communication to provide unprecedented global observation coverage and timely data receipt. From 1979, the TOVS (TIROS-N Operational Vertical Sounder), the first combined infrared/microwave (HIRS/MSU) operational sounder, was used in the reanalysis process. Although satellite data provide global coverage of measurement, their abrupt onset near those years can obviously introduce a bias between before and after FGGE.

Based on the changes of global observing system, the NCEP/NCAR reanalysis data can be distinguished into three stages: the first stage before IGY(1948 – 1957), the second stage after IGY and before FGGE (1957 – 1979), and third stage after FGGE until present.

3.2.2 Reliability of NCEP/NCAR reanalysis

Although the global rawinsonde network is established from June 1957 with the IGY, the NH rawinsonde observations had already been started by 1948. Good data coverage in China started in 1956, and in India by 1950. Before the IGY, there were no observations from most of South America and Antarctica, the network was exceedingly inadequate in the SH. However, in the NH, the upper air observations for the early years actually had some advantages compared with present days. A number of permanent ships started observations in the late 1940's and data at these locations continued in the northern oceans until about 1973-1974. There were weather reconnaissance flights over the northern oceans and to the North Pole during 1947-1960. These, together with the permanent ship rawinsondes from 1948 to 1973 have helped the reanalysis over the oceans during the early years. Winds aloft from radar or visual tracking of balloons (called pilot balloons or pibals) are also an important data source for reanalysis of the early stage. Before FGGE in 1979, NCEP/NCAR reanalysis is based on nonuniformly distributed observations. The analysis error by changes of operational network and by ununiformly distributed resolution can limit the accuracy of the reanalysis. These sources of error can modify the correlation between sites, but they do not limit the reliability of the field properties coherently. In later decades, the reanalysis includes

satellite measurement, which provides global coverage. Although satellite data provide global coverage of measurement, their abrupt onset near those years can obviously introduce a bias between before and after FGGE. After FGGE, many satellite data impact tests were executed, and generally reported strongly positive results in the Southern Hemisphere, but little impact in the Northern Hemisphere [*Mo et al.,* 1995].

3.3 method of analysis

At each pressure level, the annular mode is the first empirical orthogonal function (EOF) of the geopotential height anomalies from 20ºN to 90ºN. Monthly values of the annular mode, spanning the 57-year data record, are calculated at each pressure level by projecting monthly geopotential height anomalies onto the leading EOF patterns. The method of calculation is as described by *Baldwin and Dunkerton* [2001] and Appendix I. The leading EOFs are calculated for extended winter (from October to April) and summer (from May to September), respectively.

3.4 Sun-climate mechanism in NAM for extended winter

3.4.1 Results

Solar activity in each winter is measured by the total number of sunspots observed in each period. Figure 3.1 shows the northern annular mode in the stratosphere-troposphere system for the five winters during 1948-2004 in which solar activity was the maximum in order of highest sunspot numbers. Positive values of the NAM are shown in

blue and negative values in red. The W and E on top of each panel give the direction of the quasi-biennial oscillation (QBO) wind for each month at 50hPa provided by *Naujokat*. Figure 3.1 shows that during the five strongest solar maximum winters, perturbations emerging in the stratosphere reach the surface in four of the winter. The winter of 1979-1980 is the exception because the signal breaks up and does not reach the surface. Of the four signals that reach the surface three are negative events and only one (1989-1990) is a positive event. During negative events the polar vortex is weak and warm, while it is strong and cold in positive events [*Baldwin and Dunkerton*, 2001].

Figure 3.2 shows the northern annular mode during the five winters in which solar activity was the lowest during winter with the weakest solar activity. Figure 3.2 shows that the signals emerging from the stratosphere do not reach the surface in four of the winters, the exception being 1996-1997 when two signals emerge and propagate to the surface.

By expanding the data base with 15 winters with the highest sunspot numbers and 15 winters with the lowest sunspot numbers during 1948-2004, the fraction of the stratosphere-troposphere coupling events are compared. The results for two threshold values for defining the perturbations are given in Table 1: 1.0 and 1.5 times the standard deviation of the northern annular mode. The second line in Table 1 lists the number of signals that occurred at 10hPa level. The third row gives the number of times that the signal reached the surface. There is a significantly greater fraction of the stratospheric events reach the surface under solar maximum conditions than in minimum conditions. The statistical significance of these results is tested using a t-test and is 99% confident.

The last two rows in Table 1 give the ratio classified according to the prevailing zonal wind direction in the tropical lower stratosphere (50hPa). No signals reach the surface in the solar minimum conditions when the wind direction is from the west, while over 50% of the signals reach the surface under solar maximum conditions. Considering 16, 17, 18, or 19 winters of maximum and minimum sunspot numbers did not produce significant changes in ratios in the last three rows of Table 1. Replacing the sunspot numbers by monthly solar UV irradiance (290-295 nm) presented by *Lean* [2000] to identify winters of high and low solar activity also did not change the ratios significantly.

3.4.2 Discussion

The results may be understood in the context of findings by *Gray et al.* [2004] who studied the influence of the solar cycle and the quasi-biennial oscillation on the winter polar vortex in ECMWF Reanalysis data for 1957-2001. They find that the polar vortex in the stratosphere is more disturbed in years in which the wind is from the East than in years when it is from the West, in conformation with the *Holton-Tan* effect. However, they find an important difference in West years between solar minimum and maximum conditions. In solar minimum/West condition, the vortex is anomalously strong throughout the whole winter and an easterly anomaly in the winds does not appear until April. In solar maximum/West condition, an easterly anomaly develops in February and moves poleward and downward by March indicating midwinter warming events. Their results are consistent with previous work by *Labitzke* and coworkers who noted as early as 1982 that major midwinter stratospheric warmings do not occur during the QBO

westerly phase except near solar maxima [*Labitzke*, 1982]. Together with the present results, they suggest that the stable vortex in winters when solar activity is low and winds are from the west then the propagation of stratospheric signals to the surface is unlikely.

The present study shows that the circulation anomalies caused by these stratospheric warmings propagate down to the surface much more frequently under solar maximum conditions than under solar minimum conditions. This suggests that solar perturbation of the stratosphere by ultraviolet radiation variations followed by downward propagation of resulting circulation anomalies to the surface is the principal sun-climate mechanism.

4. The Northern Hemisphere Annular Mode in Summer and Its Relation to Solar Activity Variations in NCEP/NCAR reanalysis

In this chapter, the National Centers for Environmental Prediction/National Center for Atmospheric Research (NCEP/NCAR) reanalysis is used to calculate Empirical Orthogonal Functions (EOF)s of summer geopotential heights in the northern hemisphere at all levels in the troposphere and the stratosphere. Leading patterns in summer stratosphere are distinct from the winter patterns. Also, the leading patterns in the summer stratosphere are distinct from the patterns of the summer troposphere. The summer Northern Hemisphere annular mode (NAM) in the stratosphere has the same sign in the northern hemisphere but shows higher variability at low latitudes unlike the dipolar structure of the winter NAM. A physical interpretation of the summer NAM in the stratosphere is readily apparent because low (high) values of its principal component correspond to warmer (colder) than climatological mean summer conditions in the stratosphere. The summer NAM in the troposphere, on the other hand, is characterized by variability over the Asian monsoon region. Also, the summer NAM in the stratosphere and upper troposphere is correlated with the solar ultra violet (UV) flux such that in solar maximum conditions the stratospheric circulation is more 'summer-like' than average, and it is less 'summer-like' in solar minimum conditions. The summer NAM is thus seen as a potentially useful tool in investigating the sources of variability in the summer atmosphere.

4.1 Introduction

The Northern Hemisphere annular mode (NAM), defined as the first empirical orthogonal function (EOF) of geopotential height has been found to be an important tool in the study of variability of the winter hemisphere [*Thompson and Wallace*; 1998, 2000]. The pattern in sea level pressure in winter is called the Arctic Oscillation and it has been shown to be linked to a large number of regional climatic impacts [e. g., *Thompson and Wallace*, 2001; *Lin et al.,* 2002; *Kodera and Kuroda*, 2003]. The vertical coherence of the winter NAM pattern has been useful in investigations of stratosphere-troposphere interactions [*Baldwin and Dunkerton*, 2001] and the influence of solar activity changes on the atmosphere [*Hameed and Lee*, 2005]. The vertical coherence of the winter NAM and its relation to solar cycle and QBO is discussed in chapter 3.

In this chapter, the Northern Hemisphere annular mode (NAM) in summer and its physical interpretation is discussed. The annular mode in summer has been previously discussed by *Thompson and Wallace* [2000]. They used geopotential heights for all the months of the year in their EOF calculation and noted that it is dominated by the winter variability. They also pointed out that the annular modes exist in all seasons but the coupling between the tropospheric and stratospheric modes occurs only in winter. They did not display the summer NAM pattern in the stratosphere but noted that it is different from the winter NAM in that its meridional scale is larger. *Ogi et al*. [2004] pointed out that if the NAM is calculated using geopotential height data for all the months and its principal component regressed with circulation anomalies in different seasons, misleading results for summer may be obtained. This is because the summer season has

its own unique leading pattern which is overshadowed in the pattern obtained from using data for all months of the year. *Ogi et al.* [2004] did the EOF analysis separately for each month using zonally averaged geopotential height fields from 1000 hPa to 200 hPa, but in the latitudinal domain from 40^{o}N to the Pole, while the calculations of *Thompson and Wallace* [1998, 2000] considered the region 20^{o}N to the Pole.

In EOF analysis, a different choice of the geographical domain can introduce significant differences in the calculated patterns and their principal components. The EOF patterns for the summer season separately for each altitude available in the NCEP-NCAR reanalysis from 1000 hPa to 10 hPa for the domain 20^{o}N to the Pole. It will be seen later that using the extended geographical domain makes an important difference, because the Asian monsoon is a key part of the summer variability in the troposphere. Using the pattern at 10 hPa, it is shown that the low values of its principal component represent an accentuation from the climatological mean summer condition, while the high values correspond to weakening from the climatological summer condition.

van Loon and Labitzke [1998] have calculated the principal component of the leading EOF in July and August at 30 hPa and shown that it has a decadal variation similar to the solar UV flux for 1975-1995. This relationship is investigated at several levels in the stratosphere and troposphere for the extended period 1948 -2004.

In section 4.2 the method of calculation is described and in section 4.3 the structures of the first two EOF modes at 1000 hPa and 10 hPa in summer is discussed and compared to the two leading winter modes. In section 4.4, a physical interpretation of the leading summer mode in the stratosphere is discussed. The coupling between the stratospheric NAM and the solar cycle is investigated in section 4.5. Section 4.6

considers possible sources of stratospheric variability in summer, and the conclusions are presented in section 4.7.

4.2 Methods

NCEP/NCAR reanalysis data from May to September and from 20°N to 90°N are used to define the summer annular mode at each of the 17 pressure levels ranging from 1000 hPa to 10 hPa. Data are weighted by the square root of cosine of latitude to generate the equal area weight at each grid point. The first summer mode is defined as the first Empirical Orthogonal Function (EOF) of the temporal covariance matrix of geopotential height anomalies at each pressure level. Month to month variability of the leading modes of each summer, spanning the 57-year data record, is calculated at each reanalysis pressure level by projecting monthly geopotential height anomalies onto the leading EOF patterns. The EOF for the summer is calculated in precisely the same way as for winter as described in Chapter3, which is the same method used by *Baldwin and Dunkerton* [2001].

It can be reasonably said that the data base for NCEP/NCAR reanalysis are fewer and of poorer quality for the earlier years. However, *Kistler and Kalnay* [1999] point out that there was a considerable network of rawinsonde stations in the northern hemisphere during the late 1940s and early 1950s. The evolution and reliability of the NCEP/NCAR reanalysis are discussed in section 3.2.1 and 3.2.2. In the comparisons of the summer NAM with the solar cycle, as in Figure 4.7, the correlations would improve if the period before 1960 is omitted. However, the disagreement in the earlier period is qualitatively

not different from that of the later period of 1995-2004. It therefore seems less arbitrary to present the whole record.

4. 3 Structure of the NAM during winter and summer

Figure 4.1(a) shows the first EOF of geopotential height variance at 1000 hPa during the extended winter from 1948 to 2004. As has been noted by *Thompson and Wallace* [1998], the surface winter NAM (or the Arctic Oscillation) is characterized by cells in polar and subpolar regions, the Azores High region in the Atlantic basin, and the Hawaiian High in Pacific basin. The NAM in the summer season from May to September is shown in Figure 4.1(c). The summer pattern is also characterized by a dipole zonal structure like the Arctic oscillation. The dipole structure of the 1000 hPa summer pattern was also noted by *Ogi et al.* [2004], who did the analysis for the region 40^{o}N poleward. Comparing Figure 4.1(a) and 4.1(c), the main difference is that in the winter mode the highest variability is over the polar region, while in the summer it is over the Asian monsoon region. As seen in Figure 4.1(c), the first summer mode at 1000 hPa describes a zonal circulation around the polar vortex, as in winter, and contains 17% of geopotential height variability.

Figure 4.1(b) shows the second EOF pattern for winter. The highest variance in this mode is over the Aleutian Low and it is anti-correlated with the variability over the Icelandic Low. Figure 4.1(d) shows the second EOF during the summer. One finds that the overall pattern of variability in the second summer mode is similar to the first mode in winter; in the second summer EOF the highest amplitudes are over the Atlantic sub-polar

region, and a clear signature of the North Atlantic Oscillation (NAO) is present similar to the first EOF in winter (shown in Figure 4.1(a)). Therefore, if the first winter NAM is regressed on the summer geopotential height data to estimate summer variability, the result is likely to be more representative of the second summer EOF than the first summer pattern.

Figure 4.2 compares the first two EOF patterns for winter and summer at 10 hPa. The first winter pattern (Figure 4.2 (a)) explains 45 percent of the variance for the 1948-2004 period, while the corresponding summer pattern explains 73 percent of the variance. The fact that the first EOF pattern in summer explains such a large fraction of variance is an indication of the simpler character of summer circulation in the stratosphere. While the winter pattern has the highest amplitudes in the polar region and the well known dipole structure such that the variability in the sub-tropical region is of the opposite sign, the summer pattern is characterized by variability of the same sign throughout the northern hemisphere, with the highest amplitudes in the tropics and gradually decreasing towards the high latitudes. In Figure 4.2(d) the second EOF for summer is shown, just as at 1000 hPa, it has a structure similar to the first winter EOF. It has a more pronounced dipolar contrast between the polar and the tropical regions than in the winter NAM seen in Figure 4.2(a). By contrast the second winter EOF in Figure 4.2(b) emphasizes the opposite modes of variation between the North Atlantic-North Europe and North Pacific regions**.** The leading EOF patterns at all pressure levels in the stratosphere are generally similar to the 10 hPa patterns shown in Figure 4.2. Similarly, the leading EOF patterns at the different pressure levels in the troposphere are similar to 1000 hPa patterns shown in Figure 4.1. However the patterns in the stratosphere and the troposphere are different

from each other and their principal components are not correlated during the summer, as was noted by *Thompson and Wallace* [2000].

4. 4 Physical Significance of the summer NAM

4.4.1 Stratosphere

The variance contributed by the first mode to the total variance of the geopotential height is greatest at 10 hPa (73%). Therefore, the physical meaning of the summer NAM is investigated at the 10 hPa level. Two groups of the geopotential height fields are classified. High NAM index months are defined as those in which the NAM index is above one standard deviation from the mean of the 57 years of summer index values (51 months). The Low NAM index months are similarly defined as those in which the index is below one standard deviation (42 months).

In the climatological mean conditions of summer, there are high temperatures over the arctic stratosphere caused by direct absorption of UV radiation in comparison with lower latitudes. Hence the geopotential heights in the polar region are high and decrease toward the subtropics, giving the geopotential height distribution a dome-like shape centered on the polar region.

As shown in Figure 4.3, the geopotential height is higher in NH when the summer NAM index is low in comparison with the high NAM condition. Moreover, the low NAM is characterized by a larger meridional height gradient. The geopotential height over the polar region is greater by nearly 200 meters in Low NAM than in High NAM.

In Figures 4.4(a) and 4.4(b) the zonal wind velocities for Low and High NAM conditions are compared, respectively. There is a strong zonally symmetric easterly circulation with very little deformation during the high NAM periods (Figure 4.4(b)). The position of the strongest summer easterly jet in the low latitudes is shifted northward during high NAM periods. However, during low NAM conditions (Figure 4.4(a)), the easterly circulation is stronger poleward of about 45^{o}N. The stronger zonal circulation in low NAM vs. high NAM conditions is consistent with the geopotential height distribution differences between Figures 4.3(a) and 4.3(b).

Figure 4.5(a) shows the temperature distribution at 10 hPa in low NAM conditions and Figure 4.5(b) gives the temperature distribution for the high NAM composite. The temperature is colder during high NAM conditions, especially over the polar region where the temperature difference is 4 to 6K between the extremes of NAM. This suggests that the weaker circumpolar circulation during high NAM period allows colder air from lower latitudes to mix into the polar region, resulting in the cold anomalies there and a lowering of the geopotential heights.

From Figures 4.3 - 4.5, the summer NAM describes the hemisphere wide variability of the summer stratosphere between conditions which are more ‘summer-like’ (low NAM) and less ‘summer-like’ (high NAM). In the less ‘summer-like’ conditions, the temperatures are colder, the easterly zonal circulation is weaker, and the geopotential height distribution is less dome-like than in the climatologically averaged summer condition. In the low NAM conditions anomalies opposite to these prevail.

4.4.2 Troposphere

In Figure 4.1(c) for the leading EOF pattern the largest of variability is over the Asian monsoon region. The principal component of the leading pattern at 1000 hPa is used to define high NAM index months as those in which it is above one standard deviation from the mean of the 57 years. The low NAM index months are similarly defined as those in which the index is below one standard deviation. The composites show that the variability in the Asian monsoon region dominates the variability associated with the leading mode in summer troposphere. As an example, the difference in temperatures in the northern hemisphere between low NAM and high NAM in July-August is shown in Figure 4.6. It is characterized by warmer temperature over the Asian continent, and colder temperatures over Siberia. *Greatbatch and Rong* [2006] have shown that SLPs in NCEP/NCAR reanalyses over a region around Mongolia are biased lower than ERA 40 during 1958-68. This region is a small part of the positive Asian node in Fig. 4.1(c), and it is likely that the pattern may be different in this region if ERA 40 data were used for the analysis.

4.5 Solar cycle and the summer NAM

van Loon and Labitzke [1998] used NCEP-NCAR geopotential height data averaged for July and August during 1974-1995, and calculated the first EOF at 30 hPa. Their Figure 8 compares the first PC with the 10.7 cm solar flux, and they point out the dominance of the 11 year cycle in both curves. The first PC at 30 hPa is compared with

solar UV flux (200-295nm) in Figure 4.7 for the extended period 1948-2004. The agreement between the two curves is weakened after 1995, and it is also less strong during 1948-1975. Nonetheless, the correlation coefficient between the two time series is -0.40. It is shown by *Quenouille* that a good estimate of the effective number of independent observations entering into the calculation of cross-correlation coefficients is given by

$$N/(1+2r_1r_1^{'}+2r_2r_2^{'}+\cdots), \qquad (1)$$

where N is the number of data points in each of the two series, r_1 and $r_1^{'}$ are the lag-one autocorrelations of the two series, r_2 and $r_2^{'}$ the lag-two auto-correlation of the two series, *etc*. When the autocorrelations in the two series are taken into account using *Quenouille*'s procedure as described by *Angel and Korshover* [1981], the number of independent data points is reduced from 57 to 26. The correlation coefficient is statistically significant at the 95% confidence level for the 1948-2004 periods.

The results are given in Table 2. Each value gives the correlation coefficient between the principal component of the first EOF for that time period and pressure level with the UV flux (200-295nm). The effective sample size is listed in parentheses in each case. Correlations with statistical confidence level of 95% or higher are shown in bold.

The second column in the Table 2 lists the variance in May to September geopotential height during 1948-2004 that is explained by the first EOF of the extended summer. The square of the correlation coefficient gives the fraction of the variance in the PC that can be attributed to solar influence. For example, the correlation coefficient for the extended summer at 50 hPa is -0.38, and the variance explained by the first PC is

58 %. Thus about 8 percent of the geopotential height variance during (May-September) is attributable to the solar cycle.

In Table 2, the strongest correlations are in the lower stratosphere, at 50 hPa and 70 hPa, and are during the months of July and August. Since the ozone maximum is also in the lower stratosphere, the results in Table 2 are consistent with the view that the influence of solar variability on the summer stratosphere is primarily via absorption of UV radiation by ozone, which in turn affect the dynamics. Using Total Ozone Mapping Spectrometer (TOMS) ozone data, *Hood* [1997; 2004] has shown that the solar signal is positive and significant with ozone in the lower stratosphere for June, July and August at low latitudes up to 30ºN. *Hood* [1997] estimated that about 85% of the solar cycle variation of global mean total column ozone amount comes from below 30 hPa. Although the results by *Hood* [1997] are for low latitudes only, the agreement with the results in Table 2 is encouraging. Of course, the fact that the correlations are highest in the lower stratosphere cannot be taken as proof that the effect is largest there, because other simultaneous influences are possible. A global analysis of the satellite ozone data now available would be of much interest in better understanding ozone's role in modulating solar influence on the stratosphere.

The correlations between the UV flux and PC1 are negative, i.e., solar maximum (minimum) conditions correspond to lower (higher) summer NAM. This suggests, according to the physical interpretation of summer NAM discussed above in section 4.4, that the stratosphere is more 'summer-like' when the solar cycle is near a maximum. This means that the zonal easterly wind flow is stronger and the temperatures are higher than normal. By contrast, low solar activity corresponds to higher NAM conditions in

which the stratosphere behaves less 'summer-like'. The solar cycle effects therefore appear as small amplitude modulations of the annual cycle, as suggested by *Kodera and Kuroda* [2002].

Labitzke [2003] has shown that the geopotential height difference between solar maximum and minimum is greater in the QBO East phase than in the West phase for the month of July. However, our calculations showed that the correlation between the first principal component and UV flux does not change significantly between the QBO phases during summer. This difference may arise because of our use of the EOFs which represent hemisphere-wide patterns while the differentiation between east and west phases of the QBO was shown by *Labitzke* [2003] in particular latitude bands.

4.6 Sources of variability in the summer stratosphere

Labitzke [2003] suggested that the effects of solar cycle in the stratosphere may be seen more easily in the summer than in winter because of low level of variability in the summer season. The NAM explains a greater portion of the geopotential variance in summer than in winter, and the significant anti-correlations of the summer NAM with the solar cycle shown in Table 2 verify *Labitzke*'s suggestion. Important questions remain, however, about the mechanism of solar UV's interaction with the atmosphere, including the processes that can transfer the solar signal to the lower troposphere. A related topic that merits further investigation is the nature of the variability in the summer stratosphere and its possible sources.

Numerous observational studies have documented traveling and stationary waves in the stratosphere in the summer season. *Muench* [1968], *Randel* [1993], *Miles et al.* [1994] and studies cited by these authors showed westward propagating Rossby waves in the summer stratosphere in ozone, temperature, and velocity fields.

What processes contribute to the generation of disturbances in the stratosphere? One possible source is the differential heating caused by absorption of UV radiation by the varying concentrations of ozone. Another possibility is the impact of vertically propagating waves from the troposphere.

Edmon et al. [1980] and *Wagner and Bowman* [2000] calculated E-P flux vectors for summer months in the Northern Hemisphere. Both sets of results show that waves propagate from the troposphere vertically into the stratosphere. A region of flux divergence is seen in the middle latitudes upper troposphere from which wave activity propagates upwards. Most of the stratosphere is a region of convergence for E-P flux.

The *Charney-Drazin* theorem does not rule out planetary waves in the summer. It states that vertical propagation is present when the mean zonal flow $\bar{u}$ relative to phase speed c in the lower stratosphere is westerly, but less than a threshold value [*Charney and Drazin*, 1961].

$$0 < \bar{u} - c < \overline{u_c} \,. \qquad (2)$$

This means that traveling waves can propagate vertically into the stratosphere with easterly winds, as long as their westward phase speeds are faster than the zonal mean wind velocity. *Wagner and Bowman* [2000] analyzed daily data for the summer months

in Northern Hemisphere for 1992-1998 and showed that the wave power shifts from eastward propagating waves in the upper troposphere to dominantly westward propagating waves in the middle stratosphere, consistent with the phase speed constraint given by the *Charney-Drazin* theorem. However, their analysis also showed that the amplitudes of the waves in the summer stratosphere are extremely weak compared to the waves in winter. The sources of summer variability deserve further study.

4.7 Conclusions

The leading EOF patterns of the summer geopotential heights in the northern hemisphere are distinct from the patterns of the winter. Both in the stratosphere and the troposphere the second EOF of the summer geopotential height has structure similar to the first EOF in winter. If the principal components of the leading mode in winter are regressed on summer circulation data, the resulting statistics are likely to represent the second summer EOF pattern. In terms of physical interpretation, the low NAM in the stratosphere represents an enhancement of the average summer condition in the geopotential height, temperature and velocity distributions and the high NAM is a diminution of the average summer condition. In the troposphere the summer NAM is characterized by variability of the Asian monsoon; it however, represents a much smaller fraction off the total variance than in the stratosphere. It was found that the summer NAM in the stratosphere and upper troposphere is inversely correlated with the solar UV flux, i.e., in solar maximum conditions the stratospheric circulation is more 'summer-like' than average, and it is less 'summer-like' in solar minimum conditions. The

strongest correlations with the solar UV radiation are in the lower stratosphere. Since the EOF patterns in the stratosphere and troposphere are not coupled, a major unanswered question is about the mechanism by which solar cycle induced changes in the summer stratosphere can influence surface climate.

5. The Northern Annular Mode in Summer and its Relation to Solar Activity Variations in the GISS ModelE

5.1 Northern annular modes in simulations of Present day (PD) and Pre-industrial (PI)

In this chapter, the solar influence on atmospheric circulation is studied based on the ModelE version of the Goddard Institute for Space Studies (GISS) atmospheric and ocean general circulation model (AOGCM) simulation experiments. The simulations are forced not only with the present day or pre-industrial (PD or PI) greenhouse gas and aerosol conditions but also with changes in solar irradiance under perpetual solar maximum and perpetual solar minimum conditions, respectively. The maximum condition run (MAX) and the minimum condition run (MIN) are simulations with different direct solar ultraviolet (UV) radiation which produces stratospheric and tropospheric ozone changes via a 3-dimensional chemical model calculation.

5.1.1 Model description and experiment setup

The GISS ModelE simulations are performed separately for two solar activity conditions: solar maximum and solar minimum with present day (PD) or pre-industrial (PI) greenhouse gas and aerosol conditions. The simulations are forced with an 11-year solar cycle irradiance variation. The full solar irradiance variation corresponds to ~0.19 W/m² maximum minus minimum instantaneous radiative forcing at the tropopause,

equivalent to 1.1 W/m² change in solar irradiance at the top of the atmosphere. The variation increases markedly at UV wavelengths, where the flux changes by several percent over a solar cycle (the total irradiance variation is only about 0.1%). The spectrally varying solar irradiance perturbation inputted to the 3-dimensional chemistry coupled atmospheric GCM produces stratospheric and tropospheric ozone changes [*Shindell et al*., 2006a].

In the PI experiment, the concentrations of long-lived gases and aerosols and emission of short-lived gases are set to pre-industrial levels. Therefore, the PI MAX and PI MIN simulations have the +1/2 and -1/2 of the solar cycle irradiance changes and pre-industrial greenhouse gas conditions. The PI MIN condition represents the era of reduced solar activity in pre-industrial period such as Maunder Minimum (~1645-1715). The solar signal in the pre-industrial period is presented as differences between the +1/2 and -1/2 solar cycle runs, which provides an appropriate simulation of the climate response to an extended period of altered irradiance.

It is already known that the pre-industrial chemical conditions induce more ozone in the upper and lower stratosphere because the anthropogenic halogens are absent and approximately 60% less methane causes a drier stratosphere [*Shindell et al.,* 2001]. Ozone's temperature sensitivity is governed by catalytic cycles involving chlorine, nitrogen, hydrogen, and oxygen radicals. The temperature dependence of the rate-limiting reactions for the chlorine, nitrogen, and hydrogen cycles is weakly negative, whereas for oxygen it is strongly positive. The relative importance of the oxygen cycle is greater during the pre-industrial period, leading to large increases in overall sensitivity in the upper stratosphere. Therefore, Ozone's temperature sensitivity is increased

throughout the upper stratosphere, more than twice at 3hPa relative to the present day. Solar heating then speeds up chemical destruction more than irradiance enhances photolytic production, so that ozone concentration decreases with solar irradiance. Thus, the reduced irradiance in pre-industrial period such as Maunder Minimum leads to increased upper stratospheric ozone.

The GISS atmospheric GCM used in this chapter is coupled to a simplified thermodynamic mixed-layer ocean model, where the SST is allowed to adjust to different atmospheric fluxes but the ocean heat transport is held constant. The oceanic heat convergence (the q-fluxes) into the isothermal mixed layer is calculated as a residual given by the heat and mass fluxes at the base of the atmosphere. The 23-layer version of ModelE resolves the stratosphere, extending from the surface to 0.02 hPa, and includes a parameterization of gravity-wave drag. The GCM output is given on a 4º (latitude) x 5º (longitude) grid. In this ModelE version, a new cloud microphysical scheme and land snow and lake schemes are used and atmospheric turbulence is calculated over the whole column. Further details on the model and data-model comparisons are given by *Schmidt et al.* [2006].

5.1.2 Method

To define the winter annular mode at each of the 23 pressure levels ranging from 972 hPa to 0.017 hPa, the monthly averaged geopotential height fields from model outputs of the simulations from 20ºN to 90ºN are analyzed. The same EOF analysis method is used as already described in Chapter 3.3.

5.1.3 Structure of the northern annular modes during winter and summer in ModelE

Thompson and Wallace [1998, 2000] suggested that the dynamical coupling between the stratosphere and troposphere is controlled not as a wave-like pattern in the tropospheric circulation, but as vertically coherent variance pattern of the annular modes, characterized by zonally symmetric low frequency fluctuations in geopotential heights between the polar region and the middle latitudes. *Baldwin and Dunkerton* [2001] later demonstrated that the deep vertical coupling associated with the northern annular mode (NAM) does not occur synchronously, but that changes in the NAM at stratospheric levels tend to precede the same-signed changes in the NAM at tropospheric levels by ~60days.

After *Thompson and Wallace* [1998], the structure and the variability of NAM has been widely viewed, both in observations and models, by many studies as the dominant mode that has a strong zonally symmetric or annular component [e.g., *Fyfe et al*. 1999; *Shindell et al*. 1999a; *Shindell et al*. 2001; *Limpasuvan and Hartmann* 2000; and *Miller et al.* 2006].

Figure 5.1(a) and 5.1(b) show the first and the second EOF of geopotential height variance at 765 hPa during extended winter (October to April) from the PD simulation. The first EOF generally has the character of the northern annular mode with cells in polar and subpolar regions; one in Atlantic basin, and the other in Pacific basin. The variance explained by this mode of variability is 27% which is comparable to that of NCEP/NCAR reanalysis. Compared with the first EOF pattern of NCEP/NCAR reanalysis, the two

centers of action are shifted toward the Eurasian continent. The Pacific High is moved eastward and the Atlantic high westward. The second EOF pattern in Figure 5.1(b) shows the highest variance over the Aleutian Low as shown in NCEP/NCAR reanalysis pattern in Figure 4.1. However, the anti-correlation between Aleutian Low and Icelandic Low shown in NCEP/NCAR reanalysis pattern does not appear in the second EOF pattern in the model.

Figure 5.1(c) and 5.1(d) show the first and the second EOF of geopotential height variance at 765 hPa during summer season from May to September from the PD simulation. The second EOF of summer does not show any physically meaningful feature. However, the first summer pattern is also characterized by a dipole zonal structure like the winter northern annular mode which describes a zonal circulation around the polar vortex, and contains 18% of geopotential height variability. With the highest amplitudes of variability in Atlantic basin and Europe, this pattern is similar to the signatures of the North Atlantic Oscillation (NAO).

Figure 5.2 shows the first two EOF patterns for winter and summer at 7hPa from the PD simulation. The first winter pattern in Figure 5.2(a) explains 33% of variance and represents the second EOF from the NCEP/NCAR reanalysis, while the second winter pattern in Figure 5.2(b) explains 28% of variance and represents the first EOF of the NCEP/NCAR. The summer pattern is characterized by the variability with the same sign throughout the northern hemisphere, with the highest amplitudes in the tropics that gradually decreasing towards the high latitudes. The second mode also shows similar pattern with decreasing variability from positive to negative as the latitude increases.

Figure 5.3 shows the first two EOF patterns for winter and summer at 1hPa. The first winter pattern in Figure 5.3(a) explains 45% of the variance and represents the second NCEP/NCAR reanalysis pattern, while the second winter pattern in Figure 5.3(b) explains 23% of variance and represents the first NCEP/NCAR pattern. The first summer mode is similar to that of 7hPa and is characterized by the variability with the same sign throughout the northern hemisphere, with the highest amplitudes in the tropics that gradually decreasing towards the high latitudes. The second mode also shows the same pattern with decreasing variability from positive to negative as the latitude increases.

5.1.4 The comparison of the northern annular modes in GISS/ModelE : PI and PD

In this section, the structure of the NAM in the atmospheric GCM is reviewed both in the PI and PD simulations. The variance explained by the leading modes in EOF for the region poleward of 20ºN from each simulation is compared to those from NCEP (table 3 and table 4). In all cases, the leading modes are well separated from the other eigenmodes as according to the criterion of *North et al.* [1982] which will be explained in Appendix I. In the lower troposphere (765 hPa), the model represents more variance. It is already pointed out by *Miller et al.* [2006] that the models generally simulate the observed variance in the SLP EOF analysis, but organize too much of the variability into the annular mode.

The changes in the magnitude of the northern annular mode between the PI and PD simulations can be interpreted as the signature of large scale low frequency climate

response to the anthropogenic forcing by changes in the concentration of greenhouse gases and aerosols. To estimate the amplitude of the NAM trend associated with the anthropogenic greenhouse and aerosol forcing, the NAM indexes in the PI and PD periods are generated from the identically fixed EOF pattern. The difference of the winter NAM index between the PD and PI shows an apparent positive phase of the pattern, in PD conditions (Figure 5.4). This result is 95% significant with *Student's t*-test above 100 hPa. Many of the observational and numerical evidences suggest that the winter NAM index shows positive trend of the pattern, in recent decades. [*Thompson and Wallace*, 1998; *Fyfe et al*., 1999; *Shindell et al*., 1999; *Thompson and Wallace*, 2000; *Gillet et al*., 2002; *Miller et al*., 2006].

5.1.5 The variability of summer NAM index in ModelE

It is noticeable in Figure 5.5 that the standard deviation of NAM index is larger in solar PD MIN run than PD MAX run throughout summer stratosphere when the pressure level is lower than 300hPa. This means that the variability of summer NAM index which represents the amplitude of the large scale variability of the northern hemisphere is greater throughout the mid-troposphere and stratosphere in MIN than in MAX. The *F*-test is applied to compare the variability of two simulated climates. The difference of the standard deviation is 90% significant in the upper stratosphere (44- 110 hPa) when the number of independent samples is estimated to be 40 for each simulation ($N_{MAX} \approx N_{MIN} \approx 40$). In that case, the non rejection region for a test conducted at the

90% confidence level for a hypothesis $H_a : {\sigma_{MIN}}^2 \rangle {\sigma_{MAX}}^2$ is [0, 1.51]. The difference of NAM index variability does not appear in winter season (not shown).

5.2 The Present day (PD) Northern Annular Mode in Summer and Its Relation to Solar Activity Variations in the GISS ModelE

In this section, the annular modes of the summer geopotential heights in the northern hemisphere stratosphere and troposphere in the GISS ModelE are compared with those in the NCEP/NCAR reanalysis. In the stratosphere, the summer NAM obtained from NCEP/NCAR reanalysis as well as from the ModelE simulations has the same sign throughout the northern hemisphere, but shows greater variability at low latitudes. The patterns in both analyses are consistent with the interpretation that low NAM conditions represent an enhancement of the seasonal difference between the summer and the annual averages of geopotential height, temperature and velocity distributions, while the reverse holds for high NAM conditions. Composite analysis of high and low NAM cases in both model and observation suggests that the summer stratosphere is more "summer-like" when the solar activity is near a maximum. This means that the zonal easterly wind flow is stronger and the temperature is higher than normal. Thus increased irradiance favors a low summer NAM. A quantitative comparison of the anti-correlation between the NAM and the solar forcing is presented in the model and in the observation, both of which show lower/higher NAM index in solar maximum/minimum conditions. The temperature fluctuations in simulated solar

minimum conditions are greater than in solar maximum throughout the summer stratosphere.

The summer NAM in the troposphere obtained from NCEP/NCAR reanalysis has a dipolar zonal structure with maximum variability over the Asian monsoon region. The corresponding EOF in ModelE has a qualitatively similar structure but with less variability in the Asian monsoon region which is displaced eastward of its observed position. In both the NCEP/NCAR reanalysis and the GCM the negative anomalies associated with the NAM in the Euro-Atlantic and Aleutian island regions are enhanced in the solar minimum conditions, though the results are not statistically significant.

5.2.1 The summer northern annular modes in ModelE

The absorption of solar ultraviolet radiation by ozone creates heating in the stratosphere. Heating maximizes in the polar region in summer and this creates a meridional temperature gradient that induces an easterly jet. *Wagner and Bowman* [2000] calculated the *Eliassen-Palm* (E-P) flux vectors using the UKMO stratospheric analysis and showed that wave activity propagates vertically into the stratosphere in the presence of easterly winds during the summer time. This suggests that stratospheric dynamics in the summer is not entirely dependent on radiative forcing but is influenced by interaction with atmospheric waves propagating up to the stratosphere.

The Northern Annular Mode (NAM) in the summer geopotential heights in the stratosphere and troposphere using NCEP/NCAR reanalysis data is shown in the chapter4. Considering the first EOF of 10hPa geopotential heights for 1948-2004, it is shown that

the structure of the summer NAM in the stratosphere is different from that of the winter NAM. The summer NAM pattern in the stratosphere affords a physically consistent interpretation in that the low NAM represents an enhancement of the average summer condition and the high NAM represents a weakening of the average summer condition. In the less summer-like conditions characteristic of high NAM, the temperature is colder, the easterly zonal circulation is weaker and the meridional gradient of geopotential height is more negative than average summer conditions. It is also shown that the principal components of the first EOF in the stratosphere and upper troposphere are inversely correlated with the solar ultra violet (UV) flux, i.e., in solar maximum conditions the stratospheric circulation is more summer-like than average and the NAM index is low, while in the solar minimum case, it is less summer-like and the NAM index is high. The purpose of this section is to investigate the summer NAM in the stratosphere and in the troposphere and its response to the solar activity from the ModelE version of the Goddard Institute for Space Studies (GISS) atmospheric general circulation model (GCM). In the previous chapter, the NAM correlation with the solar activity was found from a time series analysis of the NCEP/NCAR reanalysis. To better understand the physical causes and significance of the apparent summer correlation between solar output and the NAM, the NAM index response to solar forcing in the model experiments is estimated.

5.2.2 Structure of the summer northern annular modes in ModelE compared with NCEP/NCAR reanalysis

The first EOF patterns of geopotential height anomalies in the upper stratosphere from May to September, defined as the summer northern annular modes (NAM), are shown in Figure 5.6. In the GISS ModelE output, the summer NAM explains about 41% of the total variance of the domain, while the corresponding fraction is 73% for the reanalysis. Nevertheless, the spatial structure of the leading mode derived from the model simulation appears remarkably similar to that from the observations. For both the model and the reanalysis, the summer mode is characterized by a large degree of zonal symmetry and by the amplitude being highest in the tropics and monotonically decreasing towards the higher latitudes. We define the polarity of the principal component at this level as positive (high NAM) for an accentuation of the pattern which represents the rapid decrease of geopotential height from the polar cap toward the tropics.

In the troposphere, the model does not produce coherent EOF patterns near the surface. This may reflect distortion of the height field due to poor representation of boundary layer fluxes in the model or the strong influence of topography in the relatively coarse model grid, despite the model's use of sigma levels in the troposphere. The lowest level at which a coherent EOF pattern is obtained is 765 hPa, and it is compared with the NCEP/NCAR EOF at 850 hPa in Figure 5.7. In each dataset, the pattern is characterized by a dipole zonal structure like the winter northern annular mode which describes a zonal circulation around the polar vortex and meridional contrast between the high latitudes and the midlatitudes. With the highest amplitudes of variability in the Atlantic basin and Europe, this leading EOF pattern of ModelE is similar to the North Atlantic Oscillation (NAO) signature. Compared with the first EOF pattern of NCEP/NCAR reanalysis, the dominant positive center of action over Asia in the ModelE is shifted towards the east.

This suggests that the Asian summer monsoon simulated in the ModelE is weaker than that in NCEP/NCAR, and its region of maximum intensity is displaced to the east. The first summer mode explains 18 % (16%) of the variance in the ModelE (NCEP/NCAR) in the domain at this level. Overall, the first summer mode in the troposphere derived from the ModelE appears broadly similar to that of the observations in both structure and amplitude.

5.2.3 Sun-Climate coupling during summer in GISS/ModelE

Dynamic coupling between the stratosphere and the troposphere is expected to be reduced in summer compared to winter due to the dominating easterlies in the summer stratosphere which obstruct the vertical propagation of planetary waves [*Charney and Drazin*, 1961]. Therefore, solar induced circulation anomalies in the middle atmosphere are less likely to be amplified by the planetary scale Rossby waves and propagated downward through the stratosphere in comparison with the winter season.

On the other hand, the sun-middle atmosphere connection could be enhanced in summer via sun-ozone interactions, due to the migration of the summer hemisphere toward the sun. The prolonged UV irradiation input to the summer hemisphere not only produces more ozone in the stratosphere via photochemical processes, but is also absorbed by ozone, which leads to increased temperature. This radiative mechanism can amplify the solar signal in the stratosphere through a positive feedback with the ozone concentration modulated by dynamical feedbacks [*Geller*, 2006].

To examine this hypothesis, namely, that the solar-ozone interaction may create temperature and circulation anomalies in the upper stratosphere during the summer, the summer NAM indexes in the MAX and MIN runs are compared. But first we examine the summer NAM in the model further to see if its physical interpretation is consistent with that obtained from NCEP/NCAR reanalysis.

5.2.4 Physical Significance of the summer NAM in GISS/ModelE

The amplitude of the principal component of the first EOF at 7 hPa is called the NAM index in the discussion below. For composite analysis, high NAM index months are then defined as those in which its value is above one standard deviation from the mean of the 17 years outputs (12 months for MAX run and 16 months for MIN run). The low NAM index months are similarly defined as those in which it is below one standard deviation (11 months for MAX run and 14 months for MIN run).

In Figure 5.8, the geopotential height fields at 7hPa between low and high NAM conditions are compared for GISS ModelE MAX and MIN runs, respectively. In the climatological mean conditions in summer, there are high temperatures over the arctic stratosphere caused by direct absorption of UV radiation in comparison with lower latitudes. The geopotential heights in the polar region are high and decrease toward the subtropics, giving the geopotential height distribution over the summer stratosphere a dome-like shape centered on the polar region.

As shown in the figure, the model analysis shows that the geopotential height is greater throughout the domain (20ºN-90ºN) when the summer NAM index is low in comparison with the high NAM condition. Moreover, the low NAM is characterized by a smaller meridional height decrease from pole to low latitudes in both runs. Thus the low NAM represents an accentuation of the mean geopotential height distribution with greater height at each location and a more dome like structure. Similarly the high NAM regime is characterized by negative height anomalies everywhere with respect to the mean summer state.

Lee and Hameed [2007] showed that the correlations between the UV flux and NAM index are negative, i.e., solar maximum/minimum conditions correspond to lower/higher summer NAM with the NCEP/NCAR reanalysis. In figure 5.9, the response of NAM index to the solar forcing in the model is shown and compared with those of NCEP/NCAR reanalysis. For the ModelE, the principal components are calculated for MAX and MIN simulations as described before. For the NCEP/NCAR reanalysis, the summer months with the monthly mean UV flux [*Lean*, 2000] above/below one standard deviation from the mean are grouped as solar maximum/minimum (60 months/63 months). According to this criterion, the months with 290-295nm UV flux greater/smaller than 12.26/12.15W/m² are sampled as solar maximum/minimum. In both model and observation, the NAM indexes are lower in solar maximum than in the solar minimum within 99% significant level (Table 5). The variance of the NAM index is greater in MIN than in MAX in the model, while it is greater in solar maximum than in solar minimum in the observation. The amplitude of NAM variability of the model is less than that of the NCEP/NCAR data.

5.2.5 Response of the summer NAM in the stratosphere to solar variability

The difference between the low and the high NAM composites of the geopotential height has positive height differences throughout the hemisphere in both MAX and MIN (shown in Figure 5.10). The composites of the difference fields show the unexpected pattern which has the maximum height anomalies in the pole but not in the low latitudes where the maximum variability exists in the EOF pattern. This is because the geopotential height field itself in the summer stratosphere has a strong meridional gradient and is decreasing with latitudes in the summer stratosphere as seen in Figure 5.8. Therefore, the composites of the difference fields show the pattern which has the maximum height anomalies in the pole but not in the low latitudes because the original height is much greater in the high latitudes compare to the low latitudes. Quantifying this difference with respect to the NAM index, it increases from 60m/100m in MAX/MIN in the subtropics to 240 m in the polar region when the 7 hPa NAM index changes from the one standard deviation below the mean to the one standard deviation above the mean. This is in good agreement to the corresponding increase from 100 m to 230 m found in NCEP/NCAR reanalysis data at 10 hPa level.

The zonal wind velocities for the low and high NAM conditions are compared for MAX and MIN runs in Figure 5.11. There is a strong zonally symmetric easterly circulation with very little deformation during low NAM case. The stronger zonal circulation in low NAM vs. high NAM conditions in both MAX and MIN is consistent with the characteristics found in geopotential height differences as shown in Figure 5.10,

and with the interpretation that the low NAM regime in the model represents an enhancement of the mean summer circulation, analogous to the result obtained from NCEP/NCAR reanalysis. The maximum easterly wind velocities at 7 hPa are about -20 m/s for both MAX and MIN simulations, and the amplitude of NAM variability in the zonal wind velocity is ~5 m/s when the 7 hPa NAM index changes from the one standard deviation below the mean to the one standard deviation above the mean. Both the mean wind field itself and the amplitude of the difference to the NAM variability are comparable to those found in observation. The maximum easterly wind velocity is about -25m/s and the amplitude of NAM variability is 5~10 m/s in the analysis of NCEP/NCAR data at 10hPa level.

In Figure 5.12, the difference of zonal wind velocities at 7hPa between low and high NAM conditions are compared for MAX and MIN runs, respectively. The zonal wind difference shows negative values (more easterly flow) throughout the hemisphere in MAX conditions, while the differences become zero or slightly positive in the tropics in MIN conditions.

Figure 5.13 shows the temperature distribution at 7hPa in low NAM conditions and in high NAM conditions for MAX and MIN simulations, respectively. As shown from NCEP/NCAR reanalysis composites, the temperature is colder during high NAM conditions, especially over the polar region.

Figure 5.14 shows the temperature difference at 7hPa between low and high NAM conditions for MAX and MIN runs. As expected, the temperature difference between two extreme phases is positive in the domain (20ºN to 90ºN) of summer hemisphere and about 3 K over polar region in both cases. The difference in the tropics is

between 0- 0.5 K in MAX conditions and is between 0.5 – 1.0 K in MIN conditions. This can be anticipated as the geopotential height differences were also greater in solar MIN than in MAX (Fig. 5.10). The amplitude of the temperature difference appeared in the NCEP/NCAR analysis is 2-5 K throughout the analysis period.

According to the physical interpretation of summer NAM discussed above in section 4.3, the anti-correlation between the solar flux and the NAM suggests that the summer stratosphere is more "summer-like" when the solar activity is near a maximum. This means that the zonal easterly wind flow is stronger and the temperatures are higher than normal. By contrast, low solar activity corresponds to higher NAM conditions in which the stratosphere behaves less "summer-like". This hypothesis is verified from ModelE temperature response to solar UV variability shown in Figure 5.15. The average summer hemispheric temperature responses to different solar activity conditions confirm that the summer stratosphere is more "summer-like" when solar UV is stronger. The temperature response to the solar forcing, which is estimated from the difference in the average 7 hPa temperature between MAX and MIN simulation, is 0.6 K in polar region and 0.3 K in midlatitudes except in the middle of Asian continent (Figure 5.16). The differences in the temperature are significant throughout the hemisphere at the 95% significant level based on the *Student t*-test, except in the middle of the Asian continent.

5.2.6 Response of the summer NAM in the troposphere to solar variability

We have seen that the summer leading EOF pattern in the lower troposphere has a dipole zonal structure with fluctuations of opposite signs at the high and the mid-latitudes

(Figure 5.7). In the NCEP/NCAR reanalysis, the dominant mid-latitude positive center is over the Asian monsoon region, while in the ModelE this center is weaker and shifted to the east. The positive polarity of the NAM index is marked by anomalously low geopotential heights over the polar cap as used conventionally in many studies of the winter NAM (e.g., *Thompson and Wallace* [1998; 2000], *Fyfe et al.* [1999], *Shindell et al*. [1999; 2001], and *Miller et al*. [2006]).

In Figure 5.12, the differences of geopotential heights calculated from ModelE simulations at 765hPa between low NAM and high NAM are shown in the MAX and MIN. The low NAM mode is marked by anomalously high geopotential heights over the polar region and by anomalously low heights in the zonal belt centered near 45ºN. The signal of NAM in MIN (80m) is greater in northern Europe than in MAX (50m). As in the EOF pattern in Figure 5.7, the signal of NAM in ModelE simulation over Asian continent differ from that in NCEP/NCAR reanalysis at lower troposphere. In the solar maximum conditions, the pronounced NAM signal in geopotential heights is over the eastern coasts of Asia. In the solar minimum conditions, it is divided into two centers, one over the Aleutian Island region and the other over Siberia.

To compare this NAM signal in the ModelE with that in the observation, we have classified the NCEP/NCAR reanalysis geopotential heights at 850hPa into high and low NAM index cases as in the ModelE, and then further categorized for solar maximum and solar minimum using the monthly mean UV flux. The high/low solar activity months are sampled as those in which its UV flux is above/below one standard deviation from the mean of already selected high NAM or low NAM cases. The results for the differences in the geopotential heights between low NAM and high NAM composites are shown in

Figure 5.18 for solar maximum and solar minimum conditions. The geopotential heights over the Asian monsoon region are lower by more than 50 meters and they are higher by more than 50 meters in the Arctic regions in low NAM condition. The difference composites between the solar maximum and minimum conditions are qualitatively similar. However, consistent with the model, the composite geopotential height differences in reanalysis show that the two negative anomalies in Euro-Atlantic and Aleutian island regions are enhanced in the solar minimum conditions.

5.2.7 Conclusions

The leading EOFs of summer geopotential heights, or the Northern Annular Modes, obtained from GISS ModelE in the stratosphere and troposphere reproduce salient features of the corresponding patterns obtained from NCEP/NCAR reanalysis data. The model simulated pattern in the stratosphere is consistent with the interpretation that the low values of its principal component represent a regime of above-normal summer conditions, i.e., the distribution of the geopotential heights, zonal winds and temperatures have positive anomalies with respect to the mean summer state. Similarly, the high NAM regime conditions represent a less summer-like state. The northern annular mode in the troposphere is dominated by variability over the Asian monsoon region, but the monsoon pattern in the ModelE is weaker and shifted to the east in comparison with that obtained from NCEP/NCAR reanalysis. The ModelE simulations produced incoherent EOF patterns near the surface presumably due to problems with parameterization of boundary layer processes. Comparing model simulations in the solar maximum and in the solar

minimum conditions, we find that the summer stratosphere has positive anomalies with respect to the average summer conditions under maximum conditions, i.e., it is more summer-like than the average summer state, while it is less summer-like than the average state in solar minimum conditions. This response is similar to that in NCEP/NCAR reanalysis. Consistent with its interpretation, the NAM index values are lower in solar maximum conditions than in the minimum conditions. Furthermore, the variability in atmospheric conditions associated with the Northern Annular Mode is greater in solar minimum conditions than in maximum conditions in the model.

Salby and Callaghan [2006] distinguish between the "direct (linear)" effects of changing UV radiation on the stratosphere and "indirect (nonlinear)" effects. The "linear" effects are relatively weak, typically less than 0.5K, and induced by solar UV heating, by photochemically enhancing stratospheric ozone. The temperature response to the solar forcing, which is estimated from the difference in the average 7 hPa temperature between MAX and MIN simulations, is 0.6 K in the polar region and 0.3 K in midlatitudes except in the middle of the Asian continent. The changes of winds and temperature seem to be produced by the direct (linear) response [*Salby and Callaghan*, 2006] to the UV irradiance modulations.

The NAM in the lower troposphere contains only about 16 percent (in the NCEP/NCAR reanalysis) to 18 percent (in the model) of the variance in geopotential heights. This may be a reason why our comparison of composite differences between low NAM and high NAM for solar minimum and maximum conditions in the lower troposphere did not yield significant differences in the model simulation or in NCEP/NCAR reanalysis.

The comparisons presented in this chapter highlight two areas where improvements in ModelE can result in significantly more realistic simulations. One is the lack of coherence in the EOF patterns below 765 hPa, which may indicate an unrealistically high heterogeneity in boundary layer fluxes. The other is the weakness of the simulated Asian monsoon and its displacement to the east in comparison with observations. The largest geopotential height variability in the leading EOF in the lower troposphere is in the monsoon region, and its incorrect simulation therefore indicates possible distortions in the simulation of regional climate pattern in Asia. Similarity of the simulated northern annular modes in the middle and upper troposphere and in the stratosphere with the patterns found in NCEP/NCAR reanalysis, and their responses to changes in solar activity is an encouraging result. Given these basic agreements, further comparative analysis seems useful to identify important sun-climate mechanisms driving climatological changes. An important future work along these lines would be to investigate and to compare the responses of the ozone distribution to variations in Northern Annular Mode and in solar activity. Another topic to investigate is how complete the reaction scheme in the chemistry model should be in order to adequately simulate the ozone response necessary for a realistic thermal and dynamic response in the stratosphere.

.

6. The role of solar forcing in the tropical circulation

This chapter studies the response of the seasonal tropical circulation to solar forcing with the Goddard Institute for Space Studies (GISS) ModelE. To investigate characteristic solar signals in the tropical circulation, the model experiments are carried out with certain imposed conditions: a doubly amplified solar forcing, the present day and preindustrial greenhouse gases and aerosol conditions, with the mixed layer or fully coupled dynamic ocean model. From both the model and the NCEP reanalysis, the tropical humidity increases due to the solar forcing are found to be statistically significant in both seasons. Statistically significant changes are also found in the vertical velocities for both the Hadley and the Walker circulations over the Pacific region.

6.1 Introduction

The hypothesis by *van Loon and Labitzke* [1994], that vertical motion in the tropics is correlated with the decadal solar oscillation, has been supported by many observational evidences [e.g., *Gleisner and Thejll*, 2003; *Salby and Callaghan*, 2005; *Kodera*, 2004]. Some of the observational studies suggest that the thermal solar signal is preferentially strong in subtropical Pacific areas and affects the moisture transport and precipitation in these regions [*van Loon et al*., 2004, *van Loon et al*., 2007].

Paleoclimate records also show a link between solar insolation and the centennial scale migration of the Northern Hemisphere Inter-Tropical Convergence Zone

(ITCZ) during the last millennium. It is reported that the historically severe drought in Yucatan peninsula occurred during times of increased solar output [*Hodell*, 2001]. The result from sediment record of Lake Chichancanab directly reflects the southward shift of ITCZ which is over the northernmost region of the peninsula during summer. Conversely, the Ti content data from the Cariaco basin (~10ºN) ocean sediment [*Haug et al*., 2003] suggests wetter conditions with increased solar activity. The *G. bulloides* $\delta^{18}O$ record of Cariaco basin also shows the wetter and warmer conditions when sunspot numbers are high over the last three centuries [*Black et al.*, 2004]. As this location is further south, this record is consistent with the ITCZ shift inferred from the lake records. It is also reported that the Florida Strait was in drier conditions with anomalously high surface salinities during the little ice age [*Lund et al*., 2006]. The $\delta^{18}O$ values of stalagmite from southern Oman suggests that monsoon precipitation decreased gradually in response to declining Northern Hemisphere summer solar insolation during the middle to late Holocene [*Fleitmann et al*., 2003].

In addition to these observational and proxy studies, there are successful modeling works [*Meehl et al.*, 2003; *Meehl and Hu*, 2006; *Matthes et al.,* 2006; *Shindell et al*., 2006b] that further investigate the dynamic couplings and feedbacks of the tropical circulation due to solar forcing. *Meehl et al.* [2003] suggest a mechanism in which the enhanced solar forcing produces greater evaporation and moisture in the precipitation convergence zones, a more intensified regional monsoon, and strengthened Hadley and Walker circulations, that cause cloud reductions, and hence, leads to a configuration where more solar input resides over the subtropical ocean region. Thus, the sensitivity of the tropical circulation response can cause the solar forcing to be amplified in the cloud-

free subtropics through positive feedbacks. *Matthes et al.*[2006] show that the vertical velocity response is most significant over the Indian Ocean and western Pacific with Freie Universität Berlin Climate Middle Atmosphere Model (FUB-CMAM). *Shindell et al.* [2006b] also show that solar forcing induces increased precipitation in the tropical western Pacific region from a simulation with a dynamic ocean coupled ModelE version of the Goddard Institute for Space Studies (GISS) general circulation model (GCM).

In this chapter, using the same GISS chemistry-coupled GCM, experiments are designed to investigate the role of solar forcing on seasonal tropical circulation. A doubly amplified solar forcing and different anthropogenic forcings are imposed on models with different ocean modules. The amplified solar variability is used to enhance the signal to noise ratio. Comparison of simulations with different solar forcings can also permit us to observe the linearity of the climate response. Two different atmospheric compositions are imposed; one with the present day (PD) greenhouse gases and aerosol conditions, and the other with preindustrial (PI) conditions.

From each simulation, statistically significant solar signals in the tropospheric specific humidity are presented for January and July. We also show solar signals in the vertical velocity in each simulation over the Pacific region, where the zonally asymmetric response pattern plays an important role in the tropical circulation.

6.2 Model experiments

Four pairs of model experiments are carried out to investigate the role of solar forcing in the tropical circulation: one with the present day (PD) greenhouse gases and

aerosol conditions (PD-qflux), one with the preindustrial (PI) conditions (PI-qflux), one with doubled minimum solar forcing (DF-PD-qflux), and finally one with the preindustrial (PI) conditions and with the hybrid-isopycnic ocean model HYCOM (PI-HYCOM) (Table 5). For the preindustial cases, all anthropogenic emissions into the troposphere are removed, and long-lived greenhouse gases are set to the conditions at 1850. Biomass burning emissions were set to 10% of their PD values. The PI runs are targeted to estimate the most pronounced long-term recent solar minimum event, the Maunder Minimum, when the sun's output was reduced and only a few sun spots appeared. The q-flux ocean model is a simplified thermodynamic mixed-layer ocean model, where the SST is allowed to adjust to different atmospheric fluxes but the ocean heat transport is held constant. The oceanic heat convergence (the q-fluxes) into the isothermal mixed layer is calculated as a residual given by the heat and mass fluxes at the base of the atmosphere. HYCOM includes 16 isopycnal vertical layers with horizontal resolution of 2º x 2º cos(latitude), and produces a relatively reasonable magnitude of El Niño-Southern Oscillation (ENSO)-like variability [*Sun and Bleck*, 2006].

The model simulations are performed separately for two solar activity conditions: solar maximum and solar minimum. Each pair of simulations, except the double minimum run, is forced with irradiance changes that take place over the 11-year solar cycle for perpetual solar maximum (MAX) and perpetual solar minimum (MIN) conditions. The 11-year solar cycle irradiance change corresponds to ~0.19 W/m² instantaneous radiative forcing at the tropopause, equivalent to 1.1 W/m² in solar irradiance change at the top of the atmosphere. For the double minimum run, the amplitude of the solar cycle change is doubled to give a larger solar forcing. The

spectrally varying solar irradiance perturbation input to the 3-dimensional chemistry coupled atmospheric model produces stratospheric and tropospheric ozone changes [*Shindell et al.*, 2006a].

The responses of the model to solar forcing are presented as differences between MAX and MIN simulations. In a previous analysis using the identical model output, the index for the northern annular mode (NAM) in the stratosphere was found to stabilize after the first twenty years of simulation [*Lee et al*., 2007]. For this reason, the analysis presented in this paper is for the last 17 years from the 37 years of both MAX and MIN runs that are coupled to q-flux ocean module. For the PI-HYCOM simulation, the last 30 years from 60 years of run are analyzed.

6.3 Solar signal in specific humidity

6.3.1 Local specific humidity

Mid-tropospheric humidity is highest in the convective region between 20°S and 10°N in January, and is highest between 10°S and 20°N in July, as the convective region moves toward the respective summer hemisphere (Figure 6.1). The climatology of zonally averaged specific humidity is shown for the model (Figure 6.1(a) and 6.1(c)) and for the NCEP/NCAR reanalysis (Figure 6.1(b) and 6.1(d)). Mid-tropospheric humidity decreases sharply with latitude both in the model and in the NCEP/NCAR reanalysis. This latitudinal distribution of specific humidity does not result from the temperature variations, but from the descending branch of the Hadley cell [*Pierrehumbert,* 2001].

The air in the subsiding branch is dry, because it is brought down from a cold and dry place with conserved specific humidity. Although the subsidence region is dry compared to the ITCZ, it is still humid because of the latitudinal transport of moisture by turbulent eddies [*Pierrehumbert*, 2005]. Tropospheric humidity also decreases with altitude both in the model and in the reanalysis. However, the humidity in the model decreases more slowly with altitude, and shows more humidity in the troposphere compared to the reanalysis. A comparison of the AIRS (Atmospheric Infrared Sounding) and reanalysis specific humidity profiles with the 16 different modeling works presented by *John and Soden* [2007] shows that other models also simulate more column integrated humidity compared to observations.

In Figure 6.2(a) – 6.2(d) and 6.3(a) – 6.3(d), for January and July respectively, the responses of specific humidity to solar forcing are calculated as the differences of zonal mean composites of specific humidity between the MAX and MIN simulations. The corresponding differences obtained from the NCEP/NCAR reanalysis with all years and with non-ENSO years are shown in Figures 6.2(e) – 6.2(f) and 6.3(e) – 6.3(f) for January and July, respectively. For the reanalysis, the 11-year solar cycle is quantified by the 200-295 nm solar UV flux from *Lean* [2000]. For the period from 1948 to 2004, the months with monthly mean UV above/below one standard deviation from the mean are grouped as solar maximum/minimum; 10 months/12 months for July and 10 months/11 months for January. The extreme positive and negative ENSO years (1965, 1975, and 1997 for July; 1958, 1976, 1987, and 1989 for January) were filtered out from MAX or MIN years, for the non-ENSO composites. Both the model and the reanalysis consistently show that the specific humidity is greater in the convective region in solar

maximum compared to minimum for both seasons. The lowest level of the atmosphere is mostly moistened by solar forcing over oceanic regions.

In January, the humidity changes in PD-qflux and DF-PD-qflux (doubled minimum forcing) simulation (Figure 2(a) and 2(c)) show similar broad moistening of the tropics in the 30ºS – 20ºN, but the response is enhanced by the amplified forcing in DF-PD-qflux simulation. The responses from PI (Figure 2(b)) and PI-HYCOM (Figure 2(d)) simulations are consistent with the two significant response regions: one near the equator, and the other in the north of the strong convection region. In PI-HYCOM, the significant response is in lower troposphere as in reanalysis. The most significant humidity differences between solar maximum and solar minimum in the NCEP/NCAR reanalysis (Figure 2(e) and 2(f)) are shown at the lowest tropospheric level. The statistically significant solar signal is extended to 850 hPa near the equator by filtering out strong ENSO years. The solar signals in specific humidity show moistening in the tropics in the model as well as the reanalysis. In the model, however, the solar signals are statistically significant throughout the troposphere, including the Southern subtropics., while in the reanalysis the signal is limited to the lower troposphere and does not extend into the Southern Hemisphere subtropics. It has been already shown that upper-level humidity is highly correlated to the surface humidity in general circulation models, while the upper-level humidity quickly de-correlates in observations [*Sun and Held*, 1996]. The greater variability of the data in the reanalysis caused by other forcing factors, such as ENSO, volcanic eruptions, and anthropogenic sources of increase of humidity [*Gleisner and Thejll*, 2003] is partly responsible for the small areas of statistical significance in the reanalysis. Fewer degrees of freedom due to the short period of the

reanalysis in comparison with the model output can also cause this difference. By considering the auto-correlation of the each sample, the effective degrees of freedom is estimated as ~10 for N_{NCEP} and ~21 for N_{MODEL} by *Quenouille* 's procedure as described by *Angel and Korshover* [1981]. These effective numbers are applied to determine the significance with Student's *T*-test.

In July, the humidity changes in PD-qflux simulation (Figure 3(a)) show the broad moistening in the 30ºS – 30ºN. The solar signals in specific humidity in the DF-PD-qflux simulation (Figure 3(c)) are consistent with PD-qflux simulation, but the responses are enhanced by the amplified forcing. The latitude band of the significant positive signal is narrowed toward the equator under the preindustrial greenhouse gas and aerosol conditions in PI-qflux and PI-HYCOM simulations compared to PD-qflux and DF-PD-qflux cases. Such responses lead to the stronger humidity gradient in the north of the convective region during solar maximum. The humidity response in PI-HYCOM is amplified during July. In the reanalysis, significant solar signals are extended to the mid troposphere in July while they are confined within the low troposphere in January. The statistical significance of the solar signal is vertically extended to ~700hPa near the 10ºS by filtering out strong ENSO years.

The changes of humidity in both January and July corroborate the mechanism proposed in *van Loon et al*. [2004] and in *van Loon et al*. [2007]. During the solar maximum condition, the greater solar energy input to the tropical surface air is converted into higher SST through air-sea interaction [*White et al.*, 2003] and into greater specific humidity in the boundary layer. The increase of the humidity provides more liquid water content in clouds and makes the precipitation process more efficient in the ascending

regions of convective systems. However, efficient convective precipitation leaves less water vapor available for detrainment and reduces cirrus coverage, the precipitation, and the humidity in the northward part of the convective region [*Lindzen et al*., 2001]. This response of enhanced precipitation in the ascending branch and drying in the subtropics is also consistent with the response seen in *Shindell* et al. [2006b]. This is also consistent with the theoretical response to global warming in general as outlined in *Allan and Soden* [2007]. Similar to our result, *Gleisner and Thejll* [2003] also show the moistening of the tropical troposphere during solar maximum from analyzing the annual mean NCEP/NCAR reanalysis after filtering out ENSO and volcanic signals.

6.3.2 Column integrated specific humidity

The model simulated specific humidity, integrated over 500-970 hPa level, is high in the equatorial band with a substantial latitudinal gradient over the Pacific. The difference of the integrated specific humidity between MAX and MIN is shown for January and July in Figure 6.4(a)-6.4(d) and 6.5(a)-6.5(d), respectively. In the equatorial band, positive solar signals are found in the Atlantic sector in both seasons. In January, this positive signal in the PD-qflux run extends from the Amazon area to equatorial western Africa, and to the western coast of Australia. In the PI-qflux run, the positive signal extends to the eastern Pacific and Indian Ocean. The positive humidity signal in the DF-PD-qflux run is significant throughout the equatorial band including the Intonesian archipelago. In July, the positive solar signals in the PD-qflux run are more significant in the Atlantic sector, and extend toward Africa and India. The PI-qflux run

shows a positive center in the Indian Ocean and in the eastern Pacific. Similar to January, the positive signal in the DF-PD-qflux run is also significant throughout the equatorial band in July. The PI-HYCOM run suggests an intensified summer monsoon in Africa and India (Figure 5(d)). These agree with the work of *Meehl et al*., [2003] demonstrating that enhanced solar forcing induces more evaporation over the moisture divergent oceanic regions, and that the increased moisture converges into the precipitation zones, intensifying the regional African and Indian monsoons. These response patterns are consistent with the earlier analysis of *Shindell et al.* [2006b] indicating increased precipitation near the equator and decreases at subtropical to middle latitudes and an enhanced Asian monsoon in GISS-ModelE PI-HYCOM simulations. The record in a stalagmite from Qunf Cave (~17ºN) of southern Oman [*Fleitmann et al*., 2003] indicates the gradual long-term increase in Indian monsoon precipitation intensity in response to increase of June to August summer insolation. Lake sediment core records from Yucatan peninsula (~20ºN) suggest a contrasting solar-precipitation relationship indicating that the century-scale E/P (evaporation/precipitation) ratio was enhanced with high solar activity over the past 2600 years [*Hodell et al*., 2001].

The significant solar signals in the integrated tropospheric humidity (500-970 hPa) over the equator, especially in DF-PD-qflux run (Figure 4(c) and 5(c)), coincide with the peak solar signals in the annual mean tropospheric layer thickness (500-1000 hPa) shown in *Gleisner and Thejll* [2003] with the NCEP/NCAR reanalysis. Geopotential thickness is defined as the height difference between two isobaric surfaces; it is linearly related to the mean temperature and the integrated humidity of the layer [*Zhang et al*., 2001].

6.3.3 Estimated radiative effect

The longwave radiative net flux difference due to the humidity change induced by the 11-year solar cycle is estimated by applying vertical profiles of zonally averaged specific humidity over 30 ºN latitude bands from the NCEP/NCAR reanalysis for both the solar maximum and the solar minimum to the NCAR Community Climate Model (CCM2) clear sky radiation parameterization scheme [*Hack et al*. 1993, NCAR Technical Note 382]. Other parameters are fixed from the climatology. The United Kingdom Universities Global Atmospheric Modeling Program (UGAMP) ozone profile [*Li and Shine*, 1995] is used for the ozone climatology. The longwave net flux at 30ºN calculated from solar maximum is ~0.2W/ m² greater than that from solar minimum at tropopause. The maximum 2% integrated water vapor change in the NCEP reanalysis due to solar forcing is roughly equivalent to 10% of the estimated increase of the global mean column integrated water vapor caused by the doubling of CO_2 [*Held and Soden*, 2006].

6.4 Solar signal in tropical circulation

Meehl et al. [2003] suggested a feedback mechanism for solar forcing: enhanced irradiance produces greater evaporation intensifying the regional monsoon, the Hadley and the Walker circulations in the tropics, leading to cloud reductions and hence more solar input over the subtropical ocean regions. *van Loon et al*. [2004], *Kodera* [2005], *van Loon et al*. [2007] showed significant differences in the seasonal vertical velocity (ω)

over the tropics between solar maximum and minimum that appear to be at least qualitatively consistent with this mechanism.

The tropical circulation responds to solar forcing by redistributing the zonally asymmetric diabetic heating. To further investigate the changes of the tropical Hadley and Walker circulations due to solar forcing, we show the differences in the zonally or meridionally averaged vertical motion (ω) between the MAX and MIN model outputs within the tropical Pacific region (Figure 6.6- Figure 6.9). The solar signals in the tropical circulations are compared to those seen by *van Loon et al*. [2004] and *van Loon et al.* [2007] using NCEP/NCAR reanalysis.

6.4.1 Solar signal in tropical circulation in January

The model climatology of the zonally averaged vertical velocity omega (ω) in pressure coordinates during the month of January (Figure 6.6(a)) shows the typical winter season features of vertical motion; i.e., rising motion over the tropics from 20ºS to 10ºN which peaks at 850 hPa and strong sinking motion around 30ºN which peaks at 500hPa. The statistically significant differences of vertical velocity between MAX and MIN in PD-qflux simulation (Figure 6(b)) suggest that the ascending motion in the Hadley cell is enhanced north and south of the equator throughout the troposphere except near the equator in the solar MAX run. The DF-PD-qflux simulation (Figure 6(d)) shows similar solar signal with the PD-qflux simulation, but more weakening of the descending branch. The changes in the vertical motion are not significantly increased by doubling the solar forcing. These signals in PD-qflux and DF-PD-qflux simulations indicate that the

ascending motion is enhanced and the ITCZ is shifted northward with solar forcing, and agrees well with the observed vertical velocity and precipitation changes shown by *van Loon et al.* [2007]. The vertical velocity responses of the PI-qflux and PI-HYCOM simulations (Figure 6(c) and 6(e)) represent weak enhancement in the ascending motion near the equator and weakening of the descending motion in the northward branch. In general, the model simulations indicate that the ascending branch of the Hadley cell over the Pacific is enhanced by solar forcing in January while the descending branch of the Hadley cell is weakened by solar forcing in that region.

The meridionally averaged vertical velocity in January over the equatorial band (from 10ºS to 5ºN) shows the Walker circulation along the equator in the Pacific; characterized by the rising motion west of 150ºW and sinking motion to the east (Figure 7(a)). The solar signal in the Walker circulation is shown in Figure 7(b)-7(e) from the model experiments through the differences of the meridionaly averaged vertical velocity (ω) within the equatorial region between MAX and MIN. Over the region of the Pacific warm pool (150ºE – 180º), the vertical upward motion is enhanced in the MAX compared to the MIN in the PD-qflux, DF-PD-qflux, and PI-qflux simulations (Figure 7(b)-7(c)). The enhancement of the vertically ascending motion over the Pacific warm pool indicates the strengthening of the Walker circulation, and is consistent with the increased specific humidity over this region as shown in Figure 4(a)-4(c). This result is also consistent with the enhancement of ascending motion near the equator as shown in Figure 6(b) - 6(d). The previous composition-climate modeling work of *Shindell et al*. [2006] that includes a coupled dynamic ocean also showed the increase of the annual mean precipitation in the Pacific warm pool region due to increased solar forcing. The vertical velocity change

between solar maximum and solar minimum is insignificant in NCEP/NCAR reanalysis (not shown).

6.4.2 Solar signal in tropical circulation in July

The differences of the zonally averaged vertical velocity in PD-qflux simulation in July (Figure 8(b)) show weakening of the southern flank of the ascending branch between 5ºS and 10ºS in MAX which coincides with that of the observational result of *van Loon et al* [2004]. The DF-PD-qflux simulation (Figure 8(d)) shows the similar solar signal with the PD-qflux simulation, but with the weakening of the northward part of the descending branch. Similar to the DF-PD-qflux simulation, the vertical velocity responses of the PI-qflux simulation (Figure 8(c)) represent weak enhancement in the ascending motion near the equator and substantial weakening of the descending branch. The responses in the PI-HYCOM simulation show weakening and a southward shift of the Hadley cell in the ascending branches. The intensified upwelling near the equator and the weakening of the upwelling in the northern part of the ascending branch in PI-qflux and PI-HYCOM simulations indicate a southward shift of the summer ITCZ. The Hadley circulation response patterns from the PI-qflux and PI-HYCOM runs with preindustrial compositions are consistent with the paleoclimate proxy records of *Hodell et al*.[2001] and *Haug et al*. [2003].

The model responses in Walker Circulation in July are illustrated in Figure 9(b) – 9(e) by showing the differences in the vertical velocity between the MAX and MIN, from 150ºE eastward to 90ºW. In the PD-qflux simulation (Figure 9(b)), there are stronger

ascending regions in the equatorial western and the central Pacific but weaker ascending regions in the eastern Pacific in solar maximum. In all the simulations, the enhanced Walker Cell with increased upward vertical motion in the western Pacific warm pool region is similar to that shown by *van Loon et al*. [2004] in the July-August averaged NCEP/NCAR vertical velocity. In PI-qflux simulation (Figure 9(c)), the upward motion in the eastern part of the Walker Cell is significantly enhanced. The stronger upward motion (anomalous negative values) in this region during solar maximum is consistent with the increase of the integrated humidity (positive values) in Figure 5(b). Over all, the ascending branch of the Walker circulation shows strong uprising in response to solar forcing in the western Pacific as is in January.

6. 5 Conclusion

The response patterns of tropical humidity and vertical motion to solar forcing are season dependent and spatially heterogeneous. In the tropics, both the model and the reanalysis consistently show that the specific humidity is significantly greater in the convective region in solar maximum compared to solar minimum for January and July. The humidity response in DF-PD-qflux simulation is enhanced by the doubled minimum forcing. The humidity responses indicate that tropical climate changes associated with the solar cycle include increased water vapor during solar maximum, which is similar to the responses expected from greenhouse gas increases [*Cess*, 1993]. The column integrated humidity in the model simulations increased with solar forcing in the tropical band over the Atlantic sector in both seasons, with different composition, different solar

forcing, and different ocean model. Moreover, this positive signal extends from the Amazon area past equatorial western Africa, to the western Pacific from Indonesia to the west coast of Australia. This signal extends to the whole Pacific Basin in DF-PD-qflux run when the magnitude of the solar forcing is doubled.

In the present day conditions, the tropical circulation response to solar forcing is generally consistent with the observations [*van Loon et al*., 2004, *van Loon et al*., 2007] both in winter and summer. The responses of the zonally averaged vertical velocities in PD-qflux and DF-PD-qflux simulations indicate that the ascending branch of the Hadley cell is enhanced near the equator and the ITCZ is shifted northward in response to solar forcing during the winter. The changes in the vertical motion are not significantly increased by doubling the solar forcing. In the summer, the intensified upwelling near the equator and the weakening of the upwelling in the northern part of the ascending branch in PI-qflux and PI-HYCOM simulations indicates a southward shift of the summer ITCZ. The response of seasonal tropical circulation to solar flux changes results in modulation of the strength and the position of the ascending and descending branches of Hadley circulation. which are related to regional monsoons, When the preindustrial conditions are imposed, the Hadley circulation response patterns from the model agree with proxy records which show correlations between regional drought caused by the shift of the seasonal ITCZ and solar variability.

The enhancement of the meridionaly averaged vertical velocity over the western Pacific indicates strengthening of the Walker circulation in response to solar forcing in both seasons. However, regions of statistical significance of the solar signal in vertical velocities are not consistent among the models with different atmospheric

composition, solar forcing, and ocean modules.. This includes the possibility that the tropical circulation response to solar changes depends strongly on the greenhouse effect condition, amplitude of solar forcing, and atmosphere-ocean interaction. Hence further work is clearly required to establish if the model's sensitivity to solar forcing is realistic and to better characterize the causes of the apparent dependence of the response to the background composition, the oceanic response, and the amplitude of the solar forcing.

7. Future Challenges: solar signals in mid-latitudes

Solar signals in the tropics have been investigated in the previous chapter. The differential heating in the tropical troposphere due to different solar irradiance induces anomalous increase in humidity, and changes in Hadley circulation. The response of the seasonal tropical circulation to the solar perturbation results in modulation of the characteristic features of the regional monsoon, which is coupled to the strength and the position of the ascending and descending branches of the Hadley circulation. One of the important characteristics of the tropical and subtropical circulation anomalies is that they act as the planetary wave source for midlatitude dynamics [*Chang,* 1995; *Chang,* 1998; *Seager*, 2006]. The results of these quasi-geostrophic models show that the changes of tropical circulation can create either a latitude shift or a change in the strength of the eddy driven zonal and meridional residual circulation in midlatitudes.

At midlatitudes, the responses of the tropospheric circulations to solar forcing are complex, because there is a non-linear dynamic interaction between the zonal mean flow and the baroclinic eddies. Baroclinic eddies can potentially be changed due to solar forcing, owing to the effect of changes in meridional temperature gradients, in humidity, and in land-sea temperature contrast. The heating anomalies located on different sides of a jet will have different effects, either through the forcing of transient waves or through an alteration of the mean flow by means of instability or wave-mean flow interaction [*Shukla and Kinter III*, 2006]. The effect of the solar forcing is also strongly influenced by dynamics at midlatitudes, especially by the propagation of planetary waves which redistribute the solar energy.

In an earlier work, *Geller*[1988] has hypothesized a radiative-dynamic sun-climate mechanism in which the radiative changes alter planetary-wave propagation through the meridional temperature gradient and polar vortex changes, based on the numerical modeling of the quasi-geostrophic stationary wave [*Geller and Alpert*, 1980]. He has also suggested that the changes in the planetary-wave will further induce the polar vortex to change as a result of the positive feedback which can amplify the direct radiative solar influences. As suggested by *Salby and Callaghan* [2006], the direct response to the variation of UV irradiance is relatively weak. They distinguish between the "direct (linear)" effects of changing UV radiation on the stratosphere and "indirect (nonlinear)" effects. This contrasts with wintertime "non-linear" effects that include planetary wave interactions with tropical winds that are affected by the direct solar effect and by solar modulation in the QBO frequency band.

By analyzing the zonally asymmetric northern winter temperature response for all altitudes up to the upper mesosphere obtained from simulation of the GCM HAMMONIA (Hamburg Model of the Neutral and Ionized Atmosphere), *Schmidt and Brasseur* [2006] suggested that standing planetary waves can be modified by solar forcing.

The purpose of this chapter is to propose a physical mechanism whereby the large scale mid-latitude dynamic response in the troposphere may occur by dynamic coupling. The response of the tropospheric zonal wind in winter (January) and its relation to the temperature gradient and planetary wave forcing (EP flux) is discussed with the PD GISS GCM ModelE experiment.

7.1 Direct and indirect effects of solar forcing

The first impact of solar variability *is* to reduce radiative forcing because of absorption by the existence of molecular oxygen and ozone in the stratosphere which reduces the solar radiation reaching the tropopause by about 5% [*Gray et al.,* 2005]. Secondly, however, heating of the stratosphere by enhanced solar UV produces additional downward LW (Long Wave) radiation at the tropopause, thus enhancing radiative forcing. Changes in ozone also impact the radiation fields – additional ozone reduces the downward SW (Short Wave) fluxes but increases the LW fluxes. The changes in UV lead to changes in stratospheric ozone production and hence, through the associated changes in stratospheric heating. The GCM used in this study has a fully-coupled chemistry-radiation scheme so feedbacks between ozone changes, temperatures changes and circulation changes are calculated.

Direct effect of solar forcing is generally referred to as the thermal modulation of climate including dynamics i.e. radiation's influence on thermal wind diagnostic relationship via UV variability. The temperature response simulated by GCM shows a stratospheric maximum of about 0.5 – 1K close to the stratospause. The temperature increase is due to both the direct effect of stronger solar irradiance at solar max and the increased availability of ozone which is the main absorber at these altitudes. Different analyses of satellite [*Hood*, 2004] and reanalysis [*Hood,* 2004; *Crooks and Gray*, 2005] show temperature response maxima of 0.5 to 2K in the equatorial upper stratosphere and a secondary maximum of smaller magnitude close to the equatorial tropopause. In earlier modeling studies on the solar cycle [e.g., *Haigh*, 1994; *Shindell et al.*, 1999, *Matthes et*

al., 2004], magnitude and height of the maximum ozone and temperature responses are comparable to present results. However, the pattern and longitudinal distribution of the ozone response can differ significantly between models. *Rind* [2002] notes that the 11-year solar cycle temperature anomaly in the equatorial upper stratosphere gives rise to an anomalous horizontal temperature gradient and to a corresponding anomaly in the vertical wind shear in the region of the polar night jet at upper levels.

Kodera and co-workers [2002; 2003; 2004] show solar-induced zonal wind anomaly with the associated E-P flux changes illustrating the change in planetary wave propagation. The zonal wind anomaly moves poleward and downward throughout the winter months. This anomaly suggests that solar variability influences the structure of the polar night jet and hence the propagation of planetary-scale waves that travel upward from the troposphere. This then further affects the polar vortex and can produce sudden stratospheric warming. As noted by *Rind*. [2002], an anomalous horizontal temperature gradient leads to an anomaly in vertical wind shear in the region of the polar night jet at upper levels. As a result of the consequent anomalous planetary wave propagation, this zonal wind anomaly will gradually descend with time into the lower stratosphere to give rise to solar effects that are much larger than the direct solar UV influences that initiate this dynamic modulation. *Haigh and Blackburn*[2006] showed a different banded zonal wind response with different temperature perturbations on the stratosphere. Dynamic response processes including planetary wave interactions with temperature and wind are called “in-direct” effects [*Salby and Callaghan*, 2006].

7.2 Solar signal in zonal mean wind U

During the winter season, the zonal westerly wind distributions can be divided into two regimes. One has the maximum strength in the upper troposphere in the 30ºN - 35ºN near 300-200 hPa (mid-latitude jet stream) and the other is the broad and strong westerly jet stream (Polar night jet) located in the winter mesosphere-stratosphere poleward of the mid-latitude jet stream. The strength and the location of these two jets are well simulated in the GISS ModelE (not shown).

The response of the zonal mean zonal wind to solar forcing is shown as the difference in the zonal wind between MAX and MIN in Figure 7.1. The significant positive difference in zonal mean westerly is shown in mid troposphere of midlatitudes. The acceleration of the zonal wind is limited to the poleward flank of the mid latitude jet and does not penetrate equatorward of the jet core. The combined response leads to the poleward shift of the jet during solar maximum. This response is qualitatively similar to those suggested in the previous modeling works of *Haigh and Blackburn* [2006] and *Shindell et al.* [2001].

Haigh and Blackburn [2006] have used an idealized AGCM to explore the zonal mean wind response to the two different lower stratospheric temperature perturbations. One experiment prescribes a uniform heating perturbation, and the other a heating perturbation that is maximum at the Equator and tapers to zero at the poles. They found that imposing a latitudinal gradient of the stratospheric heating gave rise to a tropospheric response that had a banded structure in the troposphere, with strengthened zonal winds near 40ºN to 60ºthat are flanked by weaker winds near 25ºN and northward of 60ºN (their

figure 3(c) and 3(d)). *Shindell et al.* [2001] also showed that the acceleration of the zonal wind at high latitudes and the increase of surface AO index are induced by increased solar irradiance perturbation.

7.3 Solar signal in Temperature gradient

The differential solar heating between equator and pole sets up the anomalous temperature imbalances which induce atmospheric motions to modify the temperature gradient. Thus the meridional temperature gradient is one of the fundamental measures for the solar modulation of mid-latitude dynamics.

The temperature difference between MAX and MIN in Figure 7.2 shows a strong negative anomaly center at 60°N in the low troposphere during solar maximum. This results in an enhanced negative temperature gradient between 40°N and 60°N and a weakened negative temperature gradient poleward of 60°N. The increase of the latitudinal temperature gradient between 40°N and 60°N leads to the enhanced upper tropospheric westerly jet in this region, and the enhanced jet refracts the upward propagating planetary waves equatorward.

Increased westerlies in MAX are balanced by the anomalous mean meridional circulation, which yields the anomalous equatorward wind in the upper troposphere by the Coriolis force, and the anomalous poleward (equatorward) winds poleward (equatorward) of about 40º near the surface by the surface friction (Figure 7.4). The increase in the negative temperature gradient provides more eddy potential energy which induces positive meridional component of eddy momentum flux (v') by baroclinic

conversion. Thus, the enhanced meridional circulation in north of the jet core leads to ascending motions in high latitudes throughout the troposphere (Figure 7.5) [*Shindell et al*., 2001]. The ascent causes adiabatic cooling and creates noticeable negative temperature (Figure 7.2) and enhanced temperature gradient in this region, so that the process iterates to support the poleward shift of the jet.

7.4 Solar signals in Eliassen-Palm flux

The zonally averaged Eliassen-Palm (E-P) flux is shown with the zonal mean zonal wind in Figure 7.6 (a). The E-P flux is upward in midlatitude lower troposphere closer to the sharp zonal wind gradient. These fluxes turn equatorward in the upper-troposphere subtropics toward lower latitudes.

The Eliassen-Palm flux (E-P flux), ***F***, is a vector in the meridional (y,z) plane with the y component equal to the eddy momentum flux and the z component to the eddy heat flux.

$$[F] = \overline{\rho}\begin{bmatrix} -[u'v'] \\ f_0[v'\theta']/\dfrac{d\Theta_0}{dz} \end{bmatrix} \text{,----------(3)}$$

where θ is the potential temperature, and Θ the global mean average of θ.

Each component itself is a useful quantity as an indicator of wave propagation, and the combination of eddy fluxes on the meridional plane represent the direction of wave propagation. The E-P flux divergence acts as a forcing on the zonal mean flow. It also acts as a source term for the stream function, and indicates important aspects of circulation in the meridional plane.

An illuminating relation derived by *Andrews and McIntyre* [1976, 1978] is given by,

$$\frac{\partial A}{\partial t} + \nabla \cdot F = D, \quad \text{----------(4)}$$

where D is zero for conservative motion (no dissipation or generation of waves by diabatic or frictional effects), and A is a measure of local wave activity or the density of "EP wave activity". In the beta-plane, quasi-geostrophic case an approximate expression for it is,

$$A \approx 1/2\overline{q'^2} / \overline{q_y}, \quad \text{----------(5)}$$

where the subscript denotes differentiation, and q' is the quasi-geostrophic eddy potential vorticity defined as,

$$q' = v_x' - u_x' = f(\theta'/\overline{\theta}_p)_p. \quad \text{----------(6)}$$

When D=0, equation (4) denotes a conservation equation where the increase (decrease) in time of wave activity is induced by inward (outward) flux of *F*. This shows the role of the EP flux vector *F* as a measure of the flow of wave activity.

Hence, the E-P flux is a useful diagnostic tool of wave propagation and wave-mean flow interaction [*Edmon et al.,* 1980; *Palmer*, 1981; *Geller et al*., 1983], from which one could estimate the forcing for meridional, vertical, and zonal circulation. The difference of eddy forcing between MAX and MIN is shown with the difference of zonal wind in Figure 7.6(b). The solar signal in the northward eddy momentum flux peaks in the mid troposphere and coincides with the zonal wind anomalies. The jet displacement is primarily maintained by changes in the poleward eddy momentum flux , as mentioned in *Haigh and Blackburn* [2006]. Increase in meridional temperature gradient also leads to an increase in the baroclinicity of the atmosphere. As shown in

Figure 7.6(b), the resulting anomalous eddy propagates toward the tropics and dissipates there close to its critical latitude. This also results in an increased acceleration of the jet towards the north, and a deceleration of the jet towards the south [*Chang*, 1998]. Both of these changes in temperature gradient and in momentum flux act to shift the upper level zonal wind poleward.

8. Conclusion

This study is based on statistical analysis of the GISS GCM ModelE simulations and the NCEP/NCAR reanalysis. The 11-year solar signals are shown in NAM, in tropical circulations, and in the mid-latitudes circulations. The transmission mechanism of the solar signal from the stratosphere to the troposphere through NAM is suggested, and used to improve previous understanding. First, the summer NAM index is newly defined by EOF (Empirical Orthogonal Function) analysis and its dynamical interpretation is presented. Statistical tests were carried out with observational data to diagnose the solar signal. Then, the effect of solar UV variability on the summer NAM is investigated in GISS ModelE version of GCM. To identify characteristic solar signals in the tropical circulation, a new model experiment was carried out with a doubly amplified solar forcing. The direct effect of solar forcing is studied with summer stratospheric temperature and tropical humidity. The indirect effect of solar variability is shown with planetary wave changes in mid-latitudes. The main results from each section are summarized here.

1. The downward propagation rate of the Northern Annular Mode (NAM) is investigated in different solar and QBO conditions and the propagation rate is found to be higher when the solar activity is stronger. This difference is more striking when the zonal wind direction in the tropics is from the west.

2. The summer NAM index is newly defined with reanalysis data to describe the characteristics of large scale variability and its relation to 11-year solar cycle. The

summer NAM in the troposphere is characterized by variability over the Asian monsoon region. The summer NAM in the stratosphere and upper troposphere is correlated with the solar ultra violet (UV) flux such that in solar maximum conditions the stratospheric circulation is more 'summer-like' than average, and less 'summer-like' in solar minimum conditions.

3. The summer NAM index in GISS GCM is analyzed and compared to that calculated with the reanalysis data. A quantitative comparison of the anti-correlation between the NAM and the solar forcing is presented in the model and in the observations, both of which show lower/higher NAM index in solar maximum/minimum conditions. The direct temperature response to solar forcing, which is estimated from the difference in the average 7 hPa summer temperature between MAX and MIN simulation, is ~0.6 K in the polar region and ~0.3 K in midlatitudes except in the middle of the Asian continent.

4. In this work, a new GCM model experiment is designed with doubled minimum solar forcing. In an effort to avoid the uncertainties from ocean-atmosphere interaction and the complexity from greenhouse gas change, each underlying process is separated since their signatures overlap and interact with each other. Four model experiments are analyzed to investigate the role of solar forcing in the tropical circulation: one with the present day (PD) greenhouse gases and aerosol conditions, one with the preindustrial (PI) conditions, one with the doubled minimum solar forcing, and finally one with the hybrid-isopycnic ocean model (HYCOM). The specific humidity is significantly greater in the convective region in solar maximum conditions than in solar

minimum conditions for both seasons. Specific humidity response is related to the amplitude of solar forcing. Influence of Total Solar Irradiance (TSI) on evaporation, can be suggested as the direct effect of solar heating.

The column integrated humidity in all the model experiments with different composition, different solar forcing, and different ocean modules, increased with solar forcing in the tropical band over the Atlantic sector for both seasons. The model's humidity response pattern is consistent with paleoclimate records indicating increased precipitation near the equator that decreases at subtropical to middle latitudes with increased solar output. The differences in the zonally averaged vertical velocities indicate that the ascending branch of the Hadley cell is enhanced and shifted northward, and that the descending branch is weakened and shifted northward with solar forcing in January. The downward branch of the Hadley cell is strengthened with solar forcing in July.

5. From the model results, the solar signals in meridional temperature gradient and zonal mean wind are shown. The enhanced meridional temperature gradient leads to a strengthening of the northern part of jet. Interaction with planetary waves is suggested as a possible mechanism responsible for northward shift of the zonal mean wind with solar forcing. Like many other observational and modeling works, this study also concentrates on showing the most significant solar signals appearing in the stratosphere, in high latitudes, and in the tropics. However, the change of mid-latitude circulation by indirect (non-linear) solar modulation of planetary waves, and its link to the changes in the tropics and in high latitudes remain uncertain.

6. The GISS model reasonably well simulates the atmospheric circulation. However, the parameterization of QBO and SAO are important for more realistic presentation of the solar signal. An improvement of the gravity wave parameterization will also provide more significant results in stratospheric residual circulation.

References

Allan, R.P. and B. J. Soden (2007), Large discrepancy between observed and simulated precipitation trends in the ascending and descending branches of the tropical circulation. *Geophy. Res. Lett*., **34**, L18705, doi:10.1029/2007GL031173.

Angell, J. K. and J. Korshover (1981), Comparison between sea surface temperature in the equatorial eastern Pacific and United States surface temperature. *Jour. App. Meteor*., **20**, 1105-1110.

Angell, J. K. (1988), Variations and trends in tropospheric and stratospheric global temperatures, 1958-87. *J. Clim*., **1,** 1296-1313.

Angell, J. K. (1989), On the relation between atmospheric ozone and sunspot number, *J. Clim*., **2**, 1404-1416, 1989.

Angell, J. K. (1991), Stratospheric temperature change as a function of height and sunspot number during 1972-89 based on rocketsonde radiosonde data, *J. clim*., **4**, 1170-1180.

Baldwin, M. P., and T. J. Dunkerton, (1999), Downward propagation of the Arctic oscillation from the stratosphere to the troposphere. *J. Geophys. Res*., **104** (D24), 30,937- 30,946.

Baldwin, M. P., and T. J. Dunkerton (2001), Stratospheric harbingers of anomalous weather regimes. *Science*, **294**, 581-584.

Baldwin, M. P., and T. J. Dunkerton (2005), The solar cycle and stratosphere-troposphere dynamical coupling. *J. Atmos. and Solar-Terrestrial Phys*., **67**, 71-82.

Black, D. E., R. C. Thunell, L. C. Peterson, A. Kaplan, and E. J. Tappa (2004), A 2000-year record of tropical North Atlantic hydrographic variability, *Paleoceanography*, **19**, PA2022, doi:10.1029/2003PA00982.

Brasseur, G., and P. C. Simon (1981), Stratospheric chemical and thermal response to long-term variability in the solar UV irradiance, *J. Geophys. Res*., **86**, 7343-7362.

Brasseur, G., A. De Rudder, G. M. Keating, and M. C. Pitts (1987), Response of the middle atmosphere to short-term solar ultraviolet variations, 2, Theory, *J. of Geophys. Res.*, **92**, 903-914.

Burroughs, W.J., (1992), *Weather Cycles, Real or Imaginary ?,* 203 pp., Cambridge University Press.

Callis, I. B., and J. E. Nealy (1978), Solar UV variability and its effect on stratospheric thermal structure and trace constituents, *Geophys. Res. Lett*., **5**, 249-252.

Cess, R. D., M. H. Zhang, and G. L. Potter, H. W. Barker, R. A. Colman, D. A. Dazlich, A. D. Del Genio, M. Esch, J. R. Fraser, V. Galin, W. L. Gates, J. J. Hack, W. J. Ingram, J. T. Kiehl, A. A. Lacis, H. Le Treut, Z. X. Li, X. Z. Liang, J. F. Mahfouf, B.J. McAvaney, V. P. Meleshko, J. J. Morcrette, D. A. Randall, E. Roeckner, J. F. Royer, A. P. Sokolov, P. V. Sporyshev, K. E. Taylor, W. C. Wang, R. T. Wetherald (1993), Uncertainties in carbon dioxide radiative forcing in atmospheric general circulation models. *Science*, **262**, 1252-1255.

Chang, E. K. M. (1995), The influence of Hadley circulation intensity changes on extratropical climate. *J. Atmos. Sci*., **52**, 2006-2024.

Chang, E. K. M. (1998), Poleward-Propagating Angular Momentum Perturbations Induced by Zonally Symmetric Heat Sources in the Tropics, *J. Atmos. Sci*., **55,** 2229-2246.

Charney J. G., and P.G. Drazin (1961), Propagation of Planetary-Scale Disturbances from the Lower into the Upper Atmosphere. *J. Geophys.Res.,* **66,** 83-109.

Christoforou, P., and S. Hameed (1997), Solar cycle and the Pacific Centers of Action, *Geophys. Res. Lett*., **24**, 293-296.

Crutzen, P. J., I. S. A. Isaksen, and G. C. Reid (1975) Solar proton events: Stratospehric sources of nitric oxide, *Science*, **189,** 457-458.

Eddy, J. A. (1976), Maunder Minimum, *Science*, **192**, 1189.

Edmon, H. J. Jr., B. J. Hoskins, and M. E. McIntyre (1980), Eliassen-Palm cross sections for the troposphere. *J. Atmos. Sci.*, **37**, 2600-2616.

Fleitmann, D., S. J. Burns, M. Mudelsee, U. Neff, J. Kramers, A. Mangini, and A. Matter (2003), Holocene Forcing of the Indian Monsoon Recorded in a Stalagmite from Southern Oman, *Science*, **300**, 1737-1739.

Fröhlich, C. (2006), Solar Irradiance Variability Since 1978: Revision of the {PMOD} Composite During Solar Cycle 21, *Space Science Rev.*, **23**, 17-24, doi: 10.1007/978-0-387-48341-2.

Fyfe, J. C., G. J. Boer, and G. M. Flato (1999), The arctic and Antarctic oscillations and their projected changes under global warming. *Geophys. Res. Lett.*, **26**, 1601-1604.

Foukal, P., G. North, and T. Wigley (2004), A Stellar View on Solar Variations and Climate. *Science*, **306**, 68-69.

Geller, M. A., and Alpert, J. V. (1980), Planetary wave coupling between the troposphere and middle atmosphere as a possible sun-weather mechanism, *J. Atmos. Sci.* **37**, 1197–1215.

Geller, M. A. (1988), Solar cycles and the atmosphere, *Nature,* **332**, 584–585.

Geller, M. (2006), Discussion of the solar UV/planetary wave mechanism. *Space Science Reviews*, **125,** 237-246.

Gillett, N.P., M.R. Allen, R.E. McDonald, C.A. Senior, D.T. Shindell, and G.A. Schmidt (2002), How linear is the Arctic Oscillation response to greenhouse gases? *J. Geophys. Res.*, **107**, no. D3, doi:10.1029/2001JD000589.

Gleisner, H. and P. Thejll (2003), Patterns of tropospheric response to solar variability, *Geophy. Res. Lett*., **30**, 1711-1714.

Gray, L. J., S. J. Phipps, T. J. Dunkerton, M. P. Baldwin, E. F. Drysdale, and M.R. Allen (2001), A data study of the influence of the equatorial upper stratosphere on northern hemisphere stratospheric sudden warming. *Quart. J. Roy. Met. Soc*., **127**, 1985-2003.

Gray, L. J., S. A. Crooks, C. Pascoe, and S. Sparrow (2004), Solar and QBO influences on the timing of stratospheric sudden warmings. *J. Atmos. Sci*., **61**, 2777-2796.

Greatbatch, R. J. and P.-P. Rong (2006), Discrepancies between different northern hemisphere summer atmospheric data products, *J. of Clim*., **19**, 1261-1273.

Haigh, J. D. (1994), The role of stratospheric ozone in modulating the solar radiative forcing of climate, *Nature*, **370**, 544-546, 1994.

Haigh, J. D. (1999), A GCM study of climate change in response to the 11-year solar cycle. *Quart. J. Roy. Meteorol. Soc*., **125**, 871-892.

Haigh, J. D. (2001), Climate variability and the influence of the sun. *Science*, **294**, 2109-2111.

Haigh, J. D., J. Austin, N. Butchart, M-L Chanin, S. Crooks, L. J. Gray, T. Halenka, J. Hampson, L. L. Hood, I. S. A. Isaksen, P. Keckhut, K. Labitzke, U. Langematz, K. Matthes, M. Palmer, B. Rognerud, K. Tourpali and C. Zerefos (2004), Solar variability and climate: selected results from the SOLICE project. *SPARC Newsletter No. **23***.

Haigh, J. D. (2006), The impact of Solar Variability on Climate. *Science*, **272**, 981-984.

Haigh, J. D., and M. Blackburn (2006), Solar influences on dynamical coupling between the stratosphere and troposphere, *Space Science Reviews*, **125**, 331-344.

Hameed S., and Jae. N. Lee (2005), A mechanism for sun climate connection, *Geophys. Res. Lett.,* **32** (L23817).

Hack, J. J., B. A. Boville, B. P. Briegleb, J. T. Kiehl, P. J. Rasch, and D. L. Williamson (1993), Description of the NCAR Community Climate Model (CCM2). NCAR Tech. Note NCAR/TN-3821STR.

Harder, J., E. Richard, J. Fontenla, P. Pilewskie , and G. Kopp (2008), Spectral Decomposition of the TSI record Using the SORCE TIM and SIM Instruments, Proceedings of 2008 SORCE meeting.

Haug, G. H., D. Gunther, L. C. Peterson, D. M. Sigman, K. A. Hughen, and B. Aeschlimann (2003), Climate and the collapse of Maya civilization, *Science*, **299**, 1731–1735.

Held, I. M. and B. J. Soden (2006), Robust Responses of the Hydrological Cycle to Global Warming, *J. Climate,* **19**, 5686-5699.

Hodell, D. A., M. Brenner, J. H. Curtis, and T. Guilderson (2001), Solar forcing of drought frequency in the Maya lowlands, *Science*, **292**, 1367–1370.

Hood, L. L. (1997), The solar cycle variation of total ozone: dynamical forcing in the lower stratosphere. *J. Geophys. Res.,* **102**, 1355-1370.

Hood, L. L. (2004), Effects of solar UV variability on the stratosphere. *Geophysical Monograph,* **141**, 283-303.

Hu, Y. and Tung, K. K. (2002): Interannual and decadal variations of planetary wave activity, stratospheric cooling, and northern hemisphere annular mode, *J. Climate*, **15**, 1659–1673.

IPCC Working Group II Contribution to the Fourth Assessment Report, *Climate Change 2007 (2007), Climate Change Impacts, Adaptation and Vulnerability*, Geneva, WHO and UNEP IPCC.

John, V. O. and B. J. Soden (2007), Temperature and humidity biases in global climate models and their impact on climate feedbacks, *Geophy. Res. Lett.,* **34**, L18704, doi:10.1029/2007GL030429.

Kalnay E. et al. (1996), The NCEP/NCAR 40-year reanalysis project, *Bull. Am. Meteorol. Soc*., **77**, 437-471.

Kistler, R. and E. Kalnay (1999), Reanalysis prior to 1958, WMO conference www.emc.ncep.noaa.gov/gmb/bkistler/conf2/conf2.html

Kodera, K. and Y. Kuroda, (2002), Dynamical response to the solar cycle: Winter stratopause and lower stratosphere. *J. Geophys. Res*., **107**, Article 2224.

Kodera, K., and Y. Kuroda (2003), Regional and hemispheric circulation patterns in the northern hemisphere winter, or the NAO and the AO. *Geophys. Res. Lett.*, **30**, doi:10.1029/2003GL017290

Kodera, K. (2004), Solar influence on the Indian Ocean monsoon through dynamical processes, *Geophys. Res. Lett*., **31**, L24209, doi:10.1029/2004GL020928.

Kodera, K. (2005), The role of dynamics in solar forcing, *Space Science Reviews*, **125**, 319-330.

Kushner, P. J., and L. M. Polvani (2004), Stratosphere-troposphere coupling in a relatively simple AGCM: the role of eddies. *J. Climate*, **17**, 629-639.

Labitzke, K. (1982), On the interannual variability of the middle stratosphere during northern winters. *J. Meteor. Soc. Japan,* **60**, 124-139.

Labitzke, K. (2001), The global signal of the 11-year solar cycle in the stratosphere: differences between the solar maxima and minima. *Meteorol. Zeitschrift*, **10,** 901-908.

Labitzke, K. (2003), The global signal of the 11-year sunspot cycle in the atmosphere: When do we need the QBO? *Meteorol. Zeitschrift*, **12**, 209-216.

Lamb, H. H. (1972), *Climate: Present, Past and Future,* Vol.1, 440-464, Methuen &Co Ltd.

Lean, J. (2000), Evolution of the Sun's spectral irradiance since the Maunder Minimum. *Geophys. Res. Lett.*, **27**, 2425-2429.

Lean, J., and D. Rind, (2001), Earth's response to a variable sun. *Science*, **292**, 234-236.

Lee, J. N., and S. Hameed (2007), The Northern Hemisphere annular mode in summer: Its physical significance and its relation to solar activity variations, *J. Geophys. Res.*, 112, D15111, doi:10.1029/2007JD008394.

Lee, J. N., S. Hameed, and D. T. Shindell (2007), The Northern annular mode in summer and Its relation to solar activity variations in the GISS ModelE. *J. Atm. Sol. Terr. Phys.*, **70/5,** 730-741, doi:10.1016/j.jastp.2007.10.012.

Lee, H. and A. Smith (2003), Simulation of the combined effects of solar cycle, quasi-biennial oscillation, and volcanic forcing on stratospheric ozone changes in recent decades. *J. Geophys. Res.,* **108**(D2), 4049, doi:10.1029/2001JD001503.

Li, D. and K. P. Shine (1995), A 4-Dimensional Ozone Climatology for UGAMP Models, UGAMP Internal Report No. 35.

Limpasuvan, V., and D. L. Hartmann (2000), Wave-maintained annular modes of climate variability. *J. Climate*, **13**, 4414-29.

Lin, H., J. Derome, R.J. Greatbatch, K.A. Peterson and J. Lu (2002), Tropical links of the Arctic Oscillation. *Geophys. Res. Lett.*, **29**(20), 1943, doi:10.1029/2002GL015822.

Lindzen, R. S., M. D. Chou, and A. Y. Hou (2001), Does the Earth have an adaptive infrared Iris? *Bull. Amer. Meteor. Soc*., **82**, 714-432.

van Loon, H., and K. Labitzke (1998), The global range of the stratospheric decadal wave. Part I: Its association with the sunspot cycle in summer and in the annual mean and with the troposphere, *J. Clim*., **11**, 1529-1537.

van Loon, H., G. A. Meehl, and J. M. Arblaster (2004), A decadal solar effect in the tropics in July–August, *J. Atmos. Sol. Terr. Phys*., **66**, 1767–1778, doi:10.1016/j.jastp.2004.06.003.

van Loon, H., G. A. Meehl, and D. J. Shea (2007), Coupled air-sea response to solar forcing in the Pacific region during northern winter, *J. Geophys. Res*., **112**, doi:10.1029/2006JD007378.

Lund, D. C, J. Lynch-Stieglitz and W. B. Curry (2006), Gulf Stream density structure and transport during the past millennium, *Nature,* **444**, 601-604.

Matsuno, T. (1970), Vertical Propagation of Stationary Planetary Waves in the Winter Northern Hemisphere, *J. of Atoms. Sci.* **27,** 871-883.

Matthes K. (2003), Der Einfluss des 11-jährigen Sonnenfleckenzyklus and der QBO auf die Atmosphäre – eine Modellstudie, *PhD theses at the geoscience department of the Freie Universität Berlin,* 250pp (http://www.diss.fuberlin.de/2003/325/).

Matthes K, K. Kodera, J. Haigh, D. T. Shindell, K. Shibata, U. Langematz, E. Rozanov, and Y. Kuroda (2003), GRIPS solar experiments intercomparison project : initial results. *Meteorolo. and Geophys*., **54,** 71-90.

Matthes, K., Y. Kuroda, K. Kodera, and U. Langematz (2006), Transfer of the Solar Signal from the Stratosphere to the Troposphere: Northern Winter, *J. Geophys. Res.,* **111**, D06108, doi:10.1029/2005JD006283.

Meehl, G. A., and A. Hu (2006), Megadroughts in the Indian monsoon region and southwest North America and a mechanism for associated multi-decadal Pacific sea surface temperature anomalies, *J. Clim*., **19**, 1605– 1623.

Meehl, G. A., W. M. Washington, T. M. L. Wigley, J. M. Arblaster, and A. Dai (2003), Solar and greenhouse gas forcing and climate response in the twentieth century, *J. Clim*., **16**, 426– 444.

Miles, T., W. L. Grose, E. E. Remsberg, and G. Lingenfelser(1994), Evolution of the Southern Hemisphere Subpolar Middle Atmosphere during Summer and Autumn. *J. Atmos. Sci.*, **51**, 677-693.

Miller, R. L., G. A. Schmidt, and D. T. Shindell (2006), Forced annular variations in the 20th century Intergovernmental Panel on climate change fourth assessment report models *J. Geophys. Res.,* **111**, D18101, doi:10.1029/2005JD006323.

Mo, K. C., X. L. Wang, R. Kistler, M. Kanamitsu, and E. Kalnay (1995), Impact of satellite data on the CDAS-Reanalysis system. *Mon. Weather Rev.,* **123,** 124-139**.**

Muench, H. S. (1968), Large-scale disturbances in the summertime stratosphere. *J. Atmos. Sci.*, **25**, 1108-1115.

North G. R., T.L. Bell, R.F. Cahalan, and F.J. Moeng (1982), Sampling errors in the estimation of empirical orthogonal functions. *Mon. Wea. Rev*., **110**, 699-706.

Ogi, M., K. Yamazaki, and Y. Tachibana (2004), The summertime annular mode in the Northern Hemisphere and its linkage to the winter mode. *J. Geophys. Res*.,

109 (D20114), 1-15.

Palmer T. N. (1981), Diagnostic study of a wavenumber-2 stratospheric sudden warming in a transformed Eulerian-mean formalism. *J. Atmos. Sci*, **38**, 844–855.

Penner, J. E., and J. S. Chang (1978), Possible variations in atmospheric ozone related to the 11-year solar cycle, *Geophys. Res. Lett*., **5,** 817-820.

Pierrehumbert, R. T., (2001), Basic principles of climate, Proceedings of 2001 program in Geophysical Fluid Dynamics: Conceptual Models of the climate, Woods Hole Oceanographic Institution, http://www.whoi.edu/cms/files/lect_07_2001_21421.pdf.

Pierrehumbert R.T., H. Brogniez, and R. Roca (2005), On the relative humidity of the atmosphere. in *The Global Circulation of the Atmosphere*, T. Schneider and A. Sobel, eds. Princeton University Press.

Randel, W. J. (1993), Global normal-mode Rossby waves observed in stratospheric ozone data. *J. Atmos. Sci*., **50**, 406-420.

Salby M. L., Callaghan P. F. (2005), Interaction between the Brewer-Dobson Circulation and the Hadley Circulation. *J. of Climate,* **18(20),** 4303.

Salby M. L. and Callaghan P. F. (2006), Influence of the solar cycle on the general circulation of the stratosphere and upper troposphere. *Space Science Reviews* ,**125**, 287-303.

Schmidt, H., G. P. Brasseur, M. Charron, E. Manzini, M. A. Giorgetta, V. I. Fomichev, D. Kinnison, D. Marsh, and S. Walters (2006), The HAMMONIA chemistry climate model: Sensitivity of the mesopause region to the 11-year solar cycle and CO2 doubling, *J. Clim.,* **19**, 3903–3931.

Schmidt, G. A., R. Ruedy, J. E. Hansen, I. Aleinov, N. Bell, M. Bauer, S. Bauer, B. Cairns, V. Canuto, Y. Cheng, A. Del Genio, G. Faluvegi, A. D. Friend, T. M. Hall, Y. Hu, M. Kelley, N. Y. Kiang, D. Koch, A. A. Lacis, J. Lerner, K. K. Lo, R. L. Miller, L. Nazarenko, V. Oinas, Ja. Perlwitz, Ju. Perlwitz, D. Rind, A. Romanou, G. L. Russell, M. Sato, D. T. Shindell, P. H. Stone, S. Sun, N. Tausnev, D. Thresher, and M.-S. Yao (2006), Present day atmospheric simulations using GISS ModelE: Comparison to in-situ, satellite and reanalysis data, *J. Clim*., **19**, 153-192.

Seager, R., N. Harnik, Y. Kushnir, W. Robinson, J. Miller (2006), Mechanisms of Hemispherically Symmetric Climate Variability, *J. of Clim*., **16**, 2960.

Shindell, D., Rind, D., Balachandran, N., Lean, J., and Lonergan, P. (1999a), Solar cycle variability, ozone, and climate, *Science,* **284**, 305–308.

Shindell, D. T., R. L. Miller, G. A. Schmidt, and L. Pandolfo (1999b), Simulation of the recent northern winter climate trends by greenhouse forcing of a stratospheric model, *Nature*, **399**, 452-455.

Shindell, D. T., G. A. Schmidt, R. L. Miller, and D. Rind (2001), Northern Hemisphere winter climate response to greenhouse gas, ozone, solar, and volcanic forcing, *J. Geophys. Res*., **106**, 7193-7210.

Shindell, D. T., G. Faluvegi, N. Unger, E. Aguilar, G. A. Schmidt, D. Koch, S. E. Bauer, and R. L. Miller (2006a), Simulations of preindustrial, present-day, and 2100 conditions in the NASA GISS composition and climate model G-PUCCINI, *Atmos. Chem. Phys*., **6**, 4427-4459.

Shindell, D. T., G. Faluvegi, R. L. Miller, G. A. Schmidt, J. E. Hansen, and S. Sun (2006b), Solar and anthropogenic forcing of tropical hydrology, *Geophys. Res. Lett.,* **33**, L24706, doi:10.1029/2006GL027468.

Shukla J. and J. L. Kinter III (2006), Predictability of seasonal climate variations: a pedagogical review, *Predictability of Weather and Climate*, 306-341, Cambridge University Press.

Solanki, S. K., and Fligge, M. (2000), Reconstruction of past solar irradiance. *Space science reviews,* **94**, 127-138.

Song, Y., and W. A. Robinson (2004), Dynamical mechanisms of stratospheric influences on the troposphere. *J. Atmos. Sci*., **61,** 1711-25.

Sun, S., and R. Bleck (2006), Multi-Century Simulations with the Coupled GISS-HYCOM Model: Control Experiments, *Climate Dynamics*, **26**, 407-428.

Sun, D-Z, and I. M. Held (1996), A comparison of modeled and observed relationships between interannual variations of water vapor and temperature**.** *J. of Climate,* **9(4)**, 665-675.

Thompson D. W. J. and J. M. Wallace (1998), The Arctic Oscillation signature in the wintertime geopotential height and temperature fields. *Geophys. Res. Lett.,* **25***,* 1297-1300.

Thompson D. W. J., and J. M. Wallace (2000), Annular modes in the extratropical circulation. Part I: Month-to-month variability. *J. Clim.,* **13**, 1000-1016.

Thompson D. W. J., and J. M. Wallace (2001), Regional Climate Impacts of the Northern Hemisphere Annular Mode, *Science*, **293**, 85-89.

Thompson, D. W. J., J. C. Furtado, and T. G. Shepherd (2005), The Direct Effect of Stratospheric Variability on the Troposphere, submitted to the *J. of Atm. Sci.*

Wagner R. E. and K.P. Bowman (2000), Wavebreaking and mixing in the Northern Hemisphere summer stratosphere. *J. Geophys. Res.*, **105**, 24,799-24,807.

Woods, T.N., J. Fontenla, J. Harder, G. Kopp, W. McClintock, P. Pilewskie, E. Richard, and M. Snow (2008), What we've learned from SORCE – Solar Cycle Maximum to Minimum, Proceedings of 2008 SORCE meeting.

White, W. B., Dettinger, M. D., and Cayan, D. R. (2003), Sources of global warming of the upper ocean on decadal period scales, *J. Geophys. Res.* **108**, doi:10.1029/ 2002JC001.

Zerefos, C. S. and J. P. Crutzen (1975), Stratospheric thickness variations over the northern hemisphere and their possible relation to solar activity, *J. Geophy. Res.*, **80**, 5041-5043.

Zhang, T. and K. Stamnes and S. A. Bowling (2001), Impact of the Atmospehric Thickness on the Atmospheric Downwelling Longwave Radiation and Snowmelt under Clear-Sky Conditions in the Arctic and Subarctic. *J. of Climate*, **14**, 920-939.

Figures

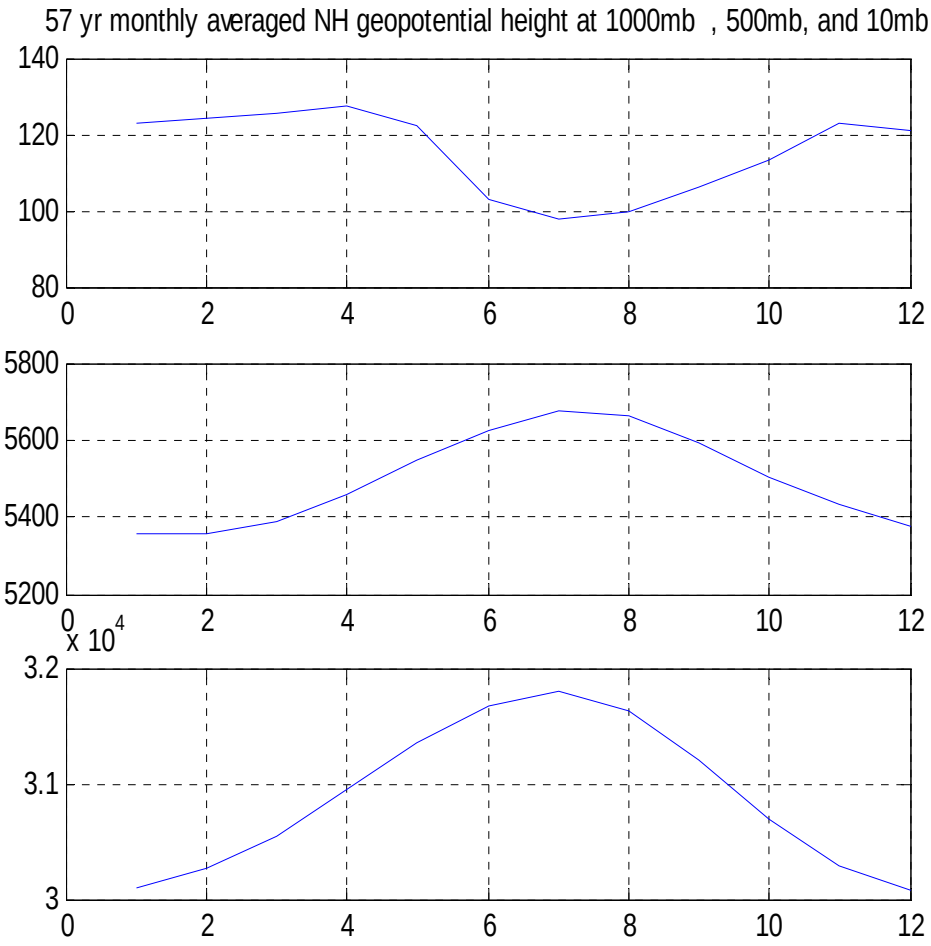

Figure 2.1 The annual march of 57 year(1948-2004) averaged NH geopotential height (in *m*) from January to December at 1000 hPa, 500 hPa, and 10 hPa (from top to bottom). The numbers in the x-axis denotes the month (1 for January and 12 for December).

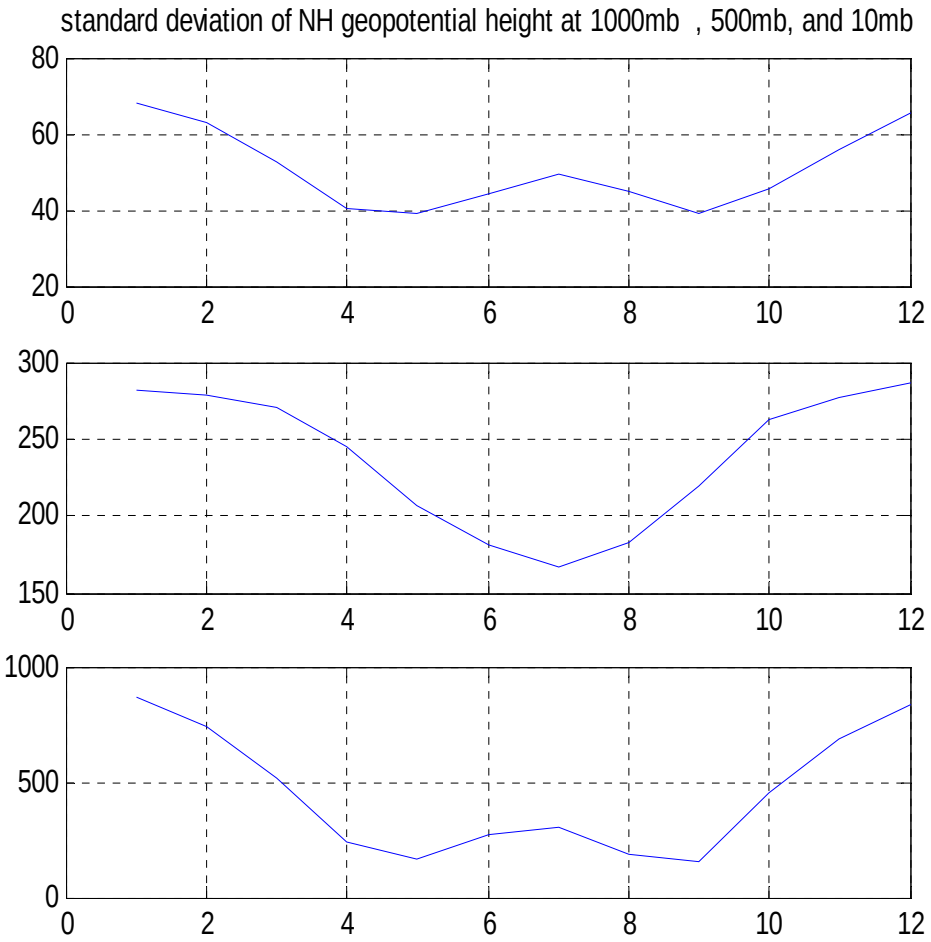

Figure 2.2 The annual march of the standard deviation of the NH geopotential height (in *m*) from January to December at 1000 hPa, 500 hPa, and 10 hPa (from top to bottom). The numbers in the x-axis denotes the month (1 for January and 12 for December).

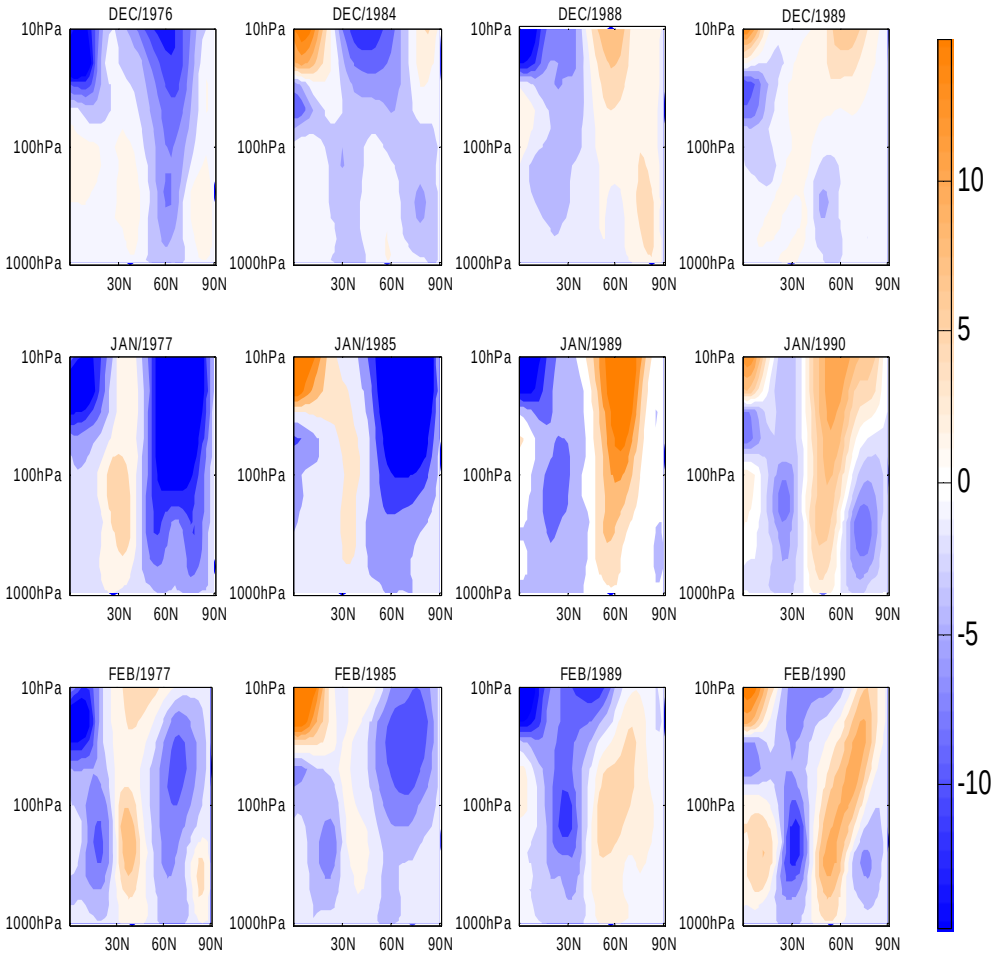

Figure 2.3 Anomalous zonal mean zonal winds (m/s) from the NCEP/NCAR reanalysis; for the winter of 1977, 1985, 1989, and 1990; for December, January, and February from top to bottom. The climatology for the monthly zonal winds is based on the average of 1948-2004.

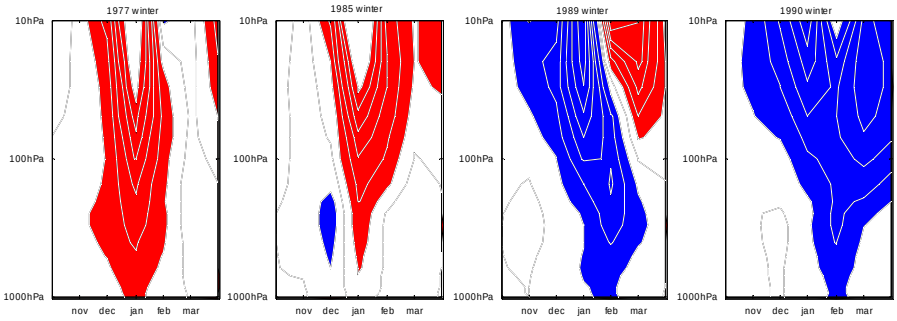

Figure 2.4 Time-height development of the normalized northern annular mode index during the four winters (1997, 1985, 1989, and 1990) from October to March. Red represents negative NAM index values (a warm, disturbed polar vortex) and blue positive NAM index values (strong and cold polar vortex). Each line represents 0.2 times of one standard deviation of the NAM indexes during 1948-2004.

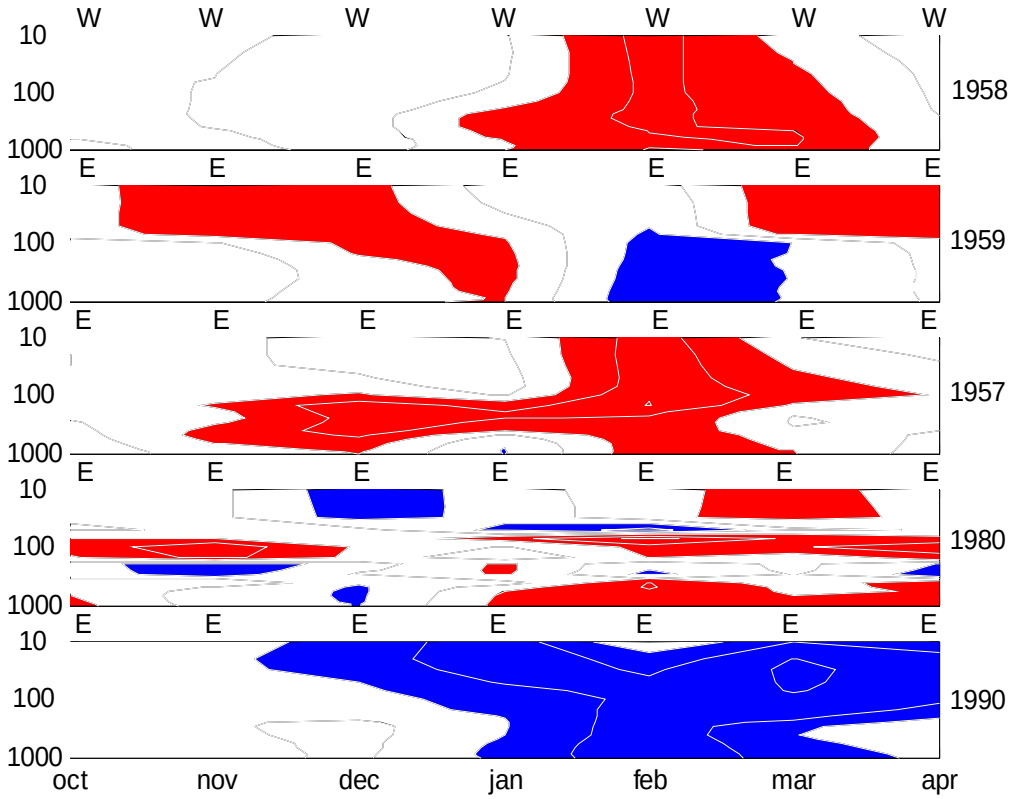

Figure 3.1 Time-height development of the northern annular mode during the five winters which had the strongest solar activity during 1948-2004. Values greater than one standard deviation are shown in color, and contour interval is one standard deviation. Equatorial zonal wind direction at 50hPa is shown for each month above each panel. Red represents negative values and blue positive values.

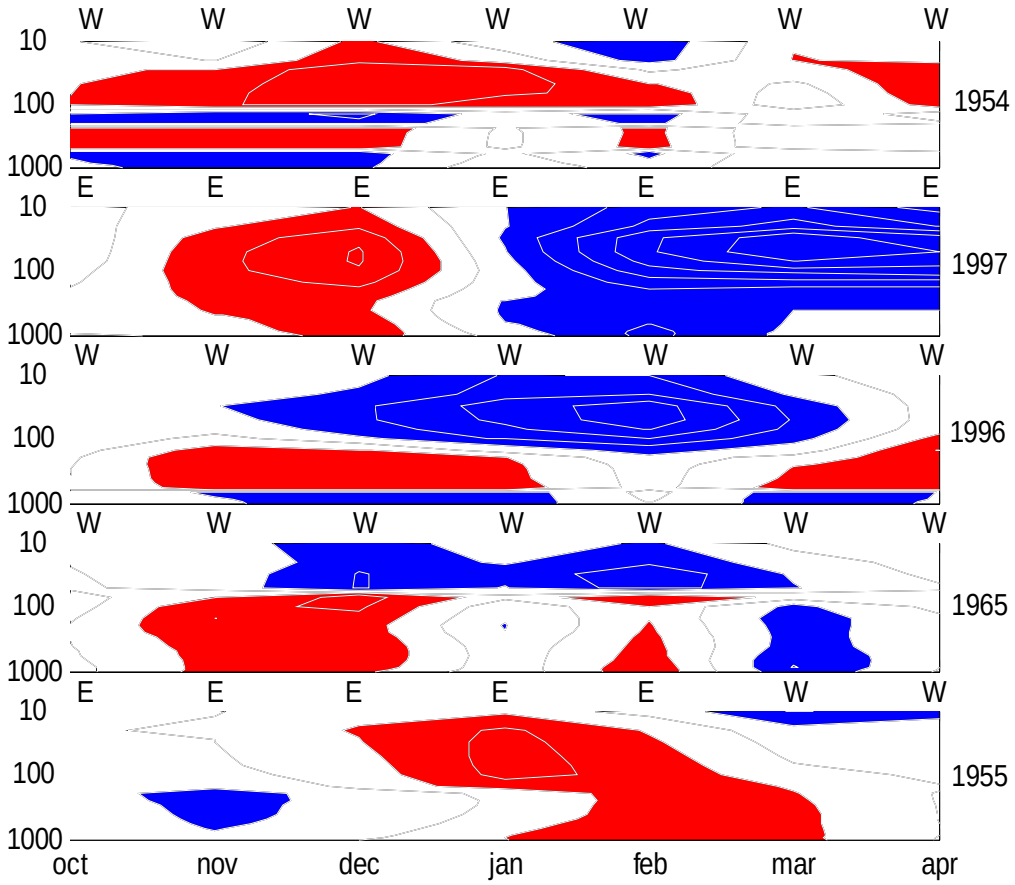

Figure 3.2 Same as Figure 3.1, but for the five winters which had the weakest solar activity during 1948-2004.

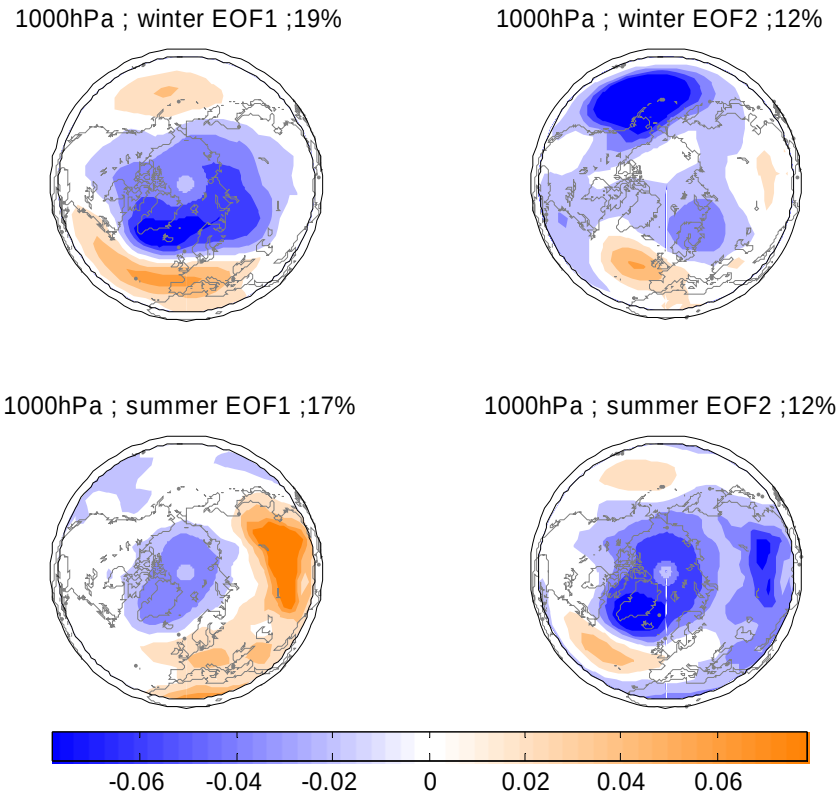

Figure 4.1 NAM patterns for extended winter ((a) and (b) from October to April) and summer ((c) and (d) from May to September) at 1000 hPa. The patterns are calculated as the first and second EOFs of monthly geopotential height for 1948-2004.

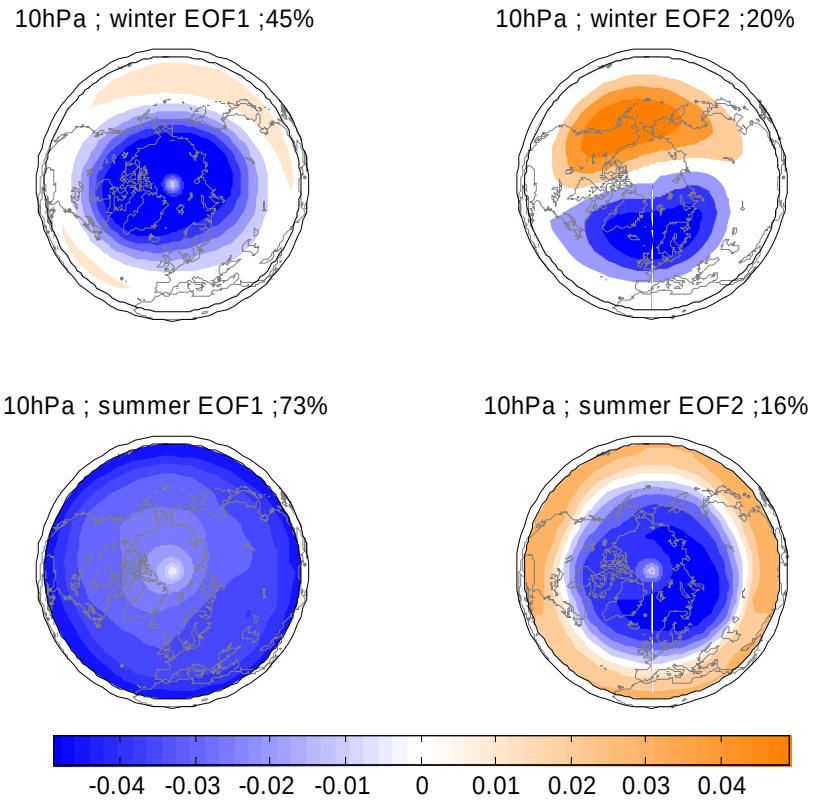

Figure 4.2 NAM patterns for extended winter ((a) and (b) from October to April) and summer ((c) and (d) from May to September) at 10 hPa. The patterns are calculated as the leading EOF of monthly geopotential height for 1948-2004.

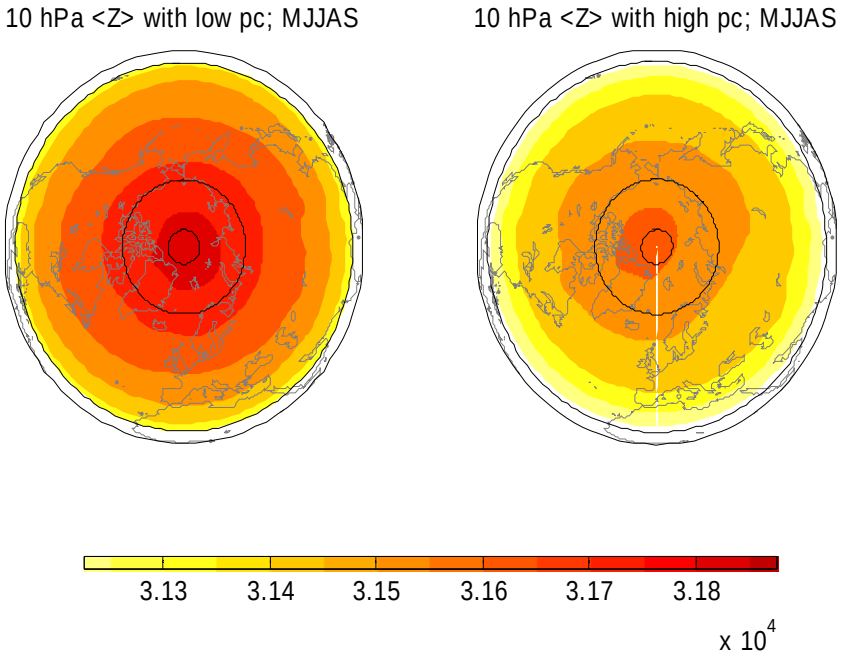

Figure 4.3 Composites of NCEP Geopotential height fields for low NAM index (left) and high NAM index (right) at 10 hPa for May to September; 1948-2004. The 70°N and 85°N circles are shown for reference. The 20°N latitude is shown as the southern limit of the region being analyzed.

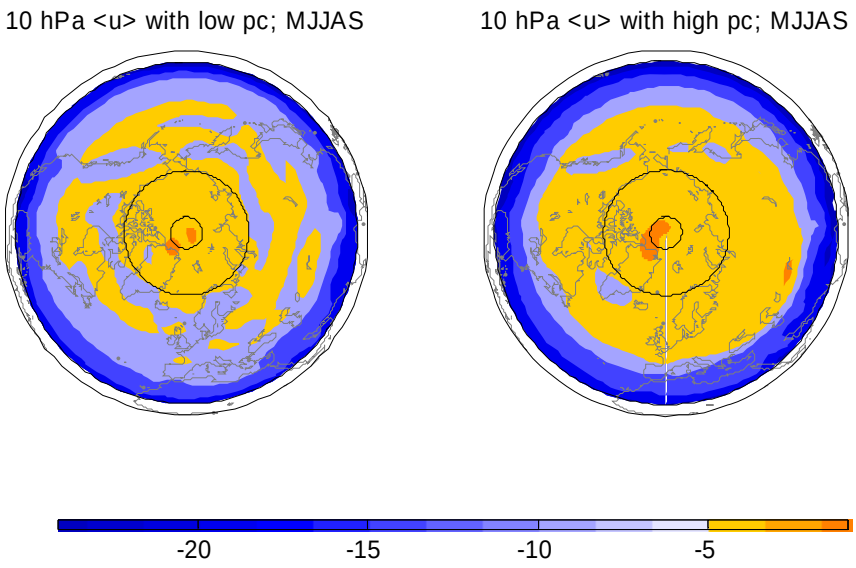

Figure 4.4 Composite of NCEP zonal wind fields (in m/s) for low NAM index (left) and high NAM index (right) at 10 hPa from May to September; 1948-2004. The 70°N and 85°N circles are shown for reference. The 20°N latitude is shown as the southern limit of the region being analyzed.

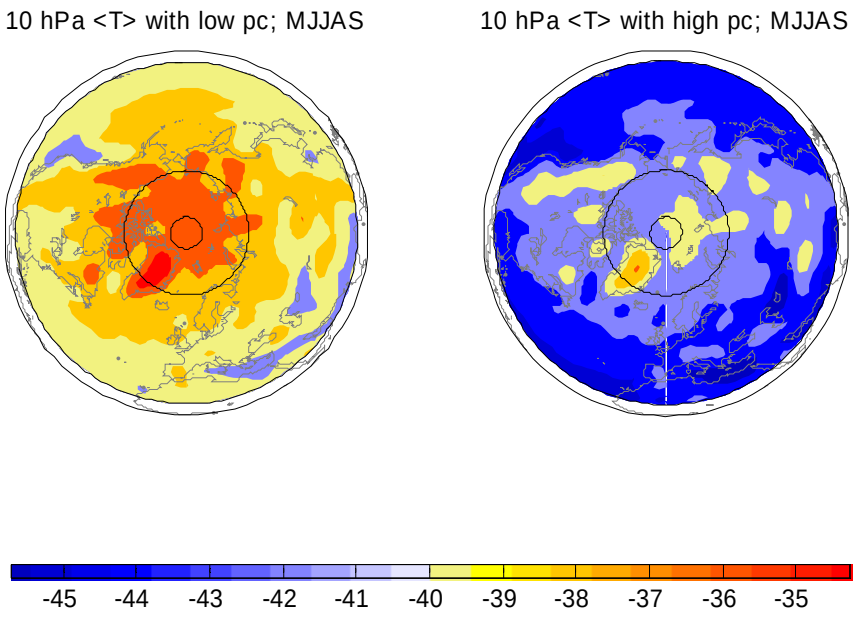

Figure 4.5 Composite of NCEP air temperature fields for low NAM index (left) and high NAM index (right) at 10 hPa from May to September; 1948-2004. The 70°N and 85°N circles are shown for reference. The 20°N latitude is shown as the southern limit of the region being analyzed.

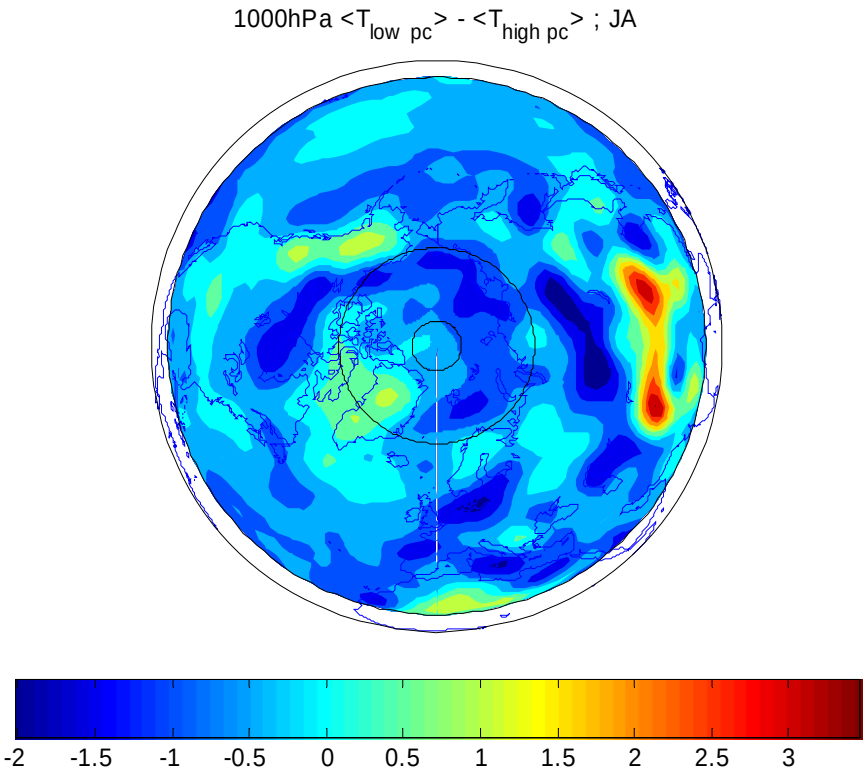

Figure 4.6 Composite difference of NCEP air temperature fields for low NAM and high NAM index at 1000 hPa for July and August; 1948-2004. The 70°N and 85°N circles are shown for reference. The 20°N latitude is shown as the southern limit of the region being analyzed.

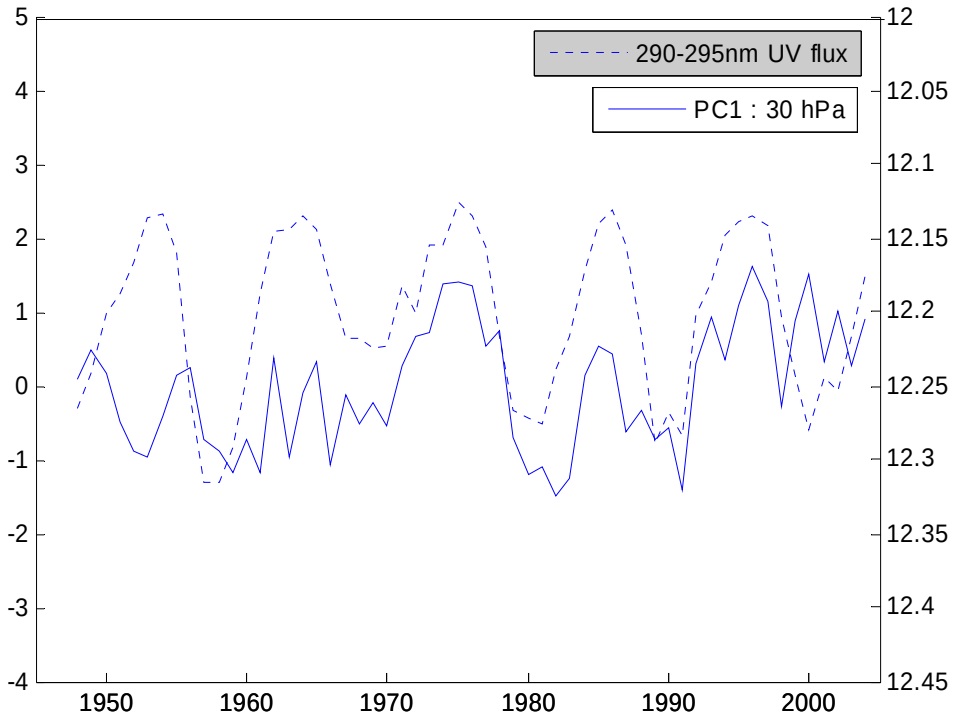

Figure 4.7 Principal component of the first EOF in the 30 hPa heights in July and August averaged geopotential heights in the Northern Hemisphere with the solar UV flux (200 – 295 nm). The UV flux scale is inverted.

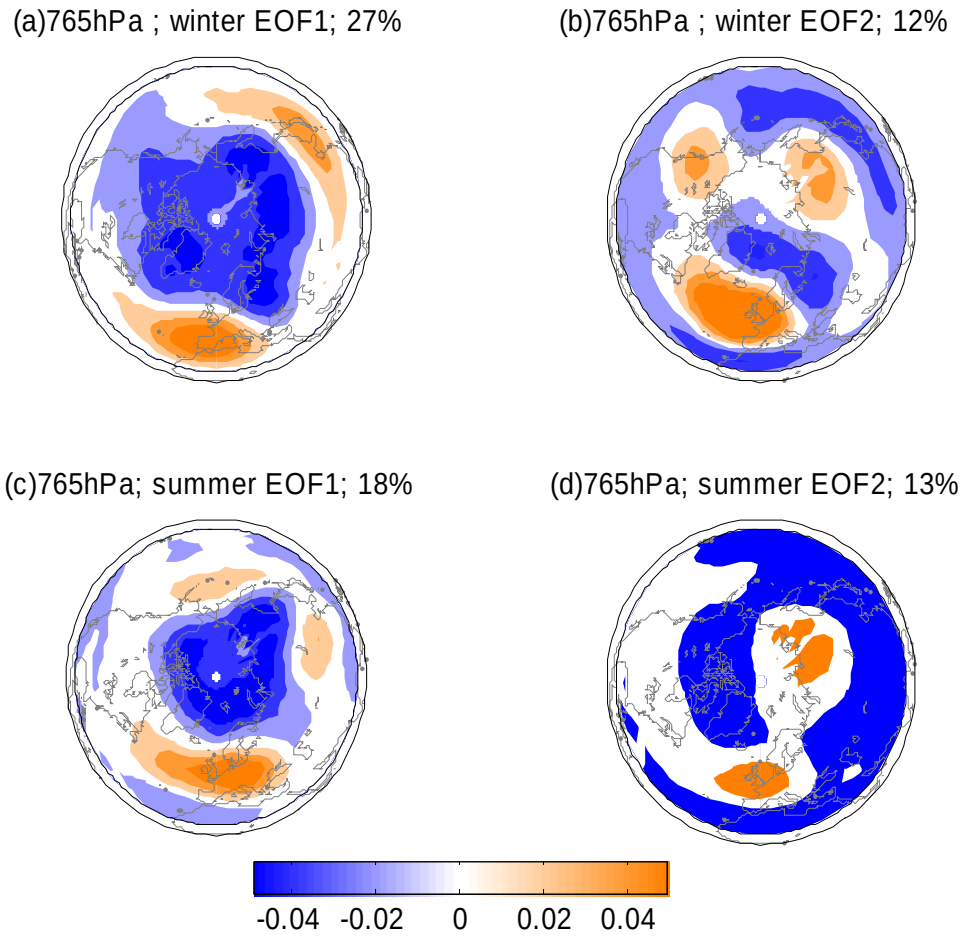

Figure 5.1 NAM patterns for extended winter((a) and (b) from October to April) and summer ((c) and (d) from May to September) at 765 hPa. The patterns are calculated as the first and second EOFs of 17 years of monthly geopotential height from GISS/modelE PD simulation.

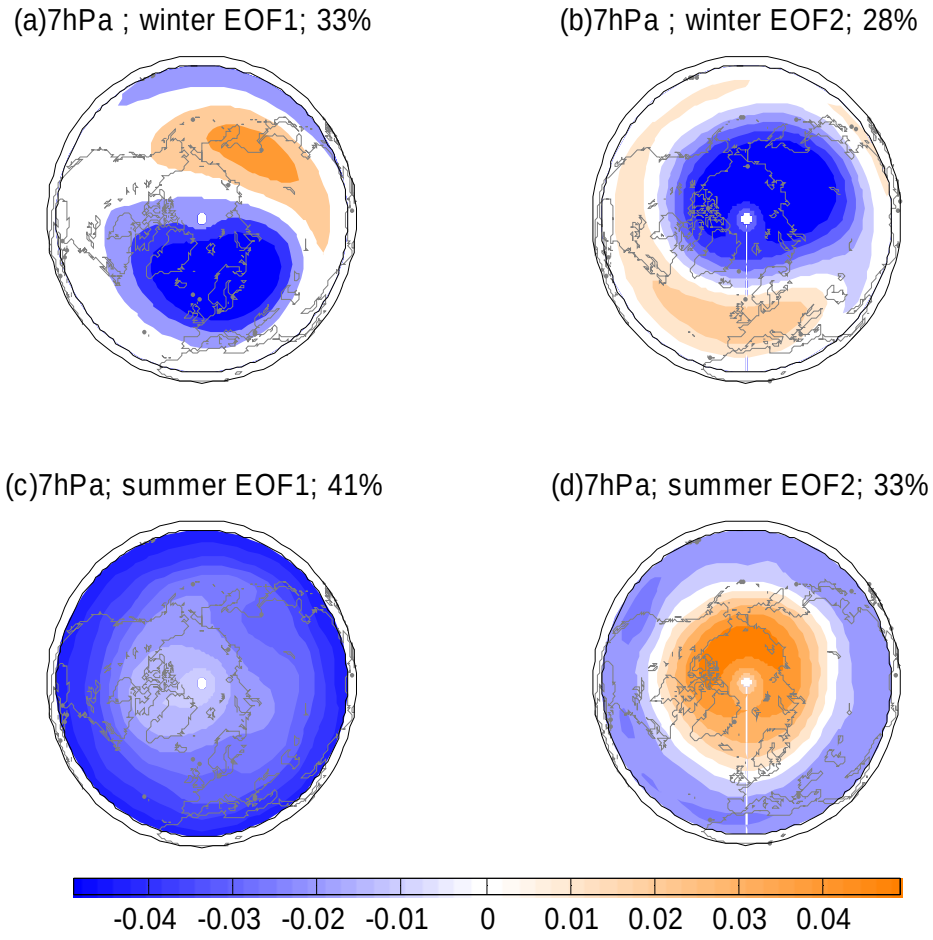

Figure 5.2 NAM patterns for winter ((a) and (b) from October to April) and summer ((c) and (d) from May to September) at 7 hPa. The patterns are calculated as the leading EOF of 17 years of monthly geopotential height from GISS/ModelE PD simulation.

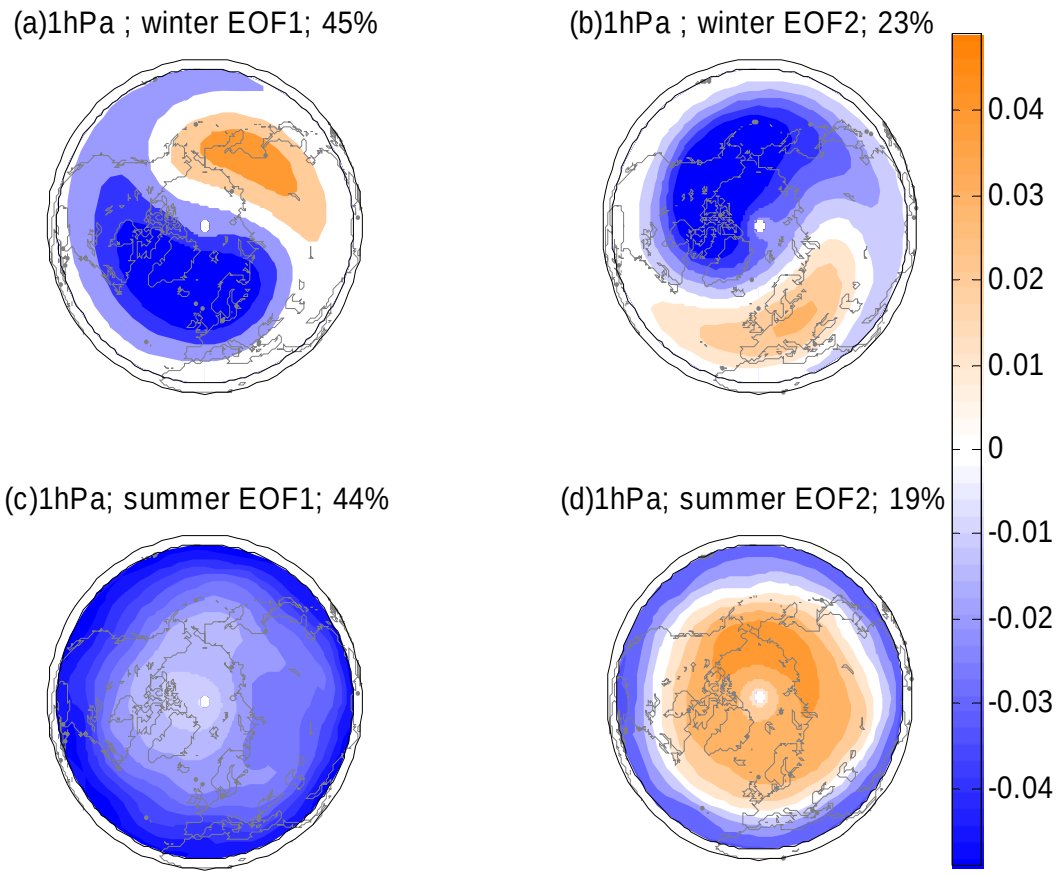

Figure 5.3 NAM patterns for winter ((a) and (b) from October to April) and summer ((c) and (d) from May to September) at 1hPa. The patterns are calculated as the leading EOF of 17 years of monthly geopotential height from GISS/ModelE PD simulation.

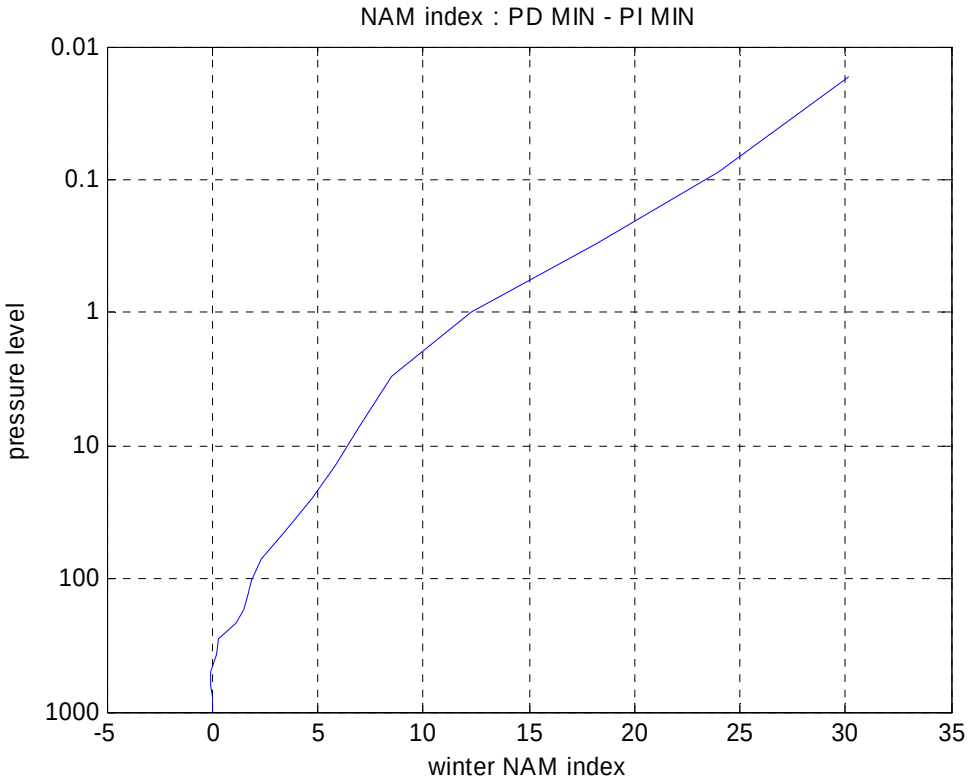

Figure 5.4 Difference of winter NAM index between PD and PI simulation.

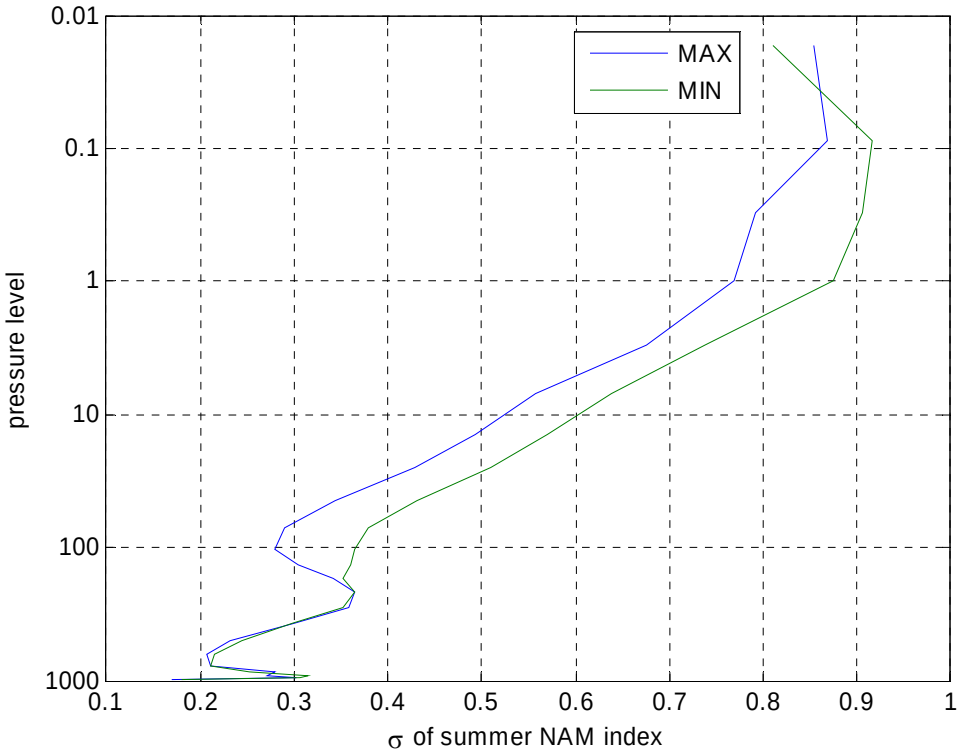

Figure 5.5 Comparison of standard deviation of summer NAM index during the 17 years of MAX and MIN run.

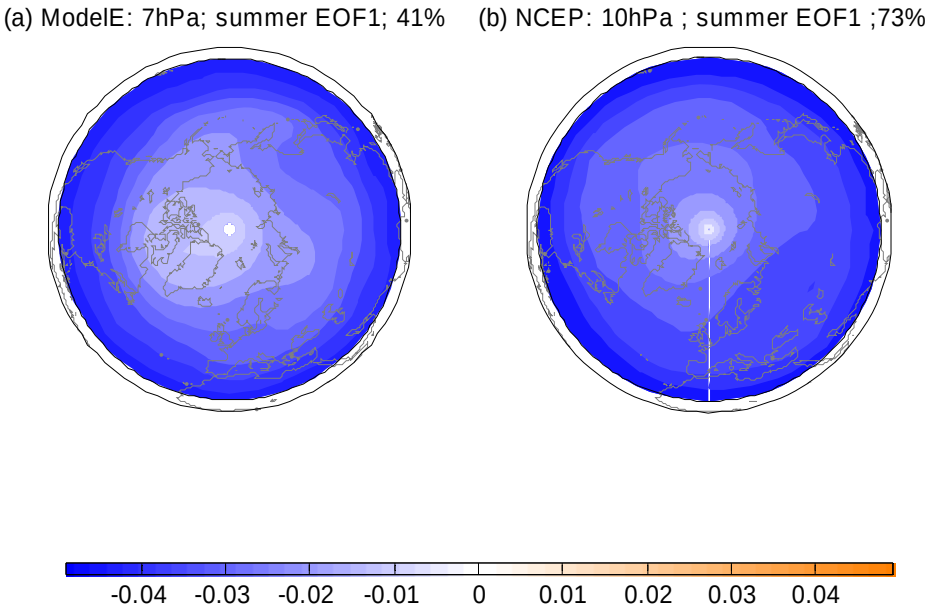

Figure 5.6 NAM patterns for summer (from May to September) for (a) the GISS ModelE run at 7hPa (left), and for (b) NCEP/NCAR reanalysis at 10hPa (right). The patterns are calculated as the first EOFs of monthly geopotential height anomalies from 20ºN to 90ºN.

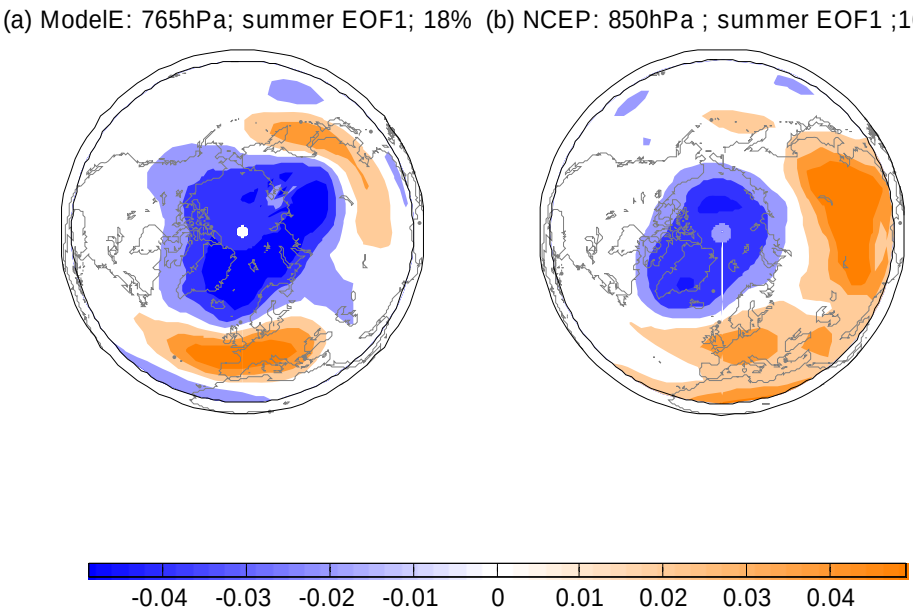

Figure 5.7 NAM patterns for summer (from May to September) for (a) GISS ModelE run at 765hPa (left) and for (b) NCEP/NCAR reanalysis at 850hPa (right). The patterns are calculated as the first EOFs of monthly geopotential height anomalies from 20ºN to 90ºN.

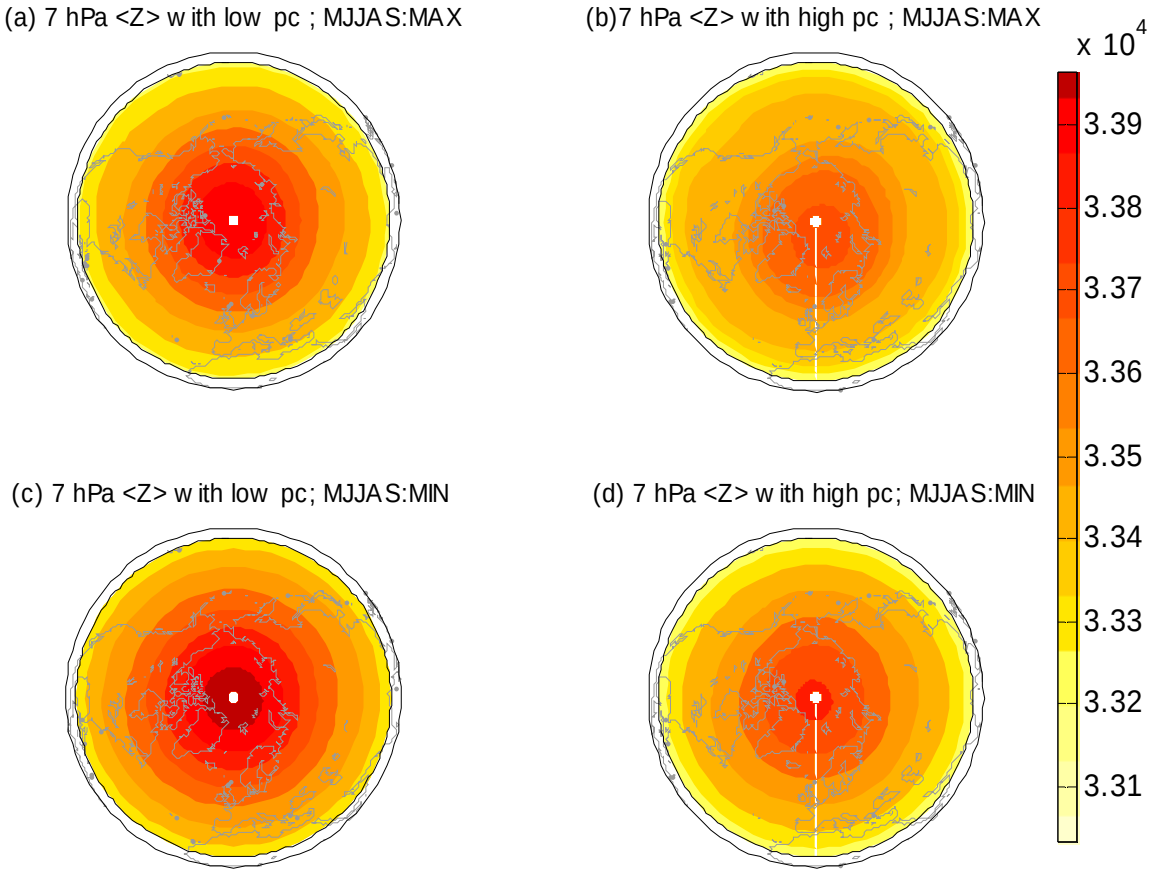

Figure 5.8 Composites of geopotential height fields from GISS ModelE MAX and MIN simulations for low NAM index (left) and high NAM index (right) at 7hPa from May to September. For the low NAM composites, 11 months for MAX run and 14 months for MIN run are averaged in Figure 5.8(a) and 5.8(c), respectively. For the high NAM composites, 12 months for MAX run and 16 months for MIN run are averaged in Figure 5.8(b) and 5.8(d), respectively.

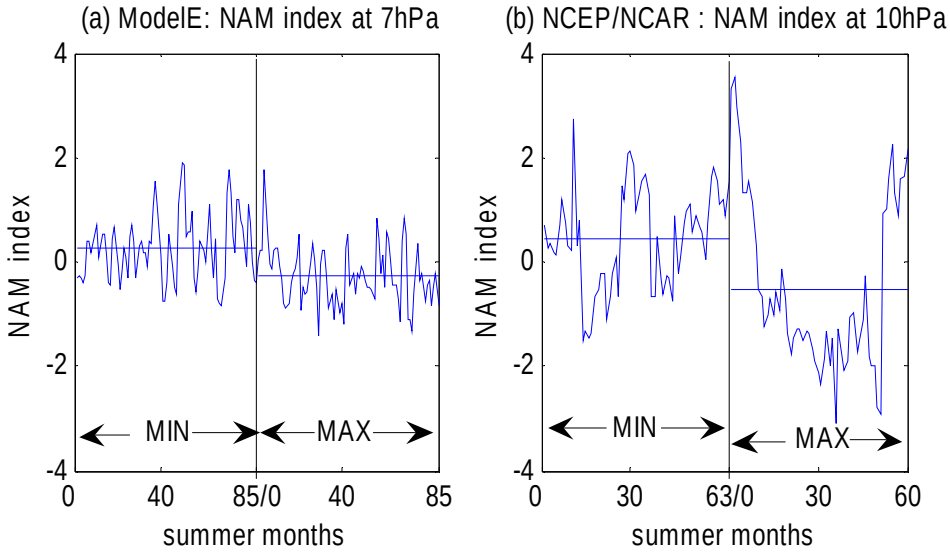

Figure 5.9 NAM index for summer (from May to September) for (a) GISS ModelE MIN/MAX run at 7hPa (left) and (b) NCEP/NCAR reanalysis at 10hPa (right) for solar minimum/maximum. The horizontal solid lines represent the mean of each NAM indexes. The MIN/MAX period are composed from 17 years of summer (from May to September) from MIN/MAX run for (a) the model and 63 months/60 months of solar minimum/maximum months grouped by the monthly mean UV flux below/above standard deviation from the mean during 1948-2004 for (b) NCEP/NCAR reanalysis.

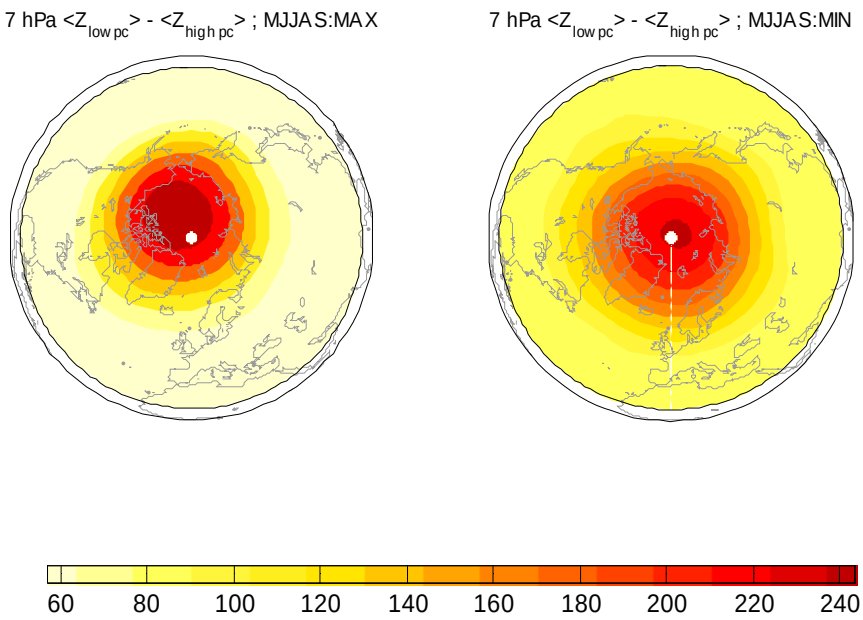

Figure 5.10 Composites of summer geopotential height fields difference between low NAM index and high NAM index in m for MAX simulation (left) and MIN simulation (right) at 7 hPa.

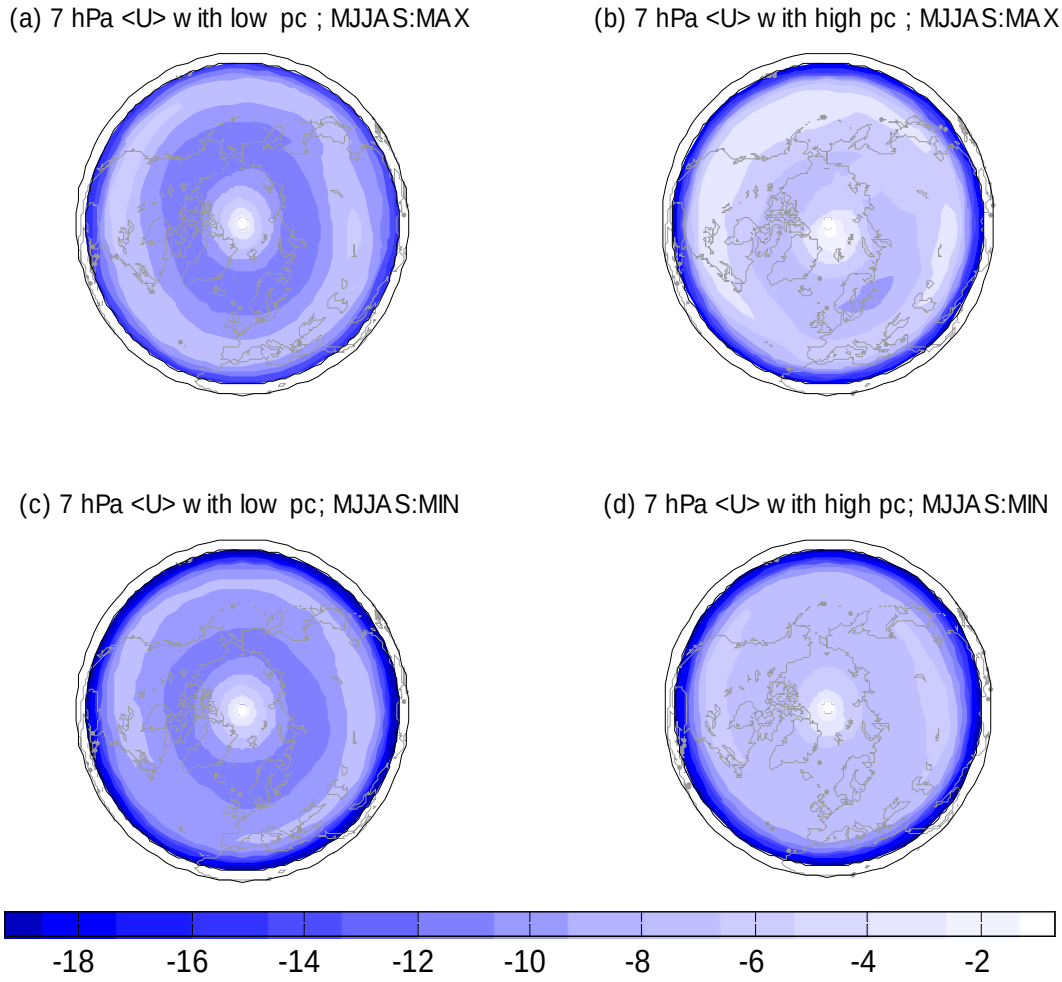

Figure 5.11 Composites of zonal wind fields from GISS ModelE MAX and MIN simulation for low NAM index (left) and high NAM index (right) in m/s at 7hPa from May to September. For the low NAM composites, 11 months for MAX run and 14 months for MIN run are averaged in Figure 5.11(a) and 5.11(c), respectively. For the high NAM composites, 12 months for MAX run and 16 months for MIN run are averaged in Figure 5.11(b) and 5.11(d), respectively.

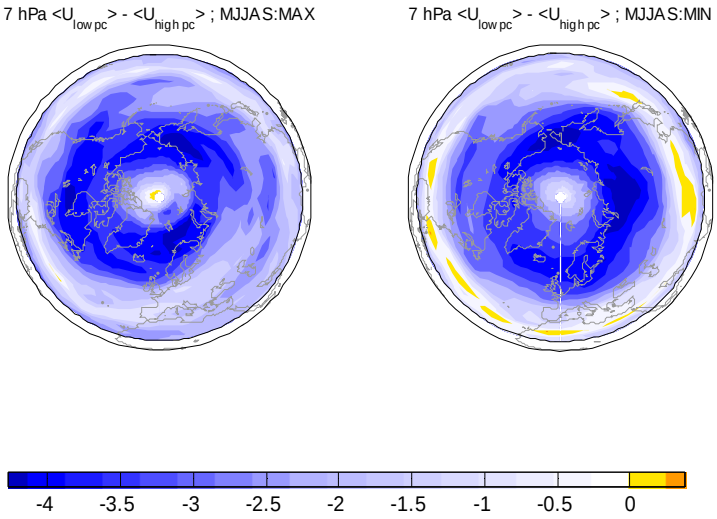

Figure 5.12 Composites of summer zonal wind fields difference between low NAM index and high NAM index in m/s for MAX simulation (left) and MIN simulation (right) at 7 hPa.

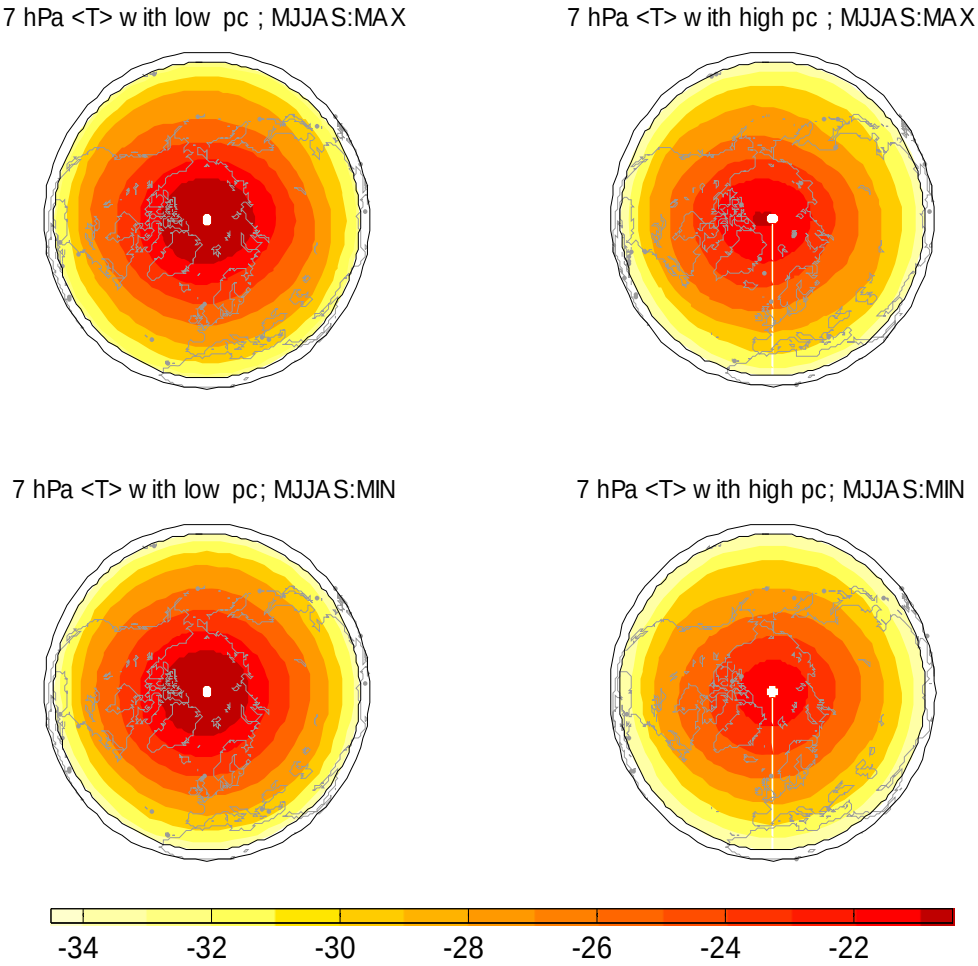

Figure 5.13 Composites of summer temperature fields for low NAM index and high NAM index in K for GISS ModelE MAX simulation (left) and MIN simulation (right) at 7 hPa. For the low NAM composites, 11 months for MAX run and 14 months for MIN run are averaged in Figure 5.13(a) and 5.13(c), respectively. For the high NAM composites, 12 months for MAX run and 16 months for MIN run are averaged in Figure 5.13(b) and 5.13(d), respectively.

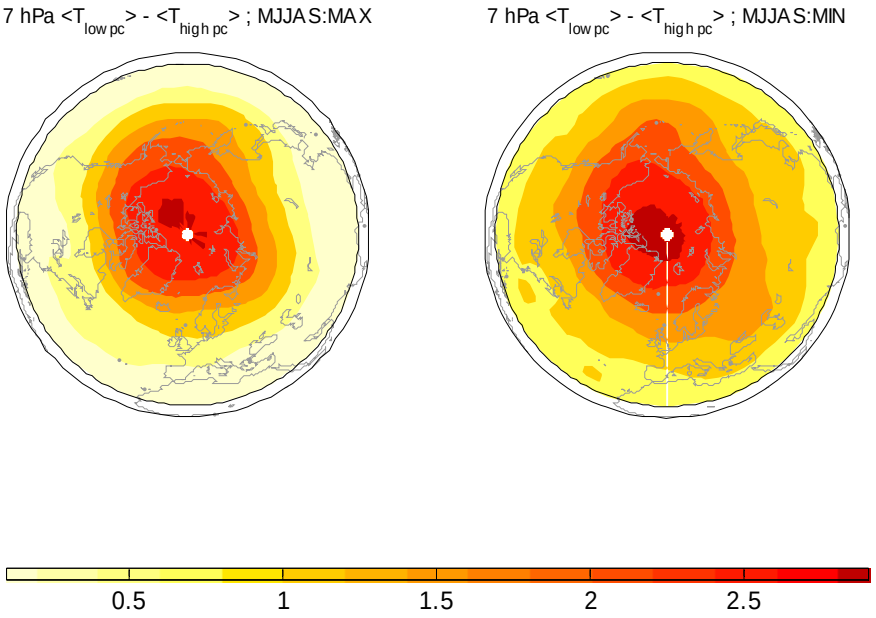

Figure 5.14 Composites of summer temperature difference between low NAM index and high NAM index in K for MAX run (left) and MIN run (right) at 7 hPa.

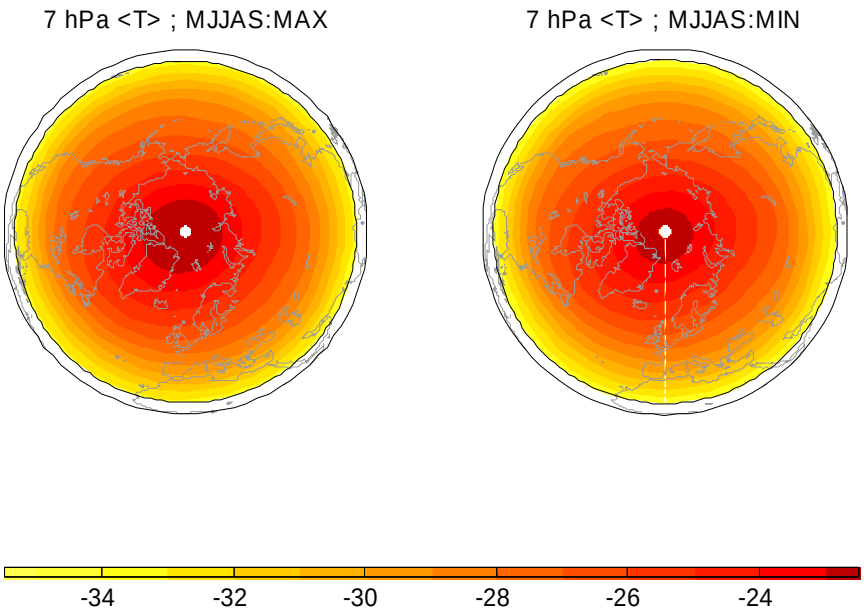

Figure 5.15 Composites of ModelE air temperature fields for MAX (left) and MIN (right) runs for 17 years at 7hPa from May to September. The temperature difference and its statistical significance are discussed in Figure 11.

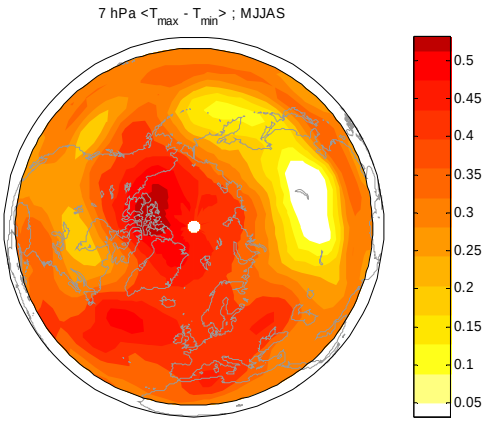

Figure 5.16 Composite of temperature difference in K between MAX run and MIN run at 7 hPa. The difference in the temperature is significant throughout the hemisphere at the 95% significant level based on the *Student t*-test, except in the middle of the Asian continent.

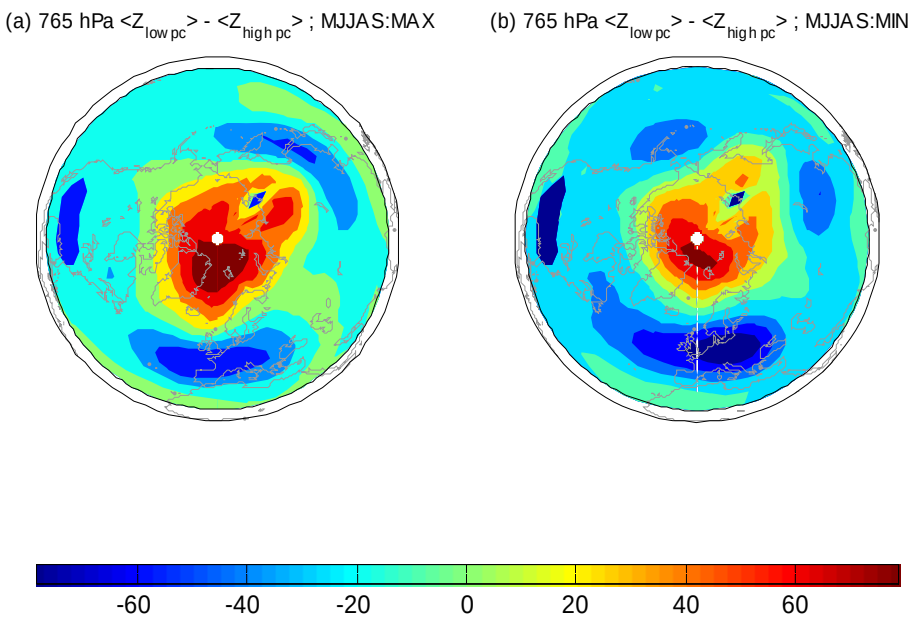

Figure 5.17 Composites of ModelE summer geopotential height fields difference between low NAM index and high NAM index in m for (a) MAX run (left) and (b) Min run (right) at 765 hPa.

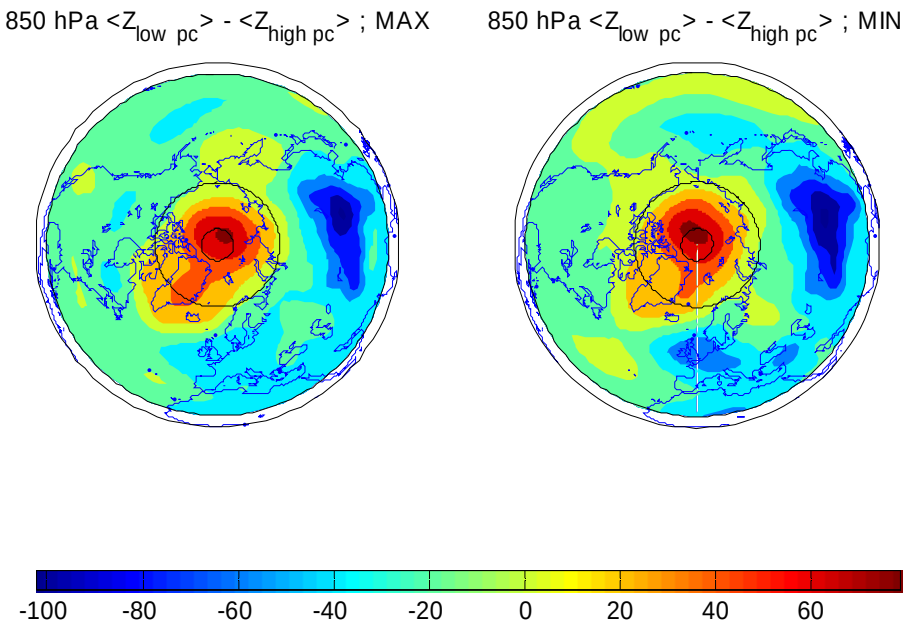

Figure 5.18 Composites of NCEP/NCAR summer geopotential height fields difference between low NAM index and high NAM index in m for solar maximum (left) and solar minimum (right) at 850 hPa.

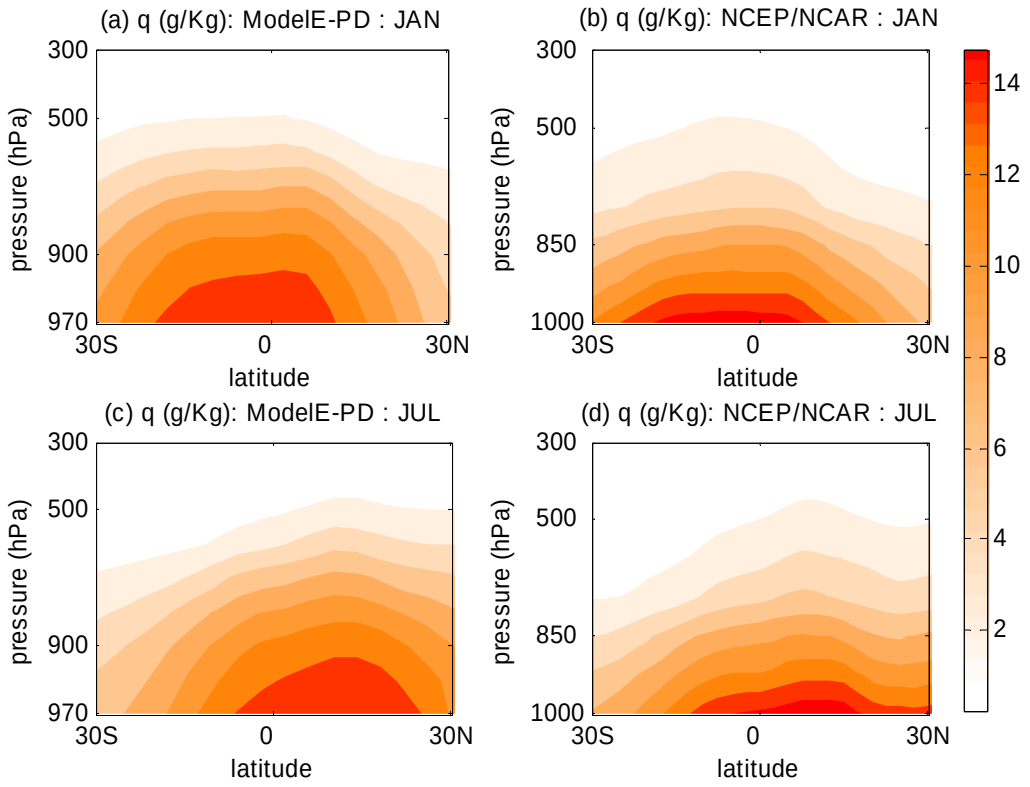

Figure 6.1 The zonally averaged specific humidity (g/Kg) in January (a) for the model-PD simulation (upper left) and (b) for the NCEP/NCAR reanalysis (upper right), and in July (c) for the model-PD simulation (lower left) and (d) for the NCEP/NCAR reanalysis (lower right).

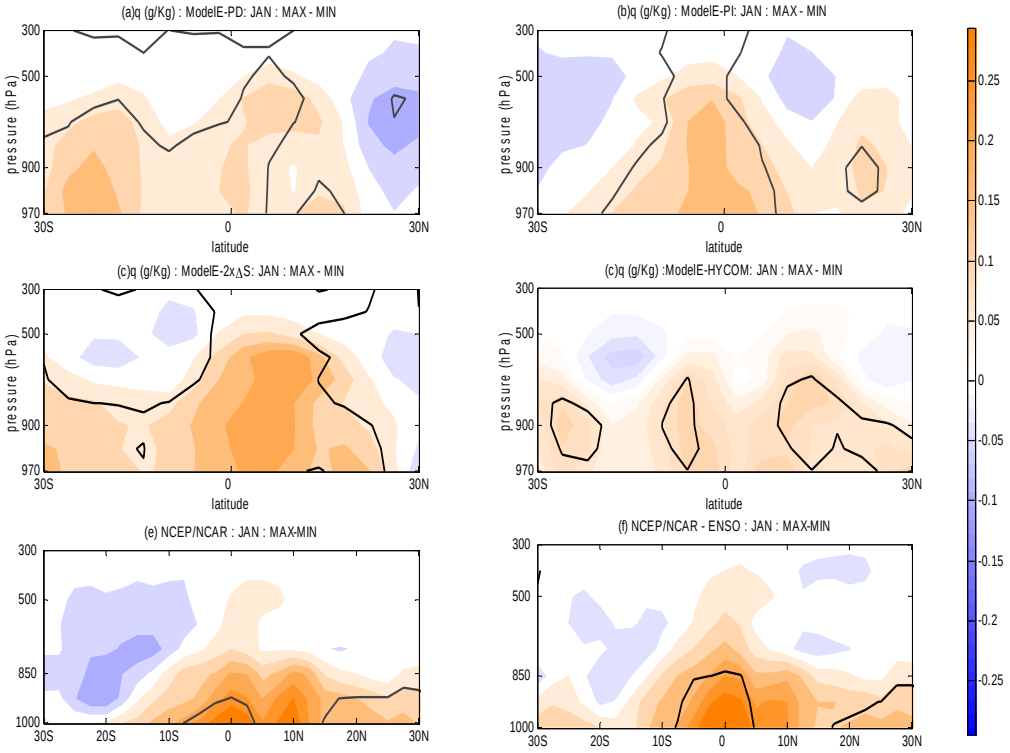

Figure 6.2 Differences of the zonally averaged specific humidity (g/Kg) between solar maximum and solar minimum in January for (a) the PD simulation, (b) the PI simulation, (c) the DF (double minimum forcing) simulation, (d) HYCOM simulation, (e) NCEP/NCAR reanalysis with all years, and (f) the NCEP/NCAR reanalysis with non-ENSO years. The solid lines represent 95% significant level computed with Student's *t-test*.

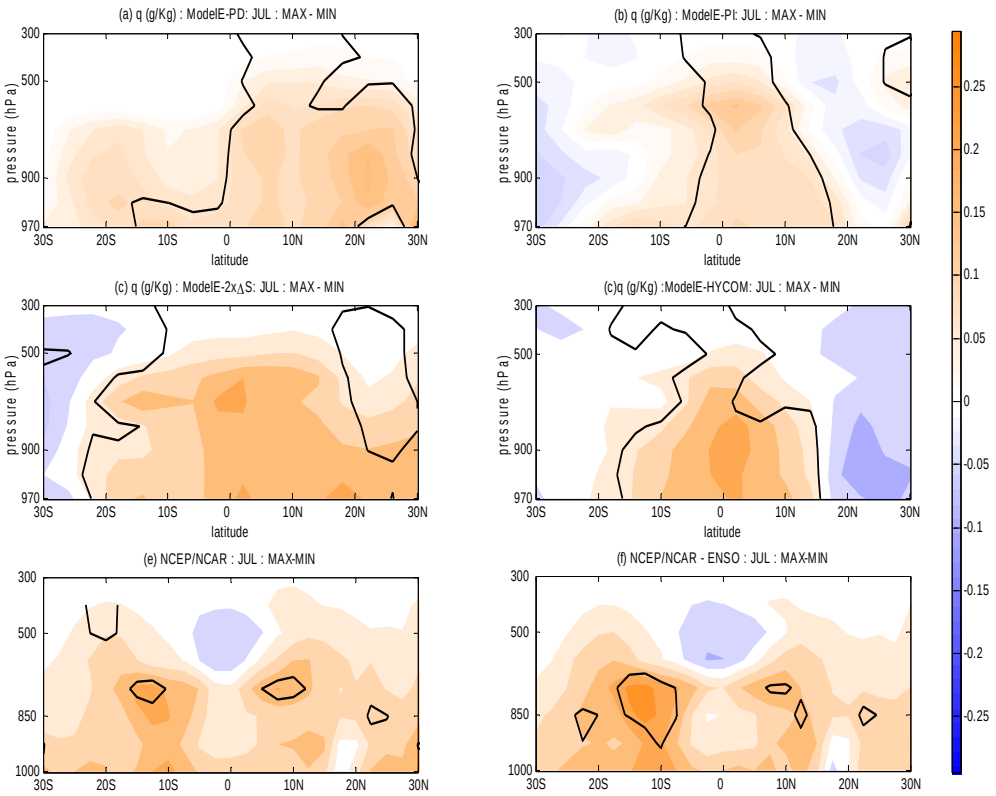

Figure 6.3 The same as in Figure 6.2, but in July for (a) the PD simulation, (b) the PI simulation, (c) the double forcing simulation, (d) HYCOM simulation, (e) NCEP/NCAR reanalysis with all years, and (f) the NCEP/NCAR reanalysis with non-ENSO years. The solid lines represent 95% significant level computed with Student's *t-test*.

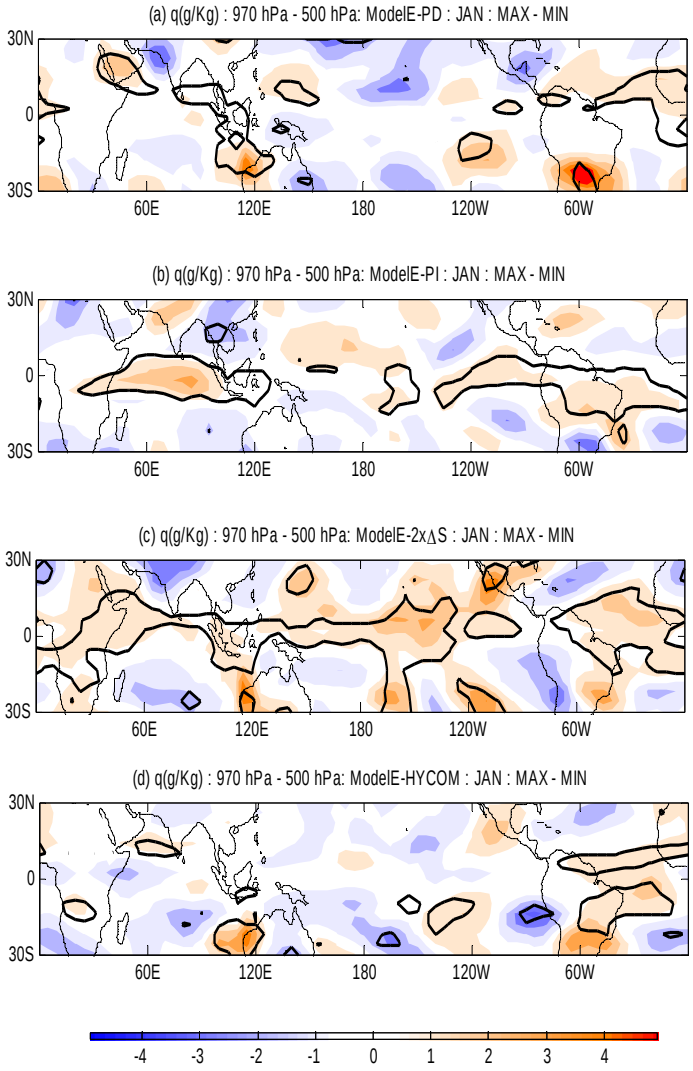

Figure 6.4 Differences of integrated specific humidity (g/Kg) from 970 hPa to 500 hPa in January for (a) the PD simulation, (b) the PI simulation, (c) the DF (double minimum forcing) simulation, (d) HYCOM simulation. The solid lines represent 95% significant level of Student's *t-test*.

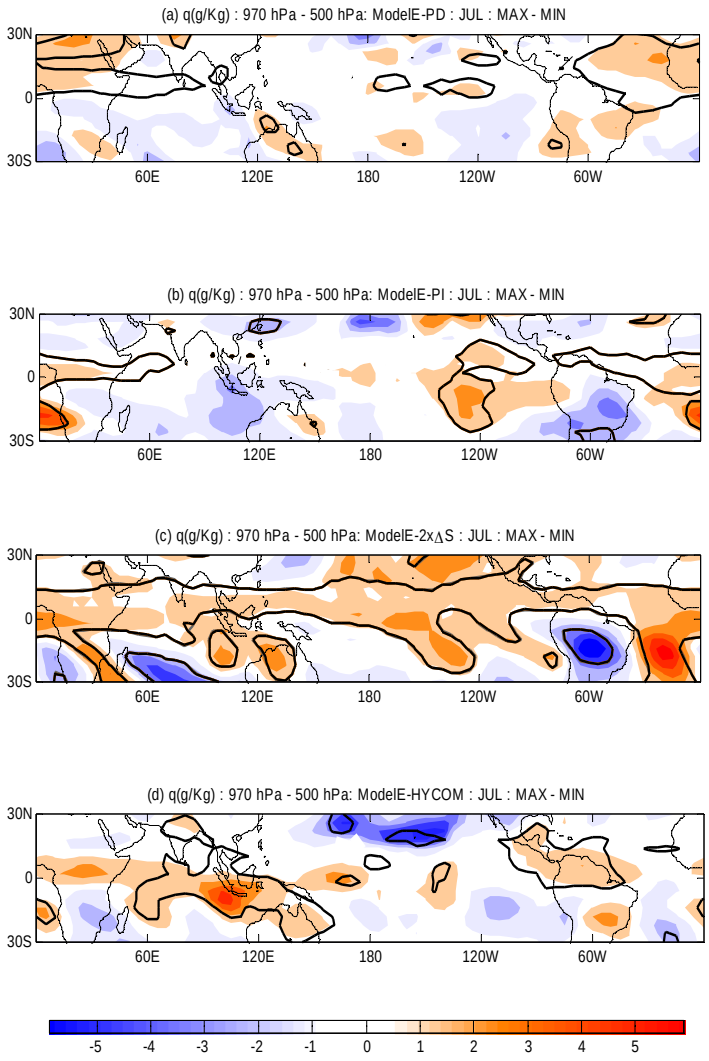

Figure 6.5 The differences of the integrated specific humidity (g/Kg) from 970 hPa to 500 hPa in July for (a) the PD simulation, (b) the PI simulation, (c) the DF (double forcing) simulation, (d) HYCOM simulation. The solid lines represent 95% significant level computed with Student's *T-test*.

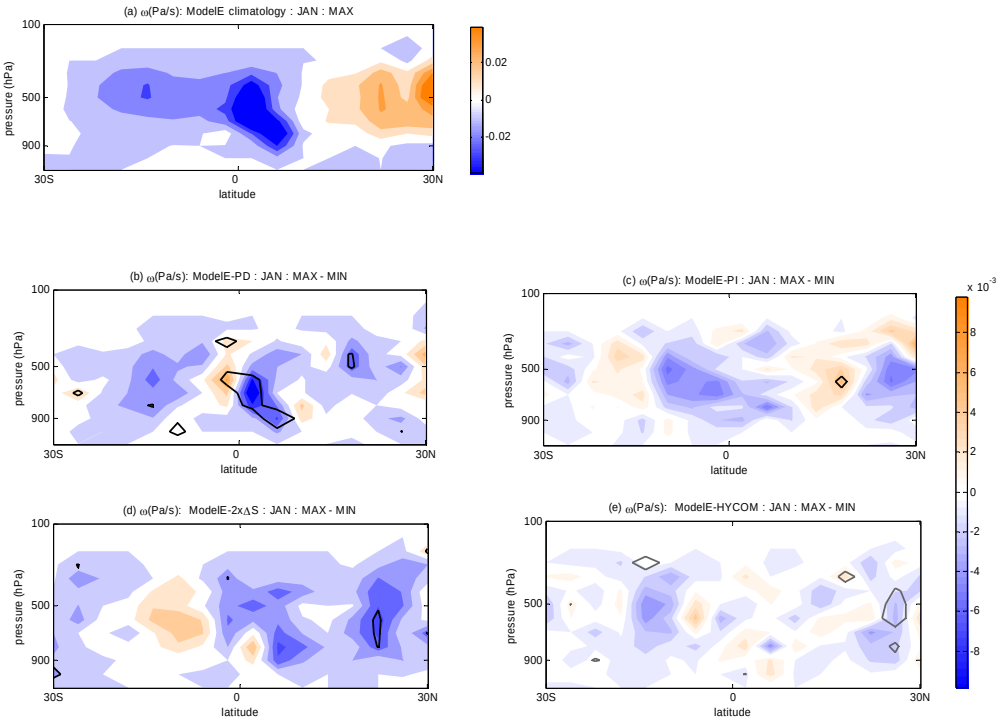

Figure 6.6 The zonally averaged vertical velocity (ω) during the month of January between 150ºE and 100ºW in Pa/s for (a) the climatology from the model simulation, and the difference between MAX and MIN for (b) the PD simulation, (c) the PI simulation, (d) the DF simulation, and (e) the HYCOM simulation. The solid lines represent 95% significant level of Student's *t-test*. Negative values represent upward motion for (a) and enhanced upward motion for (b) – (e).

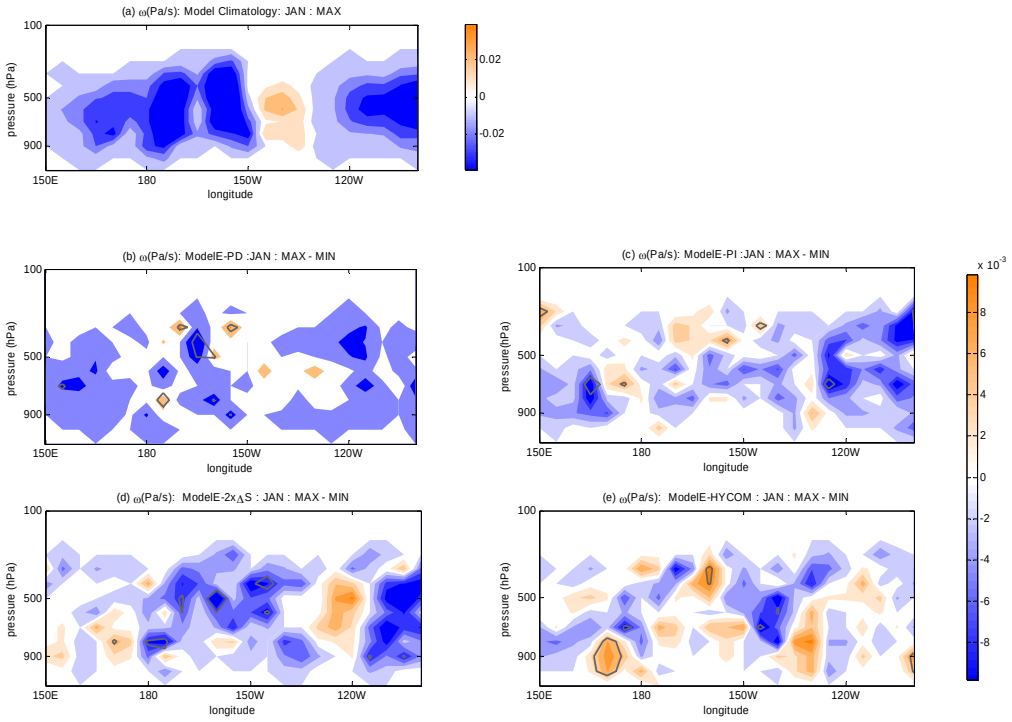

Figure 6.7 The meridionaly averaged vertical velocity (ω) during the month of January between 10ºS and 5ºN in Pa/s for (a) the climatology from the model simulation, and the difference between MAX and MIN for (b) the PD simulation, (c) the PI simulation, (d) the DF simulation, and (e) the HYCOM simulation. The solid lines represent 95% significant level of Student's *t*-test. Negative values represent upward motion for (a) and enhanced upward motion for (b) – (e).

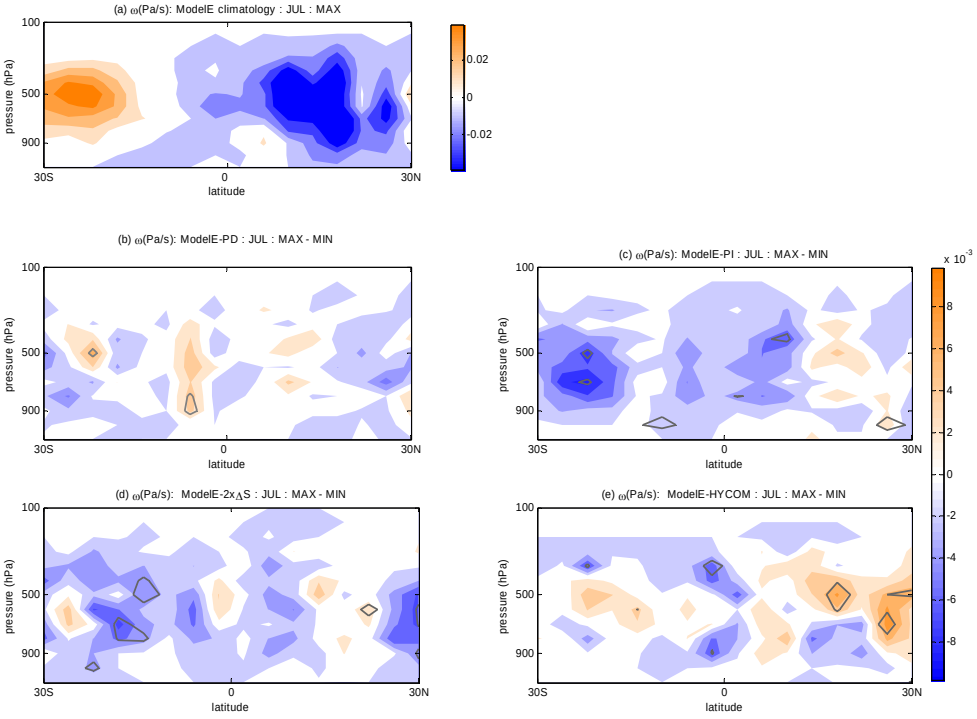

Figure 6.8 Same as Figure 6.6, but for July. Negative values represent upward motion for (a) and enhanced upward motion for (b)-(e).

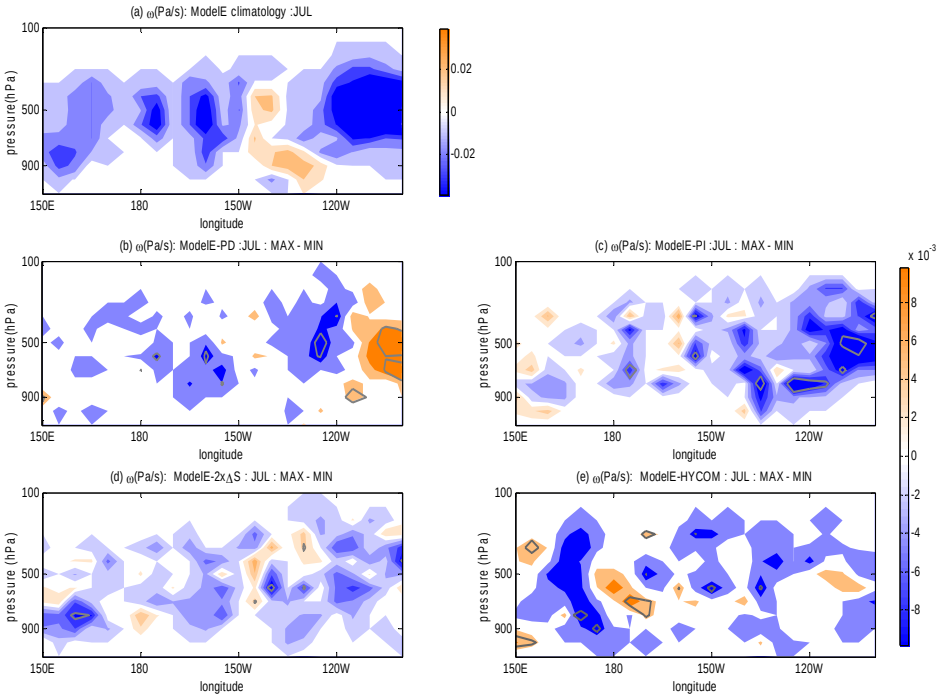

Figure 6.9 Same as Figure 6.7, but for July. The negative values represent the upward motion for (a) and the enhanced upward motion for (b)-(e).

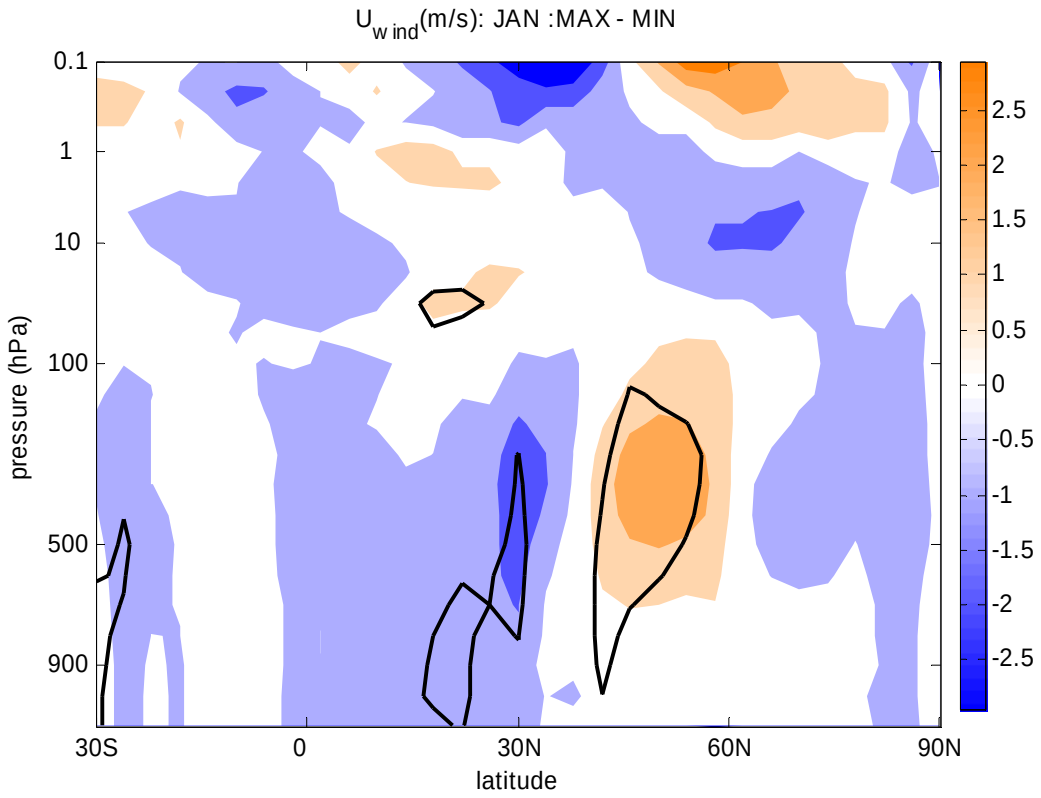

Figure 7.1 Difference in the zonal wind ($\bar{u}$) between MAX and MIN for January.

The solid lines represent 95% significant levels of Student's *t*-test.

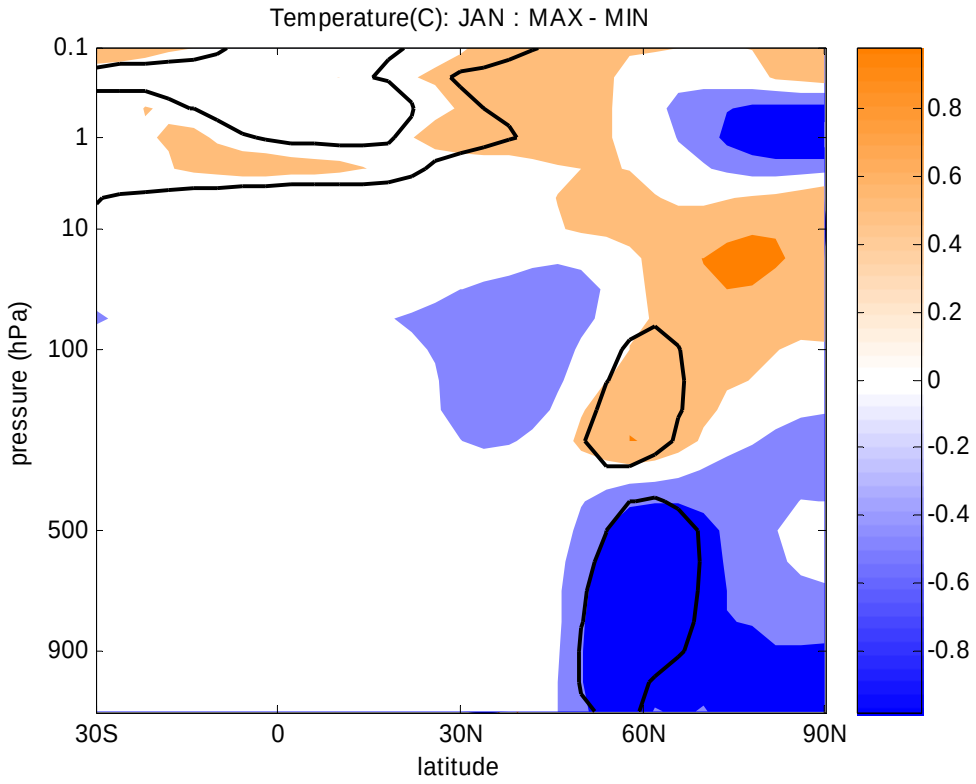

Figure 7.2 Difference in temperature (K) between MAX and MIN for January. The solid lines represent 95% significant levels of Student's *t*-test.

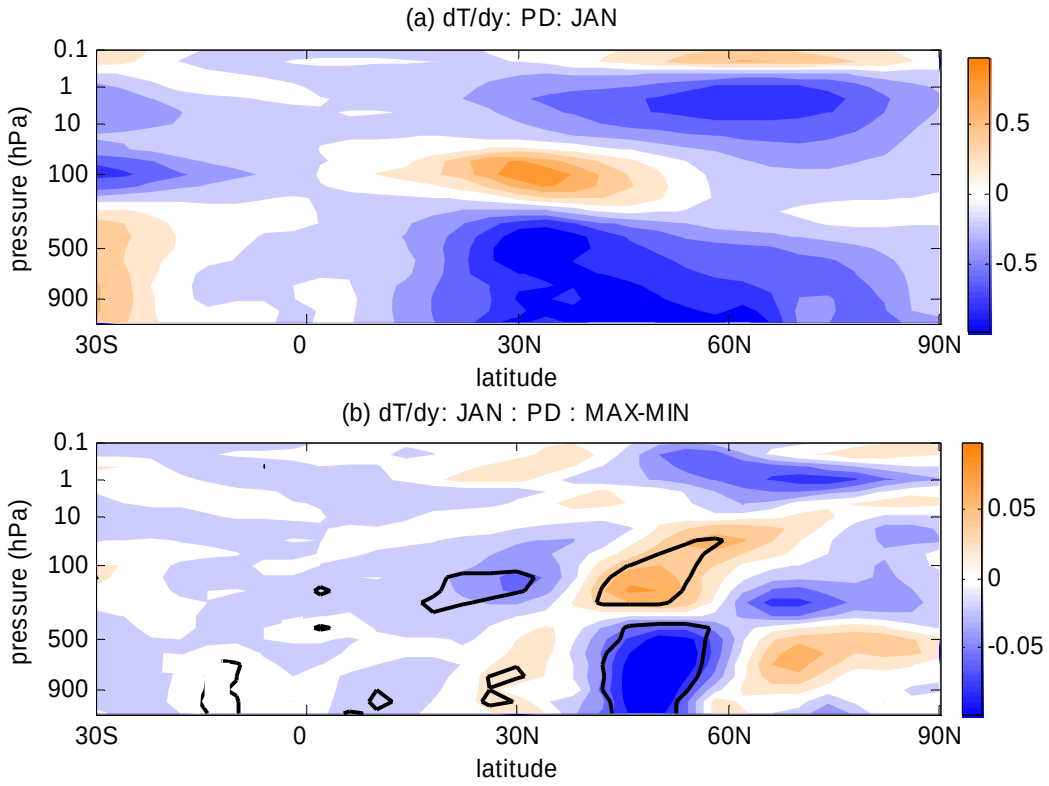

Figure 7.3 The temperature gradient (K/deg) of (a) the model and (b) difference of the temperature gradient (K/deg) between MAX and MIN. The solid lines represent 95% significant levels of Student's *t*-test.

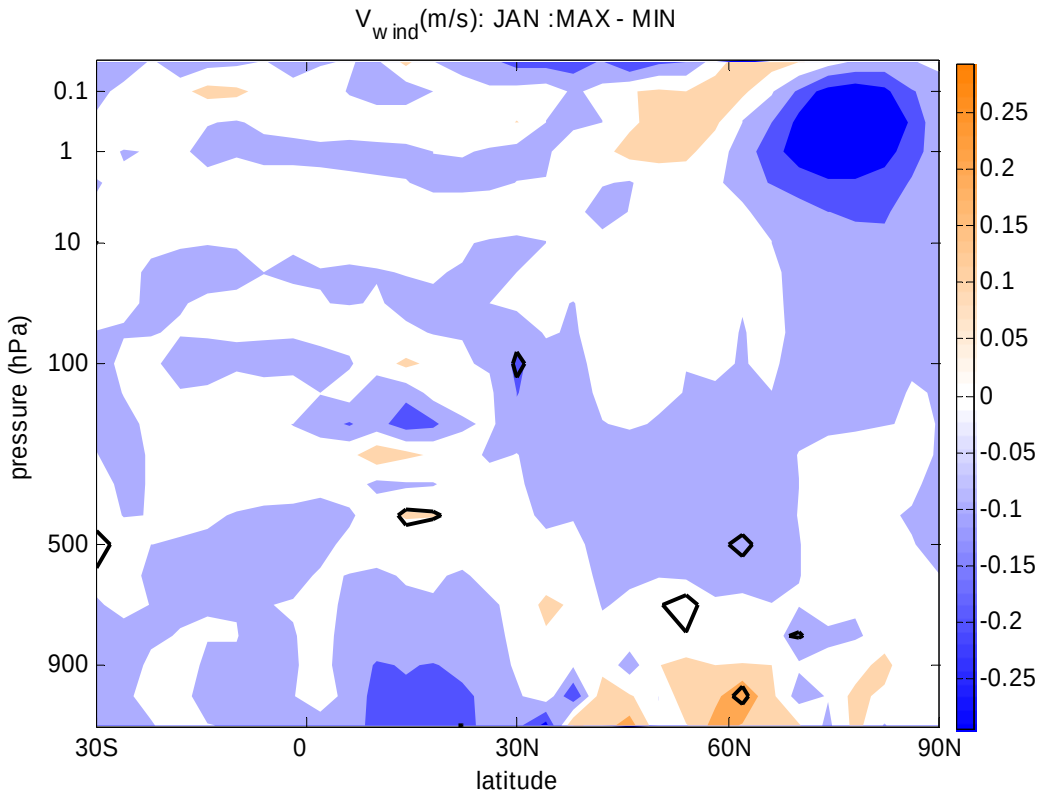

Figure 7.4 Difference in longitudinally averaged meridional velocity (υ) between solar maximum (MAX) and minimum (MIN) in January (m/s).

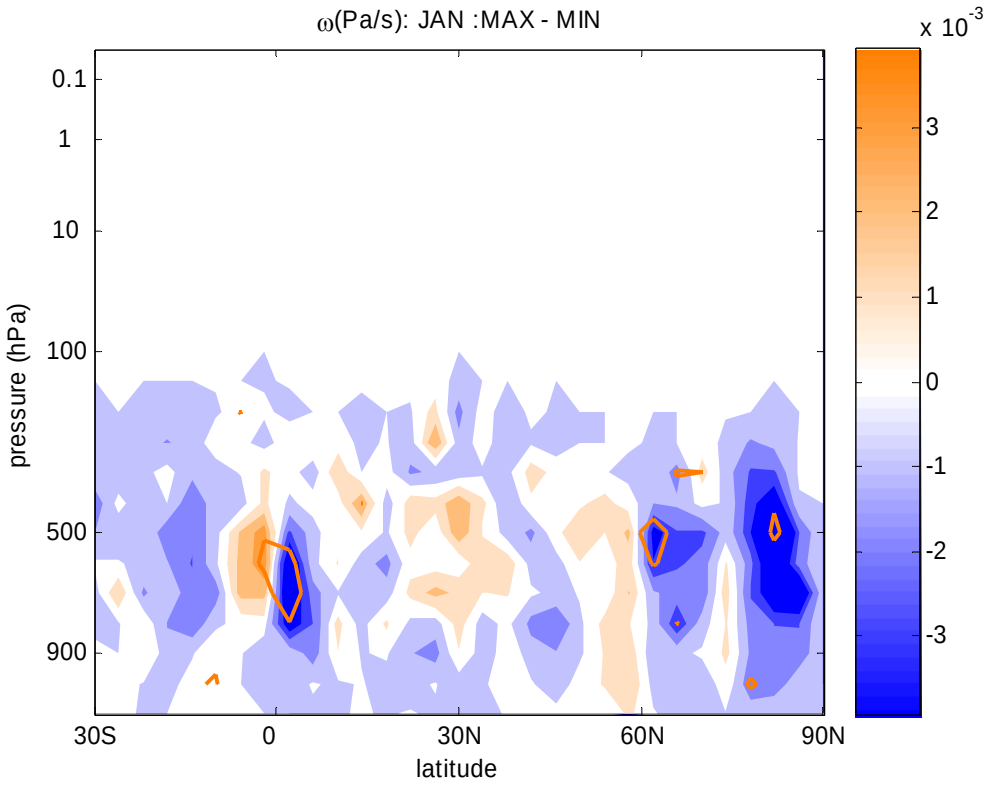

Figure 7.5 Difference in longitudinally averaged vertical velocity (ω) between solar maximum (MAX) and minimum (MIN) in January (Pa/s). The negative represents enhanced rising velocity. The solid lines represent 95% significant levels of Student's *t*-test.

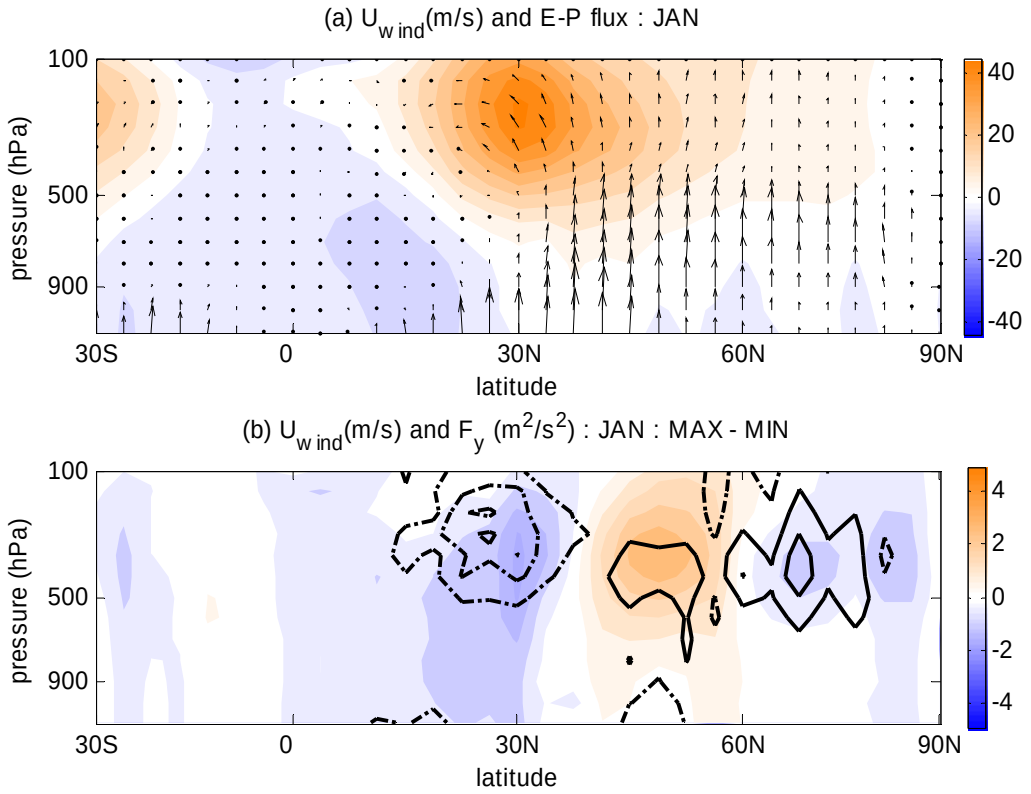

Figure 7.6 Eliassen-Palm flux (m^2/s^2) with the zonal wind (m/s) (a) for model climatology and (b) difference of poleward flux $F_y = -\rho[u'v']$ between MAX and MIN. The maximum amplitude of E-P flux is for (a) 146 m^2/s^2 and the dotted line is for negative and the solid line is positive difference with the interval of 2 m^2/s^2.

Tables

Table 1. Statistics of perturbations in the stratosphere at 10hPa that reach the surface under solar maximum and minimum conditions during 1948-2004.

	Maxima		Minima	
Signal strength	1.0σ	1.5σ	1.0σ	1.5σ
10hPa	35	22	39	26
1000hPa	16	11	5	3
Ratio	0.46	0.50	0.13	0.12
Ratio for west QBO	0.53	0.64	0.0	0.0
Ratio for East QBO	0.39	0.36	0.31	0.27

Table 2. Correlation coefficient between UV flux and summer PC1 for 1948-2004.

	Variance of PC1 for the extended summer	Correlation For the extended summer	May	June	July	August	September
10hPa	73%	-.26 (28)	-.19 (24)	-.21 (23)	-.32 (24)	-.36 **(**27**)**	-.22 (27)
30hPa	68%	-.34 (32)	-.33 (33)	-.30 (31)	**-.39** (29)	**-.41** (31)	-.29 (31)
50hPa	58%	**-.38** (35)	**-.37** (41)	**-.34** (35)	**-.44** (32)	**-.44** (33)	-.29 (30)
70hPa	47%	**-.40** (38)	**-.39** (42)	**-.36** (36)	**-.45** (34)	**-.44** (38)	-.35 (30)
150hPa	18%	**-.35** (40)	**-.34** (41)	-.30 (33)	**-.41** (33)	**-.37** (37)	-.31 (30)
300hPa	8.5%	.12 (47)	.00 (43)	.10 (38)	.27 (47)	.18 (49)	.06 (42)

Table 3. Percentage of variance explained by the winter NAM in EOF expansion of monthly mean fields for the region poleward of 20ºN: leading mode (second mode)

	ModelE_PI	ModelE_PD	NCEP
1 hPa	45% (23%)	41% (21%)	
7 hPa	33% (28%)	34% (27%)	45% (20%) at 10hPa
765 hPa	27% (12%)	25% (10%)	19% (12%) at 850hPa

Table 4. Percentage of variance explained by the summer NAM in EOF expansion of monthly mean fields for the region poleward of 20º: leading mode(second mode)

	ModelE_PI	ModelE_PD	NCEP
1 hPa	44% (19%)	45% (23%)	
7 hPa	41% (33%)	42% (32%)	73% (16%) at 10hPa
765 hPa	18% (11%)	22% (9%)	17%(11%) at 850hPa

Table 5. *Student t*-test statistics for the significance of the difference between the two means: the mean of the principal components in MAX and the mean of the principal components in MIN. Numbers in parentheses are the statistics for MAX and MIN, respectively.

	ModelE (MAX, MIN)	NCEP/NCAR (MAX, MIN)
Standard deviation, σ	0.60 (0.56, 0.64)	1.35 (1.65, 0.97)
Difference between the mean , $\mu_{MIN} - \mu_{MAX}$	0.53 (0.26, -0.26)	0.96 (-0.51, 0.44)
Degrees of freedom, $N_{MAX} + N_{MIN} - 2$	168 (85, 85)	121 (60,63)
t-value	5.76	3.94

Table 6. Description for each GISS ModelE simulation. ΔS is half of the 1.1 W/m² in solar irradiance change.

Simulations	Solar forcing	Composition	Ocean
PD-qflux	+ΔS ~ -ΔS	Present day	q-flux
PI- qflux	+ΔS ~ -ΔS	Pre-industrial	q-flux
DF-PD-qflux	+ΔS ~ -2 x ΔS	Present day	q-flux
PI-HYCOM (dynamic coupled ocean model)	+ΔS ~ -ΔS	Pre-industrial	HYCOM

Appendix I. Empirical Orthogonal Function Analysis (EOF Analysis)

1. Overview

Eigenvector analysis, commonly referred to as Empirical Orthogonal Function(EOF) analysis or Principal Component Analysis(PCA) is a statistical method to find structures that explain the maximum amount of variance from a two dimensional data set. One dimension in the data set represents the dimension in which has the structure, and the other dimension represents the dimension in which this structure is sampled. To find the characteristic spatial structures that vary with time, for example, one would use space as the first dimension and time as the sampling dimension.

Singular Value Decomposition (SVD) is a general decomposition of a matrix. EOF analysis is carried out by applying SVD on the input data matrix to find structures in both dimensions simultaneously.

2. Data matrix

2.1 The input data matrix

The row and column indices of the input data matrix define the two domains of the analysis. In general, the domains are some combination of parameter, space, and time. Space may be either one- two- or three-dimensional. The parameter refers to variables, such as geopotential height, temperature, or derived variables, etc. By

holding one parameter, over space and time, it is possible to generate the input data matrix.

Suppose we are given a $M \times N$ matrix whose elements are values of a single parameter $x_i(t_n)$ of data from *M* locations *i*

and *N* times t_n. Here the time and space domain can be regularly spaced or irregularly spaced as long as the space-time identification of the rows and columns in the input data matrix is preserved. For example, an analysis might be based upon monthly data for a number of different winter or summer seasons.

2.2 Data preparation

First, the climatological mean is extracted from the field. In this study, a symmetric orthogonal covariance matrix is used as an input data as described in section 3.2. To equally weight the variance for each grid point by the geographical area, the each grid point data is multiplied by the square root of cosine of latitude.

2.3 Structure versus sampling

In this study, the EOF patterns involve spatial patterns in the distribution of a single parameter. Sampling dimension is the time domain. In order to obtain statistically significant results, it is necessary that the effective number of degrees of freedom in the domain of the sampling be as larger than the effective number of degrees of freedom in the domain of the structure. North's criterion will be explained

in section 3.1. Since geophysical data are characterized by strong autocorrelation in the space and time domains, the effective number of degrees of freedom may be smaller than the dimension of the rows or columns in the data input matrix.

3. EOF analysis

3.1 Description

The EOF analysis yields a finite number of modes. Each mode in an EOF analysis is identified by an eigenvalue (a positive definite number which defines its rank and relative importance of modes), an eigenvector of EOF (a linear combination of the input variables in the domain of the structure), and a principal component which indicates the amplitude and polarity of that structure in the sampling domain. The principal components are the expansion coefficients of the EOF's. The eigenvalues represent how much variance is explained by each eigenvector. By arranging the eigenvalue/eigenvector pairs in order with the biggest first, then one may explain a large amount of the variance in the structure space. The goal of this method is to find a spatial pattern e_i and the time varying amplitude $Z_i(t_n)$ which explains maximum variance of the data field X.

The symmetric matrix C, which is a covariance matrix of X, can be decomposed in the following way through an eigenvector analysis.

$$Ce_i = \lambda_i e_i$$
$$CE = E\Lambda$$

Where E is the matrix with the eigenvectors e_i as its columns, and Λ is the matrix with associated eigenvalues λ_i, along its diagonal and zeros elsewhere.

Projecting a spatial pattern, $E = [e_1, e_2, ..., e_M]$, normalized so that $|e| = 1$, onto the varying data field, X, gives the time varying amplitudes, Z's.

The spatial pattern which explains the maximum variance is the first eigenvector, e_1 and is called first EOF of the input data matrix. Subsequent spatial patterns, kth EOF, e_k, can be found in order of decreasing importance, corresponding to the eigenvalue, λ_k.

EOFs can be affected by sampling biases in the covariance matrix. North et al. (1982) states that if the covariance matrix is constructed on the basis of N independent samples, its eigenvalues have sampling uncertainties $\Delta \lambda_k \sim \lambda_k \sqrt{2/N}$, and if the spacing between successive eigenvalues is comparable to or less than this sampling uncertainty, their EOFs will be heavily contaminated.

3.2 EOF analysis in matrix forms

The properties of the EOF's and PC's can be expressed in matrix forms.

$$C = \frac{1}{(N-1)} X^T X \qquad C_{jl} = \frac{1}{(N-1)} \sum_{i=1}^{N} (X_{ij} - \overline{X})(X_{il} - \overline{X}) \tag{3.1}$$

$$\mathrm{C} = \mathrm{E}\Lambda\mathrm{E}^{\mathrm{T}} = \sum_{k=1}^{M} \lambda_k e_k e_k^T \tag{3.2}$$

$$\mathrm{Z} = \mathrm{XE} \qquad Z_{ik} = \sum_{j=1}^{M} X_{ij} e_{jk} \tag{3.3}$$

$$\mathrm{X} = \mathrm{ZE}^{\mathrm{T}} \qquad \mathrm{X}_{ij} = \sum_{k=1}^{M} Z_{ik} e_{kj} \tag{3.4}$$

The subscript *i* is a row index and *k* is a column index associated with the individual EOF/PC modes. The subscript *j* is the column index in *X* and the row index in *E* and *Z*. The matrix *X* is the input data from which the column means have been removed.

Equation (3.1) defines the covariance matrix C, which is the input to the matrix singular value decomposition routine which yields the eigenvalues (λ_k) and EOF's (e_k). The diagonal elements of the covariance matrix are the variances and the trace is equal to the total variance. The covariance matrix is symmetric, i.e., $C_{jl} = C_{lj}$. The symmetric property of the covariance matrix is important to solve the eigenvalue equation. Given a matrix, it is not guaranteed that an eigenvector exists. However, if it does, it can be found by eigenvalue equation. Equation (3.2) shows how the covariance matrix can be decomposed into the eigenvectors and eigenvalues. Each mode can be seen as contributing to each element in the matrix. The matrix Λ is an eigenvalue matrix, whose diagonal elements represent the eigenvalues from largest (identified with the first or leading mode) to the smallest.

The eigenvalues have units of variance of X, and the fraction of the total variance accounted for by the k^{th} EOF is simply $\lambda_k / \sum \lambda$, where the summation is over all eigenvalues. Equation (3.3) identifies the EOF's as linear combinations of the input variables(*X*'s) that transform them into PC's (*Z*'s). Equation (3.4) shows how the input data can be represented as a sum of the contributions of the various EOF modes, each weighted by the corresponding PC, much as a continuous field can be represented as a sum of the contributions of each mode.

References

Hameed, S. and R. Wilson, Lecture notes of MAR570 (2003), MAR538(2004), Stony Brook University.

North G. R., T.L. Bell, R.F. Cahalan, and F.J. Moeng. Sampling errors in the estimation of empirical orthogonal functions. *Mon. Wea. Rev*., **110**, 699-706, 1982.

Strang, G., 1988*: Linear algebra and its Applications*, Harcourt Brace, 505pp.

Von Storch, H. and F.W. Zwiers, 1999: *Statistical analysis in climate research*. Cambridge University Press, 484pp.

http://meteora.ucsd.edu/~jnorris/sio209.sp01/EOF_tutorial.pdf

http://www.atmos.washington.edu/~dennis/